Terahertz Scanning Tunneling Microscopy of Semiconductor Nanowires

by

Max Stratmann Meouchi

A thesis submitted in partial fulfillment of the requirements for the degree of

Master of Science

Department of Physics

University of Alberta

Abstract

Terahertz-Scanning Tunneling Microscopy (THz-STM) is an exciting combination of THz experiments and STM. In conventional STM, an atomically sharp tip is used to measure the topography of a surface with sub-nanometer spatial resolution. Meanwhile, terahertz spectroscopy experiments can be used to study picosecond electron dynamics, but most experiments have a spatial resolution limited by the spot-size of the terahertz pulse. THz-STM distinguishes itself by being able to do both simultaneously - ultrafast measurements on a sub-nanometer scale. This makes it an ideal candidate to study the electron dynamics of individual nanostructures as explored in this thesis.

In this thesis, the theoretical backgrounds of STM, THz generation and detection, THz-STM, optical-pump/THz-STM-probe (OPP-THz-STM) experiments are presented, as well as the experimental setup. Photoemission experiments are then shown. These experiments use a high laser fluence to photoexcite electrons from the tip and sample and can be used to sample the THz electric field locally at the tip, and can demonstrate the ability of THz-STM to measure sub-picosecond electron dynamics. The local THz electric field at the THz-STM tip is described in detail, having been experimentally sampled at the tip and modeled using antenna coupling.

Having established the theory behind THz-STM and proven its capabilities, this thesis presents THz-STM of Cadmium Sulfide (CdS) nanowires. CdS nanowires are exciting semiconductor nanostructures with useful photocatalytic applications and a long-lived charge separation when optically excited. This thesis presents the first THz-STM study

of a semiconducting nanowire. STM of undoped CdS nanowires is shown, indicating that there is a significant amount of broadening of the image due to a convolution between the tip and sample. A bundle of undoped CdS nanowires is shown, including several ways of separating the bundle into individual nanowires, with a novel approach using a machine learning algorithm. Current-voltage characteristics are presented, showing a contrast between the undoped CdS nanowire and substrate, but not between different points on the nanowire. Differential current-voltage characteristics are also presented, which do not show a contrast between the undoped CdS nanowire and substrate. Bias-dependent scans show how the semiconducting nature of the nanowires and tip-induced band bending can lead to the STM being unable to detect the nanowires at certain biases. THz-STM results are shown on the substrate, showing an electric field dependence on the measured THz-STM signal. Algorithms showing the convolution between tip and sample are presented, along with simulations that prove the nanowire width broadening effect. Mn-doped CdS nanowires are presented in combination with simulations showing the tip-sample convolution. From these simulations, tip dimensions are fitted which match scanning electron microscopy images of the tips. For Mn-Cds nanowires, the current-voltage and differential current-voltage characteristics do not show a contrast. The first THz-STM results on Mn-CdS nanowires are presented, showing the ability of THz-STM to obtain a signal on this material. Finally, an OPP-THz-STM result on GaAs (110) is shown, as well as an attempt to obtain this result on a doped CdS nanowire at 50 K.

Preface

I declare that this thesis is an original work by myself, Max Stratmann, none of which has been published prior to the publication of this thesis. The investigation which yielded the thesis results was done starting May 2023 and ending May 2024, under the supervision of Dr. Frank Hegmann. Some results from chapter 4, chapter 5, and the contact-GaAs section in chapter 6, were taken with assistance of Howe Simpson. The nanowire samples were made by Kazi M. Alam, John Garcia and Cole Thompson under the supervision of Karthik Shankar in the Department of Electrical and Computer Engineering at the University of Alberta. Additionally, the nanowires were prepared via spincasting by John Garcia and Cole Thompson. All SEM images of the samples are used with permission of John Garcia, and all SEM images of tips are used with permission of Makoto Schreiber and Kai Cui. Some plots use a colorblind-friendly color scheme from Paul Tol.

This work has produced a first-author presentation titled "Scanning Tunneling Spectroscopy of Cadmium Sulfide Nanowires", given by myself, which was presented at the 14th Annual Symposium for Graduate Physics Research hosted by the Graduate Physics Students Association and earned 2nd place overall. The work in this thesis has produced a secondary authorship in a poster presentation, given by Cole Thompson at the Winter 2024 Dean's Research Award Poster Presentation & Competition, titled "Characterization of Semiconductor Nanowires using Scanning Tunneling Microscopy". Additionally, other work has produced authorships in two poster presentations given by Howe Simpson, given at the 13th and 14th Annual Symposium for Graduate Physics Research hosted by the Graduate Physics Students Association, titled "Short Pulses and Sharp Tips: An Introduction to Terahertz Scanning Tunneling Microscopy" and "Crashing a Tip (on Purpose) in a Terahertz Scanning Tunneling Microscope", respectively.

Acknowledgements

Thank you to my supervisor, Frank Hegmann, for your guidance and for letting me do an MSc in your lab. It has been a pleasure working in your group. Despite everything I've done, I hope my biggest achievement during my tenure here is being the best karaoke singer in the lab.

Thank you to Howe Simpson for teaching me THz-STM, and organizing physics softball. Thank you Cole Thompson for helping with the initial nanowire scanning and wearing a suit to the lab with me. Thank you Charles Jensen for giving me thesis advice and helping me with the liquid helium, among other things. I'm sure the Bogdan transform will become famous one day. Thank you to Nils Refvik for helping teach me THz-STM, and always sending out useful papers. Thank you to Makoto Schreiber for taking SEM images of my tips, and for inviting me to climbing and squash. Thank you to Sam Ruttiman for always having interesting conversations and being a fellow climbing advocate. Thank you to Niloufar Sadeghi for always being friendly - and always bringing yellow rice for lunch. Thank you to Hasti Hojabrosadati for being a great office mate and always joining squash and climbing. Thank you to Aran McDowell for sending me useful reading materials. Thank you to Nabiha Saghar for being friendly summer student. Thank you to Marín Calzada for helping with miscellaneous things, such as sending me the 3D printed scanhead models. Thank you to Peter Nguyen for explaning what tips are best for THz-STM. Thank you to the temporary german students who came over for the ATUMS collaboration: Matthias, Lennart, other Matthias, and Phillip. You all brought your cheerful attitudes from home and it was nice speaking German on occasion. Thank you to the temporary british student, Jacob. Thank you to Greg Popowich and Manvir Gil for their technical expertise and good conversations.

Thank you all the friends I made along the way: Abhi, Sam, Kusum, Camilo, Federica, Luana, Leo, Harrisen, and all my other friends in Edmonton. Thank you to all my family and friends back home, all of whom I miss very dearly. Thank you to my partner Christina Strilets for always being there for me. Finally, thank you to my parents, Miguel Stratmann and Josefina Meouchi, for their support, even though I am far away from them.

Table of Contents

List of Tables

List of Figures

Chapter 1

Introduction

As science begins to explain more and more of the natural world, we begin to run out of easily perceptible phenomena. This has led scientists to explore objects that have a radically different physical and temporal scale than what we can normally perceive. In the field of condensed matter physics, this corresponds to phenomena that are very small and occur very quickly. As will be explained later, these two characteristics will be combined in a technique known as terahertz scanning tunneling microscopy [1].

In order to see phenomena smaller than our eyes are physically capable of, we require specialized tools and instruments. The first microscopes ever documented, made by Robert Hooke and Antonj van Leeuwenhoek in the early 1600s [2], led to the discovery of cells and spawned an entire field of science known as microbiology. However, optical microscopes are limited by the diffraction limit, as discovered in 1835 by George Airy. The first microscope to bypass this limit is scanning near-field optical microscopy (SNOM), first invented by Edward Hutchinson Synge in 1928. This technique was able to resolve individual organic molecules. The first electron microscope was developed in 1931 by Max Knoll and Ernst Ruska [3]. The microscope that we will focus on is the Scanning Tunneling Microscope (STM), first developed in 1981 by Gerd Binnig and Heinrich Rohrer [4]. Five years later, they received a Nobel prize in physics due to their work.

STM has the capability to image individual atoms on the surface of a material with sub-Å precision [4]. This is orders of magnitude less than an optical microscope, which would have a diffraction limit of 200 nm for blue light. The resolution of an STM depends on its vibrational isolation, piezoelectric motor calibration, the profile of the sharp metal tip used, electronic noise, vibrational noise, and other types of noise.

In addition to being able to resolve atoms, molecules, surface reconstructions [5], and nanoscale materials [6], STM can also be used to measure the local density of states [7] and

work function of materials.

On the other hand, being able to resolve phenomena faster than our eyes can detect is a more recent accomplishment. A well known story is that of Eadweard Muybridge who in 1878 first photographed a horse galloping, proving that it had all four legs in the air at some moments [8]. Although camera technology has since progressed to have a large amount of frames per second, this technology is diffraction limited and cannot photograph nanoscale phenomena.

Terahertz (10^{12} Hz) radiation is loosely defined as any form of electromagnetic wave with a frequency between 0.1 to 30 THz. Historically, this frequency band was often referred to as the "terahertz gap" due to the difficulty in generating and detecting radiation of this particular wavelength [9]. Additionally, THz experiments are experimentally challenging due to terahertz not being visible with the naked eye or common infrared viewers.

The discovery of millimeter-wave generation and detection with picosecond photoconductors [10], by Auston and Smith, is widely regarded as the beginning of THz science (although the wavelength observed was 0.055 THz). Since then, more THz generation and detection methods have arisen, such as stimulated emission under electric and magnetic fields [11] [12], and quantum-cascade lasers [9, 13–15]. There also exist optically-based methods for terahertz generation, such as tilted pulse front [16] and spintronic sources.

THz radiation has several interesting properties that we can use. A wave with a frequency of 1 THz has a corresponding wavelength of 300 μm, a 1 ps period and a photon energy of 4.1 meV. The timescale probed by THz beams is applicable to plasmon scattering, phonon resonances, magnons [17], carrier transport in nanomaterials such as nanodots [1], carbon nanotubes [18], and nanowires [19].

Thanks to the Nobel-prize-winning technology of chirped pulse amplification (CPA), discovered by Donna Strickland and Gérard Mourou in 1985 [20], we are able to easily create powerful ultrafast pulses. As will be discussed later, we can convert these optical-frequency pulses into terahertz-frequency (10^{12}) pulses. By cleverly utilizing these pulses, which have a timescale of femtoseconds (10^{-15} s) or picoseconds (10^{-12} s), we can discover new physics on those same timescales.

The first instance of terahertz time domain spectrosopy (TDS) was published in 1988 by Smith et al [17]. There also exists terahertz emission spectroscopy and time-resolved terahertz spectroscopy (TRTS), which can be used to obtain information about the Drude-smith model of conductivity and semiconductor lifetimes, among other things [21, 22]. However, these methods are all diffraction limited.

There exist multiple ways to obtain smaller spatial resolution using terahertz waves. A regular THz pulse, such as the ones used in TRTS, are diffraction limited to 0.15 mm

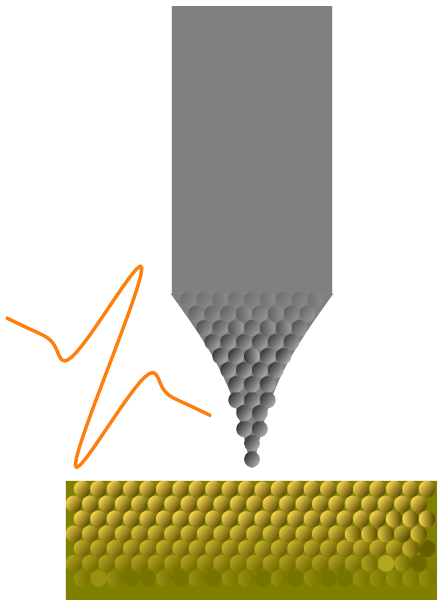

Figure 1.1: A simple model of a THz-STM. A THz beam couples to a sharp metal tip, that is one atom thick at the end, which focuses the THz into the tip-sample junction, allowing it to resolve details on the atomic scale.

for a 1 THz centered pulse. It is possible to use an aperture to limit the resolution to the micrometer scale [23]. One can also use terahertz scattering SNOM to obtain a resolution on the scale of tens of nanometers [24]. We can also couple terahertz atomic force microscopy to obtain a resolution on the angstrom scale [17, 23].

Finally, we can combine combine terahertz pulses with STM in a technique known as THz-STM. This technique involves directing a THz to an STM junction, where the sharp metal tip will act as an antenna and focus the THz into the tip-sample junction, as seen in Fig 1.1. Due to a field enhancement that increases the local (or near-field) THz at the junction, and the nonlinear properties of the junction, the THz rectifies electrons only at the junction. This gives it the spatial resolution of STM and the time resolution of THz. THz-STM can obtain resolutions on the scale of hundreds of picometers and femtosecond timescales [1, 5, 23, 25]. This powerful technique allows us to obtain nanodot carrier dynamics [1], scan surfaces without a DC bias and detect imperfections [5] [18], obtain graphene nanoribbon local density of states [26], tracking molecules [24], and more. However, this technique is not without challenges: coupling THz successfully depends on the tip geometry and parameters used, which can be hard to achieve.

Cadmium Sulfide (CdS) is a semiconductor with a bandgap of 2.4 eV that has promising applications as a photocatalyst. CdS is an interesting material in its own right, with

good visible light absorption, and electron-hole pair generation with long decay times [27, 28].

A nanowire is simply a wire where the two smaller dimensions are on the nanometer scale, which will give it different properties than the bulk form of the constituent material. Nanowires have a much higher surface-to-volume ratio and quantum confinement effects due to being a one-dimensional material. CdS-Pt nanorod heterostructures have also shown a fast separation of electron-hole pairs and a long-lived charge separation [28], making them an excellent candidate for photocatalysis. Work on regular CdS nanowires in time-resolved terahertz spectroscopy (TRTS) [19, 22] corroborates these results.

In this thesis, the primary objective will be to study these CdS nanowires in order to obtain the first THz-STM results on a nanowire. The results in this thesis will build towards the ability to find nanowires, scan them, and ultimately be able to resolve their ultrafast charge-carrier separation using an optical pump - terahertz-STM probe experiment.

The contents of this thesis are as follows: Chapter 2 will focus on Scanning Tunneling Microscopy, its theory and types of data collection. Chapter 3 will focus on THz, THz-STM and the experimental setups used. Chapter 4 will describe OPP-THz-STM theory and give experimental photoemission results. Chapter 5 focuses on CdS nanowire sample preparation, scans in Ambient STM, Ultra-high-vacuum STM and THz-STM. Chapter 6, the longest chapter, will discuss doped CdS nanowires, experimental considerations that depend on the STM tip used, advanced analysis of STM images, THz-STM results on nanowires, and OPP-THz-STM results on CdS nanowires and GaAs. Finally, Chapter 7 will conclude all of the results found.

Chapter 2

Scanning Tunneling Microscopy

2.1 Theory of STM

In the model of STM, we define the system as an atomically sharp tip and a sample separated by some distance z, as shown in Fig. 2.1. There exists a potential difference V_0 between the tip and sample. We can model this as a one dimensional system, where the tip and sample are both metallic and separated by a distance z, with vacuum in between. Classically, there is no conduction medium so there should be no current. However, if we model this as a quantum problem, there can actually exist a flow of current between tip and sample due to quantum tunneling. We will model the vacuum as having a position-dependent potential $V(x)$, which consists of three regions. Region A is the tip, with a potential of $V = 0$, region B is the vacuum, with a potential $V = V_0$, and region C is the sample with potential $V = 0$. Therefore, this can be modeled as

$$V(z) = \begin{cases} 0 & x > z \text{ (Region A)} \\ V_0 & 0 \leq x \leq z \text{ (Region B)} \\ 0 & x < 0 \text{ (Region C)} \end{cases}. \tag{2.1}$$

Starting with an electron of mass m, wavefunction Ψ, and from the time-independent Schrödinger equation (TISE):

$$\frac{\hbar^2}{m}\frac{\partial^2\Psi(x)}{\partial z^2} = [V(x) - E]\Psi(x). \tag{2.2}$$

Using the wave approximation where our wavefunctions are predefined to be of the form $\Psi_{\text{wave}} \propto e^{ikx}$, we obtain two different solutions. In regions where the electron energy is greater than the potential, those being regions A and C, we obtain:

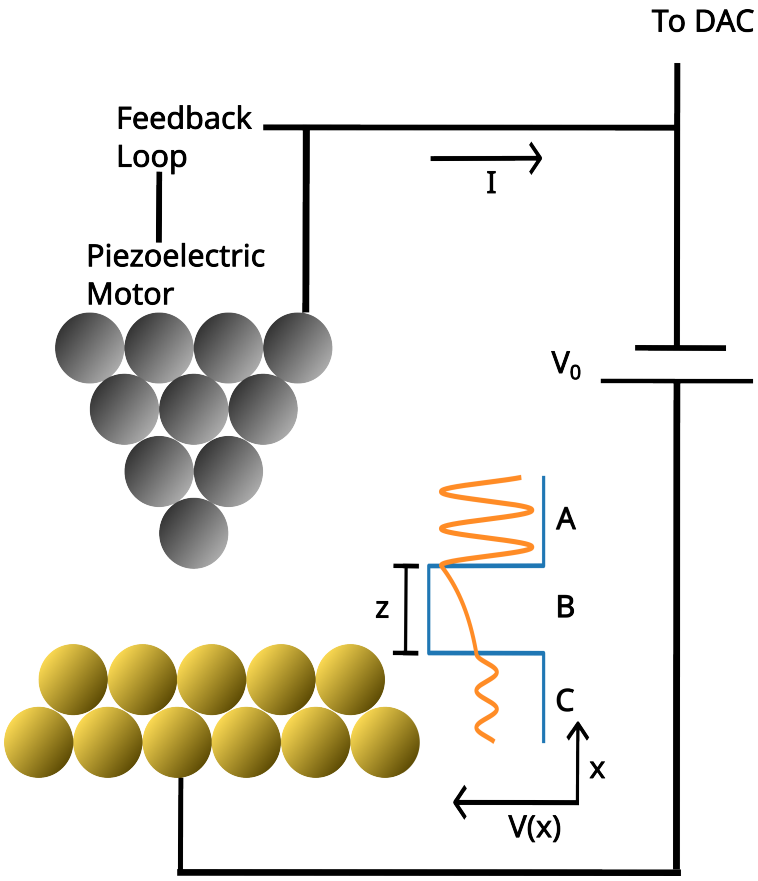

Figure 2.1: A schematic of a scanning tunneling microscope. A sharp metal tip, that is one atom thick at its very bottom, is within tunneling range of a surface. The sample is biased with a voltage V_0, and there is a current I flowing between the tip and sample. There exists a potential barrier between the tip and sample through which the electrons can tunnel. In the subfigure, the barrier potential is represented in blue and the tunneling of an electron wave is shown in orange. In this case, electrons are tunneling from the tip to the sample. Additionally, the current read is measured by a feedback loop which controls the z-position of the tip via a piezoelectric motor.

$$\Psi_{\mathrm{A,C}} = A_{\mathrm{A,C}} e^{ikx}, \tag{2.3}$$

with corresponding wavevector k:

$$k = \sqrt{\frac{2m}{\hbar^2}(E - V(x))}. \tag{2.4}$$

In the region where the potential is greater than the electron energy, we get an exponential decay of the form:

$$\Psi_{\mathrm{B}} = A_{\mathrm{B}} e^{-\kappa x}, \tag{2.5}$$

with corresponding wavevector κ:

$$\kappa = \sqrt{\frac{2m}{\hbar^2}(V(x) - E)}. \tag{2.6}$$

An algebraic solution may be obtained by matching the amplitudes of the wavefunctions and their derivatives at the boundaries, however one may intuitively determine that the electron behavior in region B will exponentially suppress the wavefunction magnitude by a factor κz at the end of the region where $x = z$. As we increase the separation z, we return to the classical limit where there is no wavefunction in region C and therefore no tunneling. This property shows how the STM is able to achieve such a high vertical resolution. To first order, only the bottom-most atom will contribute to tunneling (and therefore the signal), meaning that all our information has a spatial resolution approximately the size of one atom.

We can use the Wentzel–Kramers–Brillouin approximation, often abridged as the WKB approximation, to obtain an easier solution. With this approximation, the transmission probability between the edges of region B is as follows:

$$T(E) = \left|\frac{\Psi(z)}{\Psi(0)}\right|^2 = e^{(-2\sqrt{\frac{2m}{\hbar^2}}\int_0^z \sqrt{V(x)-E}\,dx)}, \tag{2.7}$$

and, since there is a constant potential $V = V_0$ in this region, this leads to:

$$T(E) = \left|\frac{\Psi(z)}{\Psi(0)}\right|^2 = e^{(-2\sqrt{\frac{2m}{\hbar^2}}(\sqrt{V_0-E})z)}. \tag{2.8}$$

It is important to note that the WKB approximation also shows the exponential relationship between tunneling and tip-sample separation z, similarly to what was done prior.

2.2 Bardeen Tunneling Model

The Bardeen Tunneling Model [29, 30], instead of a three-region zone, assumes two pairs of regions (sample and vacuum, vacuum and tip). To simplify the notation, $V = V_{\text{sample}} - V_{\text{tip}}$ will refer only to the potential difference between the tip and the sample, where the sample is the one being biased. The electron tunneling is thereby calculated using time-dependent perturbation theory and using Fermi's golden rule, Eqn 2.9, to calculate the transition rate of states w as:

$$w_{\text{i,t}\,\to\,\text{f,s}} = \frac{2\pi}{\hbar}|M_{\text{fi}}|^2\delta(E_{\text{f}} - E_{\text{i}}), \tag{2.9}$$

where i is the initial tip state, f is the final sample state, and M is the matrix element:

$$M_{\text{fi}} = \frac{\hbar^2}{2m}\int_S [\psi_{\text{i}}(\mathbf{r})\nabla\psi_{\text{f}}^*(\mathbf{r}) - \psi_{\text{f}}(\mathbf{r})^*\nabla\psi_{\text{i}}(\mathbf{r})]d\dot{\mathbf{S}}, \tag{2.10}$$

where S is a tip-sample separation surface. Furthermore, we can sum over all states, multiply by charge, and then double that to include electron degeneracy, to get the (absolute) current traveling through the STM.

$$I = \frac{4\pi e}{\hbar}\sum_{i,f}|M_{\text{f,i}}|^2\delta(E_{\text{f}} - E_{\text{i}}). \tag{2.11}$$

However, it is more useful to work in an energy formalism as opposed to one with wavefunctions. Electron properties dictate that each wavefunction will have a unique energy leading to:

$$M_{\text{fi}}(\psi_{\text{i}}, \psi_{\text{f}}) \to M(E_{\text{f}}, E_{\text{i}}) = M(E_{\text{f}}), \tag{2.12}$$

and using the dirac delta function properties we can derive that:

$$|M(E_{\text{f}})|^2\delta(E_{\text{f}} - E_{\text{i}}) = \int_{-\infty}^{\infty} M(\epsilon)\delta(E_{\text{i}} - \epsilon)\delta(E_{\text{f}} - \epsilon)d\epsilon, \tag{2.13}$$

which can be inserted into Eqn 2.9 to get:

$$w_{\text{i}\,\to\,\text{f}} = \frac{2\pi}{\hbar}\int_{-\infty}^{\infty}|M(\epsilon)|^2\delta(E_{\text{i}} - \epsilon)\delta(\epsilon - E_{\text{i}})d\epsilon, \tag{2.14}$$

which is the transition rate in an energy formalism. Next, keeping in mind the DOS equation, which is:

$$\rho(E) = \sum_k \delta(E - E_{\text{k}}), \tag{2.15}$$

we can derive the current once more in an energy formalism. Using the same process from Eqn. 2.11, but this time using the results from Eqn. 2.14, the current is:

$$\begin{aligned} I &= \frac{4\pi e}{\hbar} \sum_{i,f} \int_{E_{\mathrm{f,t}}}^{E_{\mathrm{f,s}}} |M(\epsilon)|^2 \delta(E_{\mathrm{i}} - \epsilon)\delta(\epsilon - E_{\mathrm{i}}) d\epsilon \\ I &= \frac{4\pi e}{\hbar} \int_{E_{\mathrm{f,t}}}^{E_{\mathrm{f,s}}} |M(\epsilon)|^2 \sum_i \delta(E_{\mathrm{i}} - \epsilon) \sum_f \delta(\epsilon - E_{\mathrm{i}}) d\epsilon \\ I &= \frac{4\pi e}{\hbar} \int_{E_{\mathrm{f,t}}}^{E_{\mathrm{f,s}}} |M(\epsilon)|^2 \ \rho_{\mathrm{t}}(\epsilon)\rho_{\mathrm{s}}(\epsilon) d\epsilon \end{aligned} \tag{2.16}$$

Finally, we can see that the current depends on the local densities of state of the tip and sample, as well as a tunneling probability that depends on the wavefunctions of the tip and sample. To further simplify this and get it into nicer form, we use the relationship $E_{\mathrm{f,tip}} - E_{\mathrm{f,sample}} = eV_0$, where V_0 is the applied bias (in equilibrium these fermi energies are equal). Additionally, since we are biasing the tip, we set $\rho_{\mathrm{t}}(\epsilon) \to \rho_{\mathrm{t}}(\epsilon - eV_0)$ so that its energy level is relative to its own fermi level. This yields:

$$I = \frac{4\pi e}{\hbar} \int_0^{eV_0} T(\epsilon, V, z)\rho_{\mathrm{t}}(\epsilon - eV)\rho_{\mathrm{s}}(\epsilon) d\epsilon, \tag{2.17}$$

where the transmission factor is $T(\epsilon, V, z) = |M(\epsilon)|^2$. Using the assumptions of the Bardeen model that the wavefunctions are just exponentially decaying within the vacuum, and assuming elastic tunneling ($E_{\mathrm{f}} = E_{\mathrm{i}} = E$), we use trial wavefunctions to construct

$$\begin{aligned} \psi_{\mathrm{t}}(x) &= \psi_{\mathrm{t}}(0)e^{-\kappa x} \\ \psi_{\mathrm{s}}(x) &= \psi_{\mathrm{s}}(z)e^{-\kappa(z-x)} \\ M(\epsilon) &= \frac{\hbar^2}{2m} \int_S 2\kappa\psi_{\mathrm{t}}(0)\psi_{\mathrm{s}}(z)e^{-\kappa z} dS \\ M(\epsilon) &= \frac{\hbar^2}{m} \kappa\psi_{\mathrm{t}}(0)\psi_{\mathrm{s}}(z)e^{-\kappa z} A. \end{aligned} \tag{2.18}$$

From this it is easy to see that the transmission factor depends on junction area, electron energy, voltage, and tip-sample separation:

$$T(E, V, z) \propto Ae^{-2\kappa z} = Ae^{-2z\sqrt{\frac{2m}{\hbar}[E-V]}}. \tag{2.19}$$

Which once again shows that the transmission is exponentially proportional to distance, as shown before. Putting together the entire picture, we can make more inferences. Based on

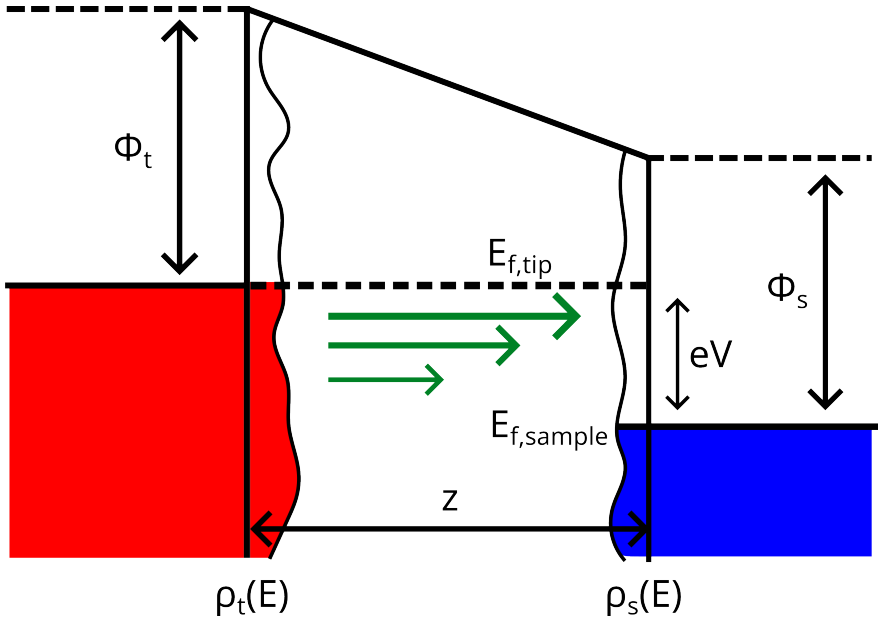

Figure 2.2: The energy bands of the tip and sample according to the Bardeen Model. The fermi levels are separated by eV due to the bias on the tip. The barrier heights (to vacuum) are given by ϕ_t and ϕ_s, respectively. Electrons are tunneling from the tip to the sample (separated by a distance z), as shown by the green arrows. The LDOS of the tip and sample vary across the energy landscape and are given an arbitrary profile for demonstrative purposes. Figure adapted from Ref. [29].

Eqn. 2.19 we can see that the tunneling probability depends on the applied voltage. Also, from Eqn. 2.17 we see that the tunneling probability depends on the tip and sample density of states. If a semiconducting sample is chosen, there will be no tunneling from states within the bandgap, as shown by Feenstra [7].

The full diagram of the energy bands can be found in Fig 2.2. This figure neglects band-bending effects [30], which are important but not discussed in this thesis.

Similarly to the energy formalism, the equations governing an STM are often defined in the context of barrier heights. Defining the barrier heights of the tip and sample as ϕ_t and ϕ_s, respectively, respectively, the barrier height at the middle (approximately the average) is $\overline{\phi} = (\phi_t + \phi_s)/2$. An electron in the middle of the gap will see a "raised" barrier by $eV/2$ but will also see a decrease due to its energy ϵ relative to $E_{f,sample}$ (where ϵ can range from 0 to eV). Therefore it will see a barrier height of $\phi_{eff} = \overline{\phi} + eV/2 - \epsilon$. Recall that in our original formalism we defined a rectangular potential. We can use ϕ_{eff} the barrier height of the rectangular potential. Therefore, Eqn. 2.19 becomes:

$$T(E, V, z) \propto e^{-2\kappa z} = e^{-2z\sqrt{\frac{2m}{\hbar}\phi_{eff}}}. \tag{2.20}$$

2.3 Imaging with STM

2.3.1 Experimental Considerations

The principle of scanning tunneling microscopy is as follows: the tip of the STM is lowered until an appreciable current is measured (usually 1 nA - 10 pA). The current height of the tip is taken to be the approximate height of the surface at that particular point. Then, the tip is moved sideways to perform a raster scan of the surface. At every point along the scan, the height of the tip is measured, leading to an image such as Fig. 2.3.

The tip is moved using piezoelectric motors. Piezoelectric materials are materials whose crystal lattice spacing is increased or decreased by an applied electric field. This makes a motor expand or contract, moving the tip attached to it. For STM, a good motor can move precisely with sub-angstrom amounts using easily achievable levels of voltage. However, there are several considerations. Piezoelectric response is nonlinear, so a "linear" region of the response must be chosen and operated on. Also, piezoelectric drift and hysteresis are factors to consider as well. In order to properly calibrate the relationship between applied bias on the piezoelectric motor and movement of the tip, a well-known sample can be used. Highly oriented pyrolitic graphite (HOPG) is one such material. Figure 2.3 shows the electronic structure of HOPG in air. In this example of STM, the tip is made out of platinum iridium, and cut by hand by shearing a piece of platinum iridium wire. By measuring the atomic spacing between atoms (2.46 $\mathring{A}$), and by measuring the step edge between monolayers of graphene (some multiple of 3 $\mathring{A}$), the STM can be calibrated.

Determining the absolute value of z can be done by lowering the tip until it enters a 'contact' regime where lowering the tip further will not result in more current. Additionally, the current increases by a large amount since it is no longer in the tunneling regime. Whenever STM data is taken, the tip height is determined by the bias and setpoint before the feedback loop was disengaged. Having a different tip-sample separation may produce slightly different STM images. Additionally, the bias used is very important. This can also determine tip-sample separation, which atomic orbitals are being probed [31] and can even select between different atoms in a compound semiconductor such as GaAs [32].

2.3.2 Feedback Loop

A scanning tunneling microscope must employ a feedback loop in order to control the tip height in constant-current mode. The exponential relationship between current and tip height means that a feedback loop must be employed to determine the exact tip height at which the setpoint is reached [33]. Usually, this takes the form of a Proportional-Integral

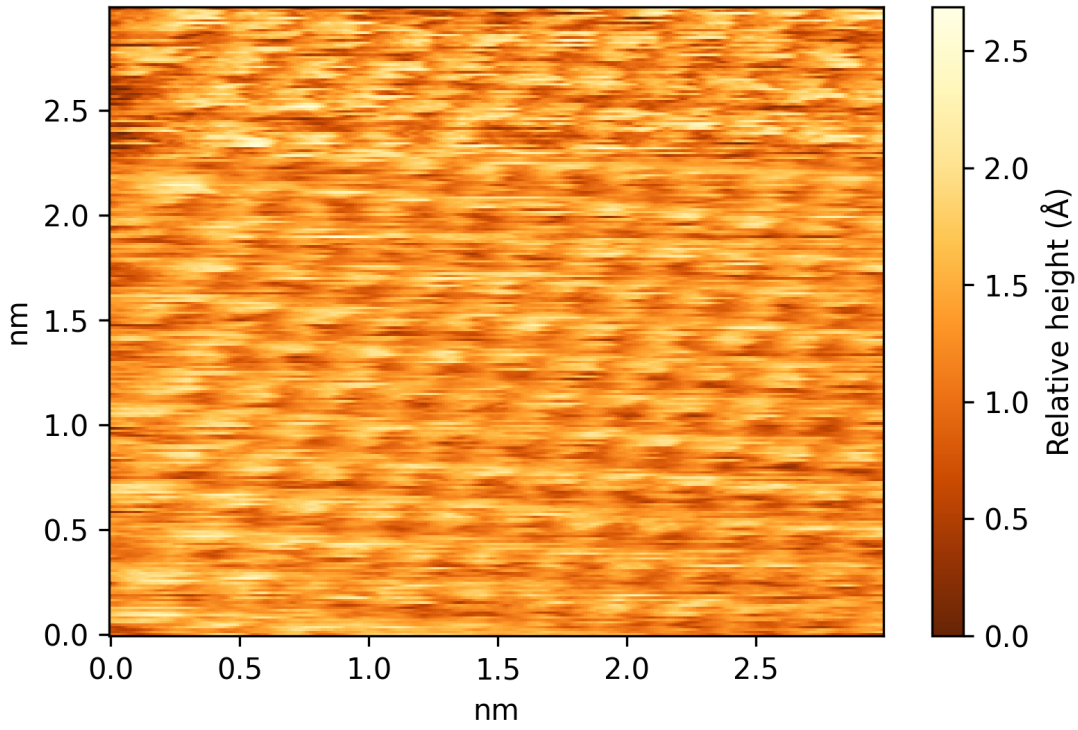

Figure 2.3: STM image obtained under ambient temperature and pressure of the electronic structure of HOPG using a constant current of 0.5 nA. The bias on the tip is 18 mV and the raster scan is 256 by 256 lines. The tip is a PtIr shear-cut tip.

(PI) controller.

A PI controller is based on the following principle: the signal (in the case of an STM, this is the current) is substracted from the setpoint to get the error signal. The goal of a PI is to minimize this error signal by using the following equation [34, 35]:

$$\begin{aligned} i_{\text{setpoint}} - i(t) &= e(t) \\ \Delta z(t) &= Ke(t) + \frac{K}{t_{\text{c}}} \int_0^t e(t)dt, \end{aligned} \tag{2.21}$$

where $e(t)$ is the error signal, K is the Proportional gain, and t_{c} is the integration time constant, of which the latter two are adjustable by the user. In practice, the feedback loop combined with the noise of the STM does not result in perfect tracking of the surface. The current tends to vary a lot due to the exponential nature of the feedback. Whenever a large or tall object is encountered, and the tip retracts upwards to compensate, it may take some time for the tip to come down and make contact. If the tip scans an object right to left, and left to right, this process can result in different images in an effect known as "shadowing". Additionally, sometimes there can be a large jump in tip height due to noise or some other unknown effect. Since the tip can take some time to come down, this can result in an effect known as "streaking".

The frequency response of the feedback loop is also important. We can introduce a low-pass filter in order to filter out high frequency signals. As will be explained later, the current fluctuations induced by STM must be done at a frequency fast enough to not affect the feedback loop of the system.

2.3.3 Tip Radius and Convolution

In the case of a perfectly flat substrate, there are no further considerations for imaging. However, in the case of a tall object on the surface, the atom closest to the surface may not always be the bottom-most one. This results in a convolution of the profile of the tip with the profile of the surface [36]. Usually this results in an apparent broadening of the surface features [37].

One can model the effects of the tip-sample convolution, and possibly deconvolute an image, using algorithms defined by Villarrubia[36]. This model ignores the tip-sample distance and assumes perfect contact between the tip and sample. Additionally, the feedback loop is also not considered for simplicity. The tip radius alone results in an apparent broadening of the underlying features, which corresponds to a mathematical dilation of the

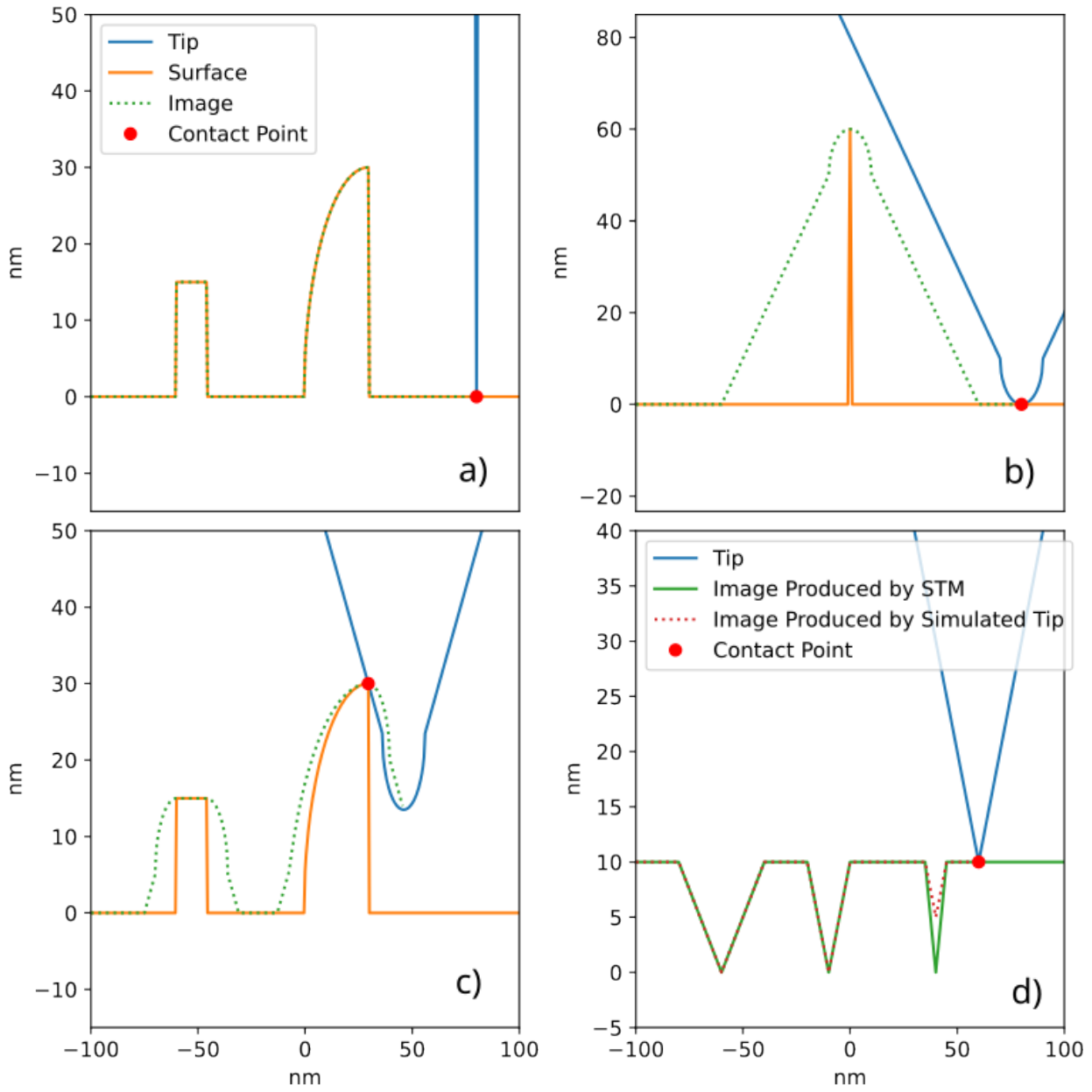

Figure 2.4: A simulation of an STM tip imaging a surface. The simulation assumes direct contact and ignores feedback loop considerations. The simulations have a (**a**) Perfect (dirac-delta like) tip and random sample, (**b**) Dirac-delta sample and an imperfect tip, (**c**) Imperfect tip and the random sample from (a). (**d**) A simulation of a blind tip estimation. The simulated tip can fit in the first two gaps, but not in the last one, indicating that the simulated tip is "larger" than the actual tip used in the STM experiment.

surface features. Once the tip shape is known, a mathematical erosion can be performed to extract the underlying surface features. There are many ways to determine tip profile, such as statistical methods [38], SEM images, and blind tip reconstruction.

Fig. 2.4 shows multiple simulations of tips scanning a surface. In Fig. 2.4(a), a perfect, dirac-delta-like tip is being used to scan a random surface. In this case the bottom-most atom is (almost) always in contact with the surface, leading to the best theoretical scan. However, one must note that any overhangs or caves would not be scanned. Fig. 2.4(b) shows a dirac-delta-like surface and an imperfect tip with radius 30 nm, and a cutoff at 45°. This attempts to simulate the profile of a good tip. In this case, the resulting image is actually of the tip - there is nothing in the math specifying that the sample must be imaged and not the other way around. In this edge case, the convolution is heavily biased towards the tip - the opposite of Fig. 2.4(a). Fig. 2.4(c) shows the imperfect tip from Fig. 2.4(b) interacting with the random surface from (a). The tip is shown mid-scan for clarity, and one can see that the bottom-most atom is not always being used for scanning. This results in an apparent broadening of the surface features.

In some cases, it may be useful to use an algorithm called "blind tip reconstruction". It is used in order to try and estimate a tip shape given a real STM image. An arbitrary tip shape is created, and scanned across the surface. If the simulated tip is able to correctly reconstruct the surface, then the tip profile may be similar to the one actually used. If the tip is unable to recreate the surface, then the actual tip must be "sharper" somehow. For example, as shown in Fig. 2.4(d), the tip is able to fit comfortably in the leftmost hole, and fits perfectly in the middle hole. If the rightmost hole were not present, this would be the upper bound for the tip shape - however, since it cannot fit in rightmost hole, the actual tip used must be sharper. Blind tip estimation is very helpful for establishing an upper bound for the tip shape.

2.4 Scanning Tunneling Spectroscopy (STS)

It is often useful to pick an interesting point of the surface acquired using STM and acquire data on it. In almost all cases, the feedback loop is disengaged while data is taken. The piezos hold their current position and the data is taken at a constant tip height. In practice, this is not perfect due to factors such as drift and thermal expansion. Therefore, one cannot stay at a particular place for too long - the tip will either "crash" into the sample or move too far away. A crashed tip can result in bad imaging and may necessitate a tip change. If in cryogenic operation, these drift factors are reduced and it may even be possible to do "constant-height" STM. However, for the work produced in this thesis it was important to

take data quickly to prevent crashing the tip. Similarly to STM, the bias and setpoint are important - they determine the tip height before the feedback loop is disengaged.

2.4.1 STS: IV and dI/dV

The most common type of spectroscopy is an IV curve. This is done by keeping a constant tip height, sweeping a range of voltages and measuring the tunneling current. The exponential nature of the transmission (as seen in Eqn. 2.19) means that even if a metal is measured, the result will not be ohmic (following $V = IR$). However, for a semiconductor, the doping will lead to an uneven IV curve, with one side having a greater magnitude of current than the other despite the same voltage. Ideally, the current measured at the original bias will match the original setpoint before the feedback loop was disengaged. If the new current is higher, then the tip got closer to the sample, and vice versa. However, noise is always present and there is a noise floor on every measurement (to be discussed later).

The derivative of an IV curve can bring very interesting results. Taking the derivative of Eqn. 2.17, we get the following result:

$$\frac{dI}{dV} \approx \frac{4\pi e^2}{\hbar}[\rho_{\mathrm{t}}(0)\rho_{\mathrm{s}}(eV)T(eV,V,z) + \int_0^{eV} \frac{\partial \rho_{\mathrm{t}}\epsilon - eV}{\partial V}\rho_{\mathrm{s}}(\epsilon)T(\epsilon,V,z)d\epsilon + \int_0^{eV} \rho_{\mathrm{t}}(\epsilon - eV)\rho_{\mathrm{s}}(\epsilon)\frac{\partial T(\epsilon,V,z)}{\partial V}d\epsilon]. \tag{2.22}$$

Although we often assume that the tip DOS is constant, the same cannot be said for the transmission factor, which depends exponentially on voltage. In the barrier-height formalism,

$$T(\epsilon,V,z) \propto e^{-2z\sqrt{\frac{2m}{\hbar}(\bar{\phi}+eV/2-\epsilon)}}, \tag{2.23}$$

therefore, a very complicated model is required to fully extract the sample density of states. Taking only the first term, we can get some approximate idea of this quantity:

$$\frac{dI}{dV} \approx \frac{4\pi e^2}{\hbar}\rho_{\mathrm{t}}(0)\rho_{\mathrm{s}}(eV)T(eV,V,z). \tag{2.24}$$

Although one can simply perform a numerical derivative on an IV curve to extract this data, it is more useful to use a lock-in amplifier technique. The bias is modulated at some frequency, and the effect of that modulation on current is then measured using a lock-in

amplifier. Mathematically, this can be proven by:

$$\begin{aligned} I &= f(V_{\mathrm{DC}} + V_{\mathrm{LIA}}\cos(wt)) \\ I &= \sum_{k=0}^{\infty}(V_{\mathrm{LIA}}/k!)\frac{d^k f}{dV^k}\cos^k(wt). \end{aligned} \tag{2.25}$$

And, using trigonometric identities, we can convert to:

$$I = f(V) + V_{\mathrm{LIA}}\cos(wt)\frac{df(V)}{dV} + \frac{1}{4}V_{\mathrm{LIA}}^3\cos(2wt)\frac{d^2f(V)}{dV^2} + O(V_{\mathrm{LIA}}^2). \tag{2.26}$$

As shown by Feenstra [7], one can 'normalize' the dI/dV signal to deal with the voltage-dependence of transmission. By dividing the LIA signal by the IV curve, one gets:

$$\frac{dI/dV}{I/V} = \frac{\frac{4\pi e^2}{\hbar}\rho_{\mathrm{t}}(0)\rho_{\mathrm{s}}(eV)T(eV,V,z)}{[\frac{4\pi e}{\hbar}\int_0^{eV_0}T(\epsilon,V,z)\rho_{\mathrm{t}}(\epsilon-eV)\rho_{\mathrm{s}}(\epsilon)d\epsilon]/V}. \tag{2.27}$$

Again, assuming that the tip DOS is constant, we get:

$$\frac{dI/dV}{I/V} = \frac{\rho_{\mathrm{s}}(eV)}{\frac{1}{eV}\int_0^{eV_0}\frac{T(\epsilon,V,z)}{T(eV,V,z)}\rho_{\mathrm{s}}(\epsilon)d\epsilon}. \tag{2.28}$$

2.4.2 STS: Iz

An Iz curve is a slightly different measurement than what we have seen. Once the feedback loop is disengaged, the tip is moved away (towards) the sample and the decreasing (increasing) current is measured, using the same bias all throughout. Assuming that at the setpoint we have some current I_0, if we move back by some distance Δz, the transmission factor (see eqn. 2.23) will change, leading to a new current of approximately:

$$I(\Delta z) = I_0 e^{-2\Delta z\sqrt{(\frac{2m}{\hbar}\phi_{\mathrm{eff}})}}. \tag{2.29}$$

Using some clever rearrangement, we can solve for ϕ_{eff} to get

$$\phi_{\mathrm{eff}} = \frac{\hbar}{8m}[\frac{d(ln(I))}{dz}]^2. \tag{2.30}$$

Therefore, one can easily apply an exponential fit and extract information about the apparent barrier height.

Chapter 3

THz-STM Experimental Setup

3.1 Generating THz

This thesis will focus on terahertz generation via a large-aperture photoconductive antenna. When a femtosecond pulse of light hits a semiconducting material with a bandgap smaller than the photon energy of the pulse, free carriers in the form of electrons and holes are generated. These carriers are then accelerated by an external DC bias, and due to their opposing signs, they will travel in opposite directions, thereby generating a transient current. This transient photocurrent will be generated in approximately the same timescale as the pulse duration of the optical beam. This sharp generation of current subsequently generates an electromagnetic wave with the same duration, which is the terahertz radiation. The photocarrier lifetime will generate neglegible radiation due to its (comparatively) higher lifetime. The generated far-field THz generation follows the equation [39]:

$$\mathbf{E}_{\mathrm{THz}}(t) = \frac{\mu_0 w_0}{4\pi} \frac{\sin(\theta)}{r} \frac{dI_{\mathrm{PC}}(t_{\mathrm{r}})}{dt_{\mathrm{r}}} \boldsymbol{\theta}, \tag{3.1}$$

where μ_0 is the permeability of free space, w_0 is the beam spot size, θ is the angle, and $t_{\mathrm{r}} = t - r/c$ is the 'retarded time'. Therefore, the generated THz field is dependent on the generated photocurrent. By changing the optical beam duration, the photocurrent generation time can be changed, which thereby changes the terahertz duration. Due to differences in mobility, the electrons are the dominant carriers. The generation of the photocurrent will depend on the profile of the optical pulse and the response of the antenna:

$$I_{\mathrm{PC}}(t) = \int I_{\mathrm{opt}}(t-\tau) e n(\tau) v(\tau) d\tau, \tag{3.2}$$

where I_{opt} is the optical pulse intensity profile, n is the time-dependent carrier density and v

is the electron velocity. Assuming that the photocarriers are generated instantly, the carrier density will be:

$$n(t) = \begin{cases} 0 & t < 0 \\ n_{\mathrm{pc}} e^{-t/t_{\mathrm{c}}} & t \geq 0 \end{cases}. \tag{3.3}$$

Where n_{pc} is the amount of photogenerated carriers and t_{c} is their corresponding lifetime. In order to control the electron velocity, the DC bias applied across the photoantenna accelerates any generated carriers. Assuming an instantaneous effect again, and using a velocity given by the Drude-Lorentz model, we get [40]:

$$v(t) = \begin{cases} 0 & t < 0 \\ \mu_{\mathrm{e}} E[1 - e^{-t/t_{\mathrm{s}}}] & t \geq 0 \end{cases}, \tag{3.4}$$

where μ_{e} is the electron mobility, t_{s} is the carrier scattering time, and $E = E_{\mathrm{DC}}$ is the static DC electric field. However, there are two factors that prevent infinite linear scaling of terahertz generation [41]. For large carrier densities, excess carriers can screen the DC field. The induced polarization leads to a change in the local electric field of [42]:

$$\begin{aligned} E &= E_{\mathrm{DC}} - \frac{P}{\epsilon \eta} \\ \frac{dP}{dt} &= \frac{P}{t_{\mathrm{r}}} + J \end{aligned}, \tag{3.5}$$

where P is the polarization, ϵ is the dielectric constant, η is a geometric factor, and t_{r} is the recombination time. This is ultimately leads to a fluence dependence of:

$$\mathbf{E}_{\mathrm{THz}}(t) \propto \frac{I}{I + I_0}, \tag{3.6}$$

where I_0 is the saturation intensity. There is also a saturation in terahertz field strength due to large DC biases. For electric fields in the few-kV range, the electron mobility has been shown to saturate [43].

For our experiments, we use a GaAs photoconductive antenna (Laser Quantum, TeraSED). GaAs has a bandgap of 1.42 eV which is less than the photon energy of 1.55 eV for 800 nm light. In addition, the photocarrier lifetime of GaAs is longer than the terahertz pulse duration, which is important for generation [44]. This is placed on a rotational mount, and by rotating the crystal it is possible to rotate the polarization of the generated THz beam.

3.2 Detecting THz

Detecting terahertz radiation is typically done through electro-optic sampling (EOS). Experimentally, we employ a flip-mirror to pick off terahertz radiation into an EOS line, where great care is taken to recreate the same optics and path length of the experimental line. This way, the terahertz at the EOS detector will match the far-field terahertz at the experiment. The outline is as follows: a polarized, femtosecond optical pulse is sent through a ZnTe crystal, a quarter waveplate, then through a Wollaston prism, then into two balanced photodetectors. In the absence of THz, the Wollaston prism splits the pulse into two equal intensity, oppositely polarized beams, and the photodetectors read equal amounts of signal. In the presence of terahertz, the terahertz will electro-optically induce a temporary birefringence in the ZnTe, which modifies the passing probe beam, which ultimately results in the photodiode signals being uneven. This signal will be a convolution of the probe beam and terahertz beam, however the shorter duration of the probe beam produces a waveform that approximates that of the terahertz. By changing the delay between the probe and THz pulse, it is possible to get the entire waveform of the THz pulse.

The terahertz beam induces a birefringence in the ZnTe crystal via the Pockels effect (also known as the linear electro-optic effect), which is only possible in non-centrosymmetric materials. In a non-centrosymmetric crystal under an incident electric field, the i-th component of polarization will be [39]:

$$P_{\mathrm{i}}(w) = P_{\mathrm{i}}^{(1)}(w) + P_{\mathrm{i}}^{(2)}(w) + O(E^3), \tag{3.7}$$

where the Pockels effect relates specifically to the second order polarization,

$$P_{\mathrm{i}}^{(2)}(w) = 2\sum_{j,k} \epsilon_0 \chi_{\mathrm{ijk}}^{(2)}(w, w, w=0) E_{\mathrm{j}}(w) E_{\mathrm{k}}(w=0), \tag{3.8}$$

where χ is the second order suspectibility tensor. This shows the Pockels effect: an incident electromagnetic wave with frequency w, and some polarization j, combines with a static DC electric field (with frequency $w = 0$) with direction k, resulting in an induced polarization in direction i with frequency w. For our EOS, the probe beam acts as the incident wave and the terahertz field acts as a quasi-static DC field. The Pockels effect leads to a phase change in the probe beam of:

$$\Delta\phi = (n_{\mathrm{y}} - n_{\mathrm{x}}) wL/c = (n_{\mathrm{optical}} r_{41} E_{\mathrm{THz}}) wL/c, \tag{3.9}$$

where n_{optical} is the refractive index of ZnTe at the probe-beam frequency, r_{41} is an electro-

optic coefficient, and w is the frequency of the optical beam. Therefore, the two photodiodes will see a change in signal:

$$\begin{aligned} I_{\mathrm{x}} &= 0.5I_0(1 - \sin(\Delta\phi)) \\ I_{\mathrm{y}} &= 0.5I_0(1 + \sin(\Delta\phi)), \end{aligned} \tag{3.10}$$

where I_0 is the initial intensity of the beam. One can solve for E_{THz} to get:

$$E_{\mathrm{THz}} = \frac{c}{wLn_{\mathrm{optical}}r_{41}}\Delta\phi \approx \frac{c}{wLn_{\mathrm{optical}}r_{41}}\frac{I_{\mathrm{y}} - I_{\mathrm{x}}}{I_{\mathrm{y}} + I_{\mathrm{x}}}. \tag{3.11}$$

Therefore, one can obtain the terahertz field strength using the photodiode measurements. As mentioned before, the response will be a convolution of the probe and THz beams, for which the probe acts like a dirac-delta function. By sweeping the delay between the probe and THz beams (achievable using motorized stages), one can map out the entire terahertz pulse. An experimental electro-optically sampled waveform is shown in Fig. 3.1. Although there is a small day-to-day fluctuation in the laser / THz power and alignment, this graph is a good indication of what the parameters are like for almost all the THz-STM experiments shown in the later chapters. Notably, the absolute value of the peak electric field for positive and negative polarities is not exactly equal. If the THz generation beam is slightly off-center on the THz antenna, rotating the antenna will make the generation beam hit a different area, whose local properties can affect the efficiency of THz generation.

The parameters of ZnTe are $n_{\mathrm{optical}} = 2.8$ at $\lambda = 800$ nm, $r_{41} = 4.0 \times 10^{-12}$ m/V, and a transmission factor of 0.48.

3.3 THz-STM

3.3.1 Coupling THz Pulses to an STM

When a terahertz pulse is incident on an STM tip, the tip will act as an antenna and focus the wave into the tunneling junction. The terahertz pulse at the junction is known as the near-field, to differentiate it from the terahertz prior to hitting the junction which is known as the far-field THz. The near-field experiences field enhancement, which increases the electric field strength by seveal orders of magnitude. Early simulations showed field enhancements of 28 [5], but different tips show enhancements of 10^4 to 10^5 [45]. Experimental data for field enhancement ranges from 28 to 10^5 [1, 5, 25].

The shape of the terahertz pulse is also affected due to coupling. High-frequency components are suppressed [46]. The STM tip can be modelled as an RLC circuit, however,

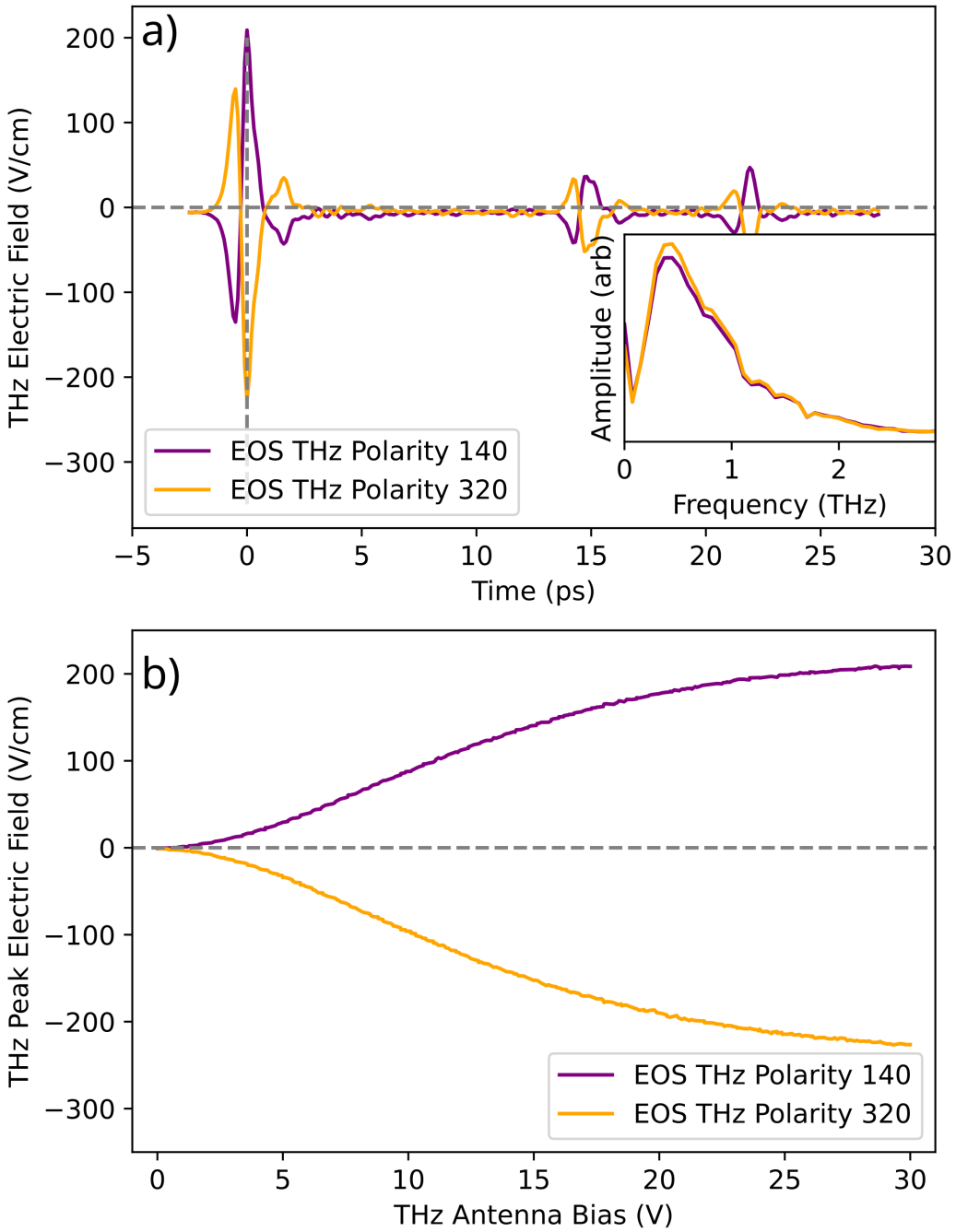

Figure 3.1: An experimental electro-optic sampling of a terahertz pulse, corresponding to one of the THz plots shown in later chapters. The polarity refers to the angle of the THz antenna, which yields a maximum signal at angles of 140 and 320 degrees. (**a**) Temporal profile of the THz pulse, achieved by sweeping the delay between the THz and probe beams. The timescale has been set such that the maximum of the pulse ocurrs at time t=0. The antenna bias is 30 V and the smaller pulses are due to reflections in the optics. The inset shows the FFT spectrum of the pulse. (**b**) Effect of sweeping the bias on the antenna at the peak of the wave, which is at t=0.

the specific parameters are dependent on geometry and will vary from tip to tip. Simulation and experimental data have shown values of R, L, C in the few-hundred Ohms, 10's of nH, and 35 fF, respectively. Simulation-wise, the profile of the near field resembles the integral of the far field.

When the terahertz is incident on the junction, it will act as a voltage on the sample. We assume that the temporal profile of the applied terahertz voltage ($V_{\mathrm{THz}}(t)$) matches the profile of the near-field. The peak voltage generated by the THz depends on the field strength, tip material and geometry. Simulations have shown that the bias can reach up to 3 V peak. Published ambient THz-STM data shows peaks of 0.3-0.4 V, and published UHV data shows peaks of 2-10 V [46, 47], although higher voltages are possible.

The time-dependent terahertz voltage will be added to the DC bias $V_{\mathrm{DC}} \rightarrow V_{\mathrm{DC}} + V_{\mathrm{THz}}(t)$ to create a time-dependent current $I_{\mathrm{DC}} \rightarrow I_{\mathrm{DC}} + I_{\mathrm{THz}}(t)$. Due to the nonlinear form of Eqn. 2.17, the resulting terahertz current will be highly dependent on the setpoint chosen. The terahertz bias and currents, at ultrafast speeds, are too fast for any electronics to measure. However, there is a rectification present due to the nonlinearity of the I-V curve, which can be seen in Fig. 3.2. The THz far-field and near-fields must satisfy the wave property of:

$$\int_{-\infty}^{\infty} E_{\mathrm{THz}}(t)dt = \int_{-\infty}^{\infty} V_{\mathrm{THz}}(t)dt = 0. \tag{3.12}$$

However, due to the non-linearity of the IV characteristics, the rectified terahertz current does not have to satisfy this equation, as seen in Fig. 3.3. After the transient bias, there is a rectified charge:

$$Q_{\mathrm{THz}} = \int_{-\infty}^{\infty} I_{\mathrm{THz}}(t)dt, \tag{3.13}$$

which does not necessarily have to be zero. Therefore, assuming the right bias is chosen and that they have the same tip height, an experiment with THz incident on the junction will experience more current than an experiment without THz. Thankfully, we are able to measure the average terahertz current over a large time interval:

$$I_{\mathrm{THz,avg}} = f_{\mathrm{rep}} Q_{\mathrm{THz}} = f_{\mathrm{rep}} e N_{\mathrm{e/pulse}}, \tag{3.14}$$

where e is the electron charge, $N_{\mathrm{e/pulse}}$ is the number of rectified electrons per pulse, and $f_{\mathrm{rep}}(= 250\ \mathrm{kHz})$ is the repetition rate of the laser.

The sharp resolution of STM is still present in THz-STM. This is due to two reasons: the field enhancement only ocurrs at the end of the tip, and the electronic tunneling properties only occur at the junction. THz-STM has been shown to have a temporal resolution under 500 fs and a spatial resolution of 2 nm in ambient [1], while UHV-THz-STM has a

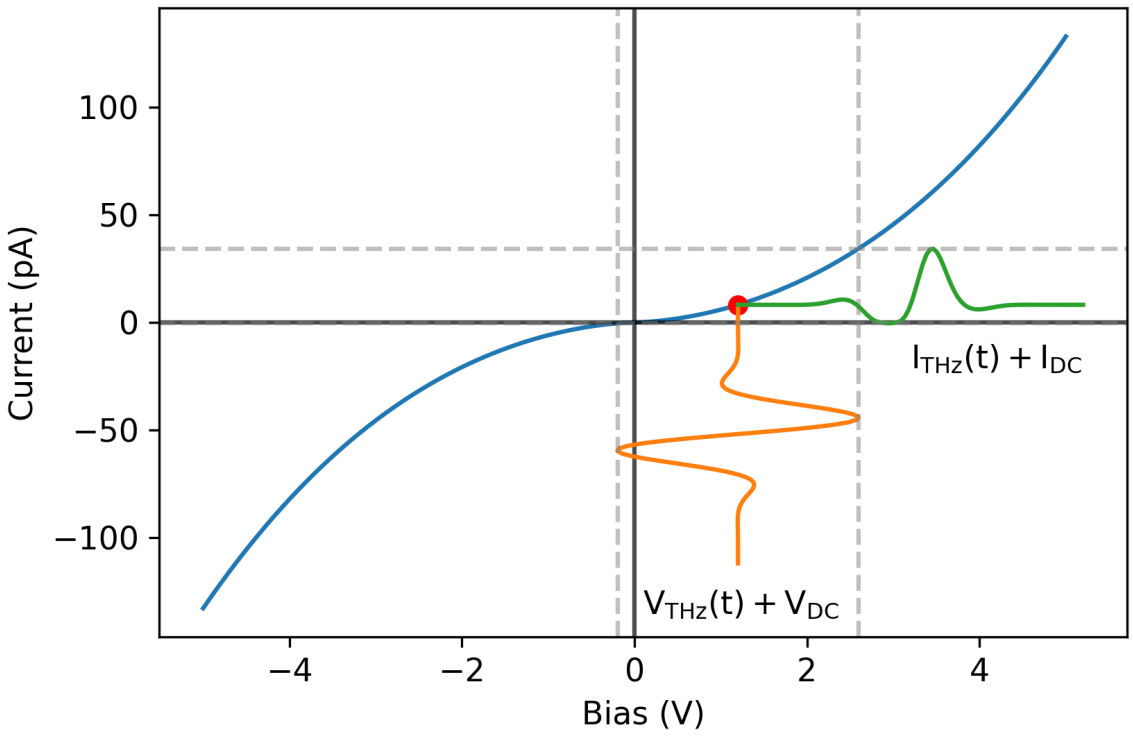

Figure 3.2: This image shows the terahertz-induced voltage transient interacting with the IV curve present in the junction. The terahertz pulse, shown in orange, provides a time-dependent modulation around a DC value. This results in a time-dependent tunneling current shown in green. The maxima and minima of the functions are shown with dashed lines for clarity. The terahertz near field and terahertz-induced voltage ($V_{\mathrm{THz}}(t)$) must satisfy the property that their integral is zero. However, the integral of the terahertz current ($I_{\mathrm{THz}}(t)$) is nonzero and therefore measurable with conventional electronics as shown in Fig. 3.3. The model, chosen arbitrarily, has a DC setpoint of 8 pA, DC bias of V_{DC}=1.2 V, and a THz modulation amplitude of $V_{\mathrm{THz,peak}}$=1.4 V.

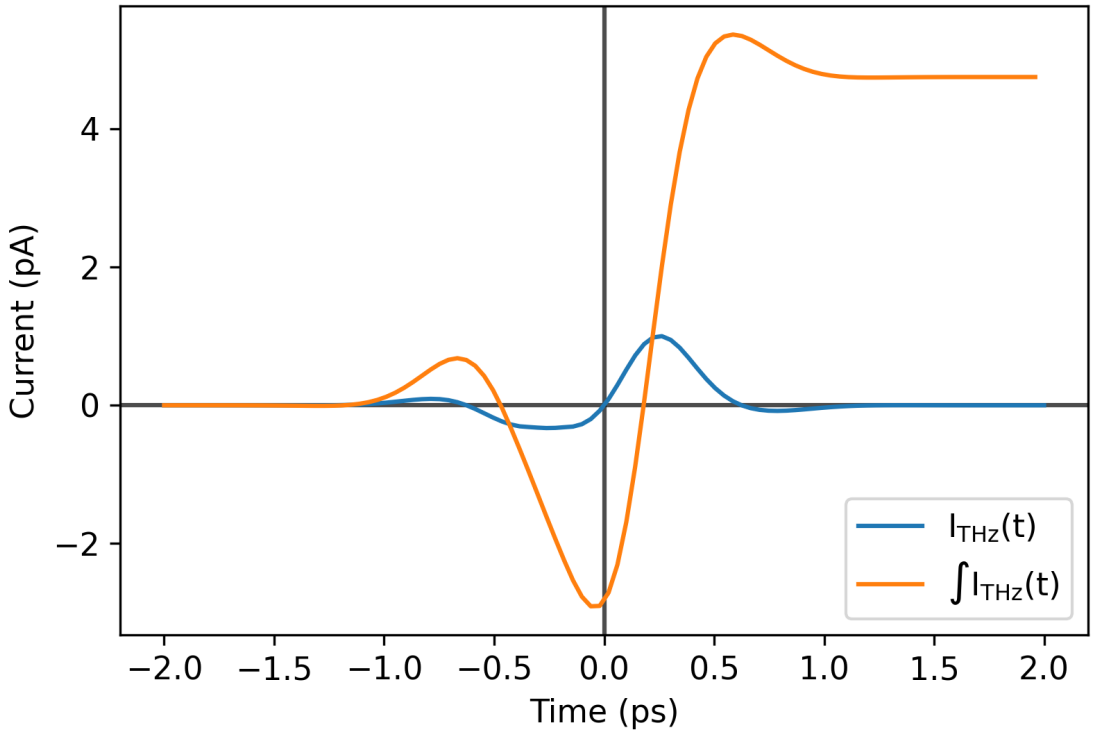

Figure 3.3: The time-dependent terahertz current, $I_{\mathrm{THz}}(t)$, which comes about due to the THz-induced voltage. The current is taken from Fig. 3.2. Although the terahertz current is not measurable using conventional electronics, it is possible to obtain the rectified charge $Q_{\mathrm{THz}} = \int_{-\infty}^{\infty} I_{\mathrm{THz}}(t)dt$.

sub-nanometer spatial resolution [5].

3.3.2 THz-STM Spectroscopy

The introduction of THz into an STM allows for a larger variety of experiments that can be performed. Similar to an STM scan, a THz-STM can also scan a surface. However, this THz-STM scan can be done with some or no DC bias (the latter is known as Terahertz Driven STM, or TD-STM). These THz-based scans can reveal defects and subsurface features [5, 18, 25]. It is possible to take regular STM spectroscopes, such as IV and Iz, with the THz field applied to the tip. Oftentimes, an IV curve with THz enabled is useful for finding a good bias at which the THz current is strongest. As seen in Fig 3.2, the bias can have a significant effect on the measured current. Additionally, an "IE" can be taken. In this case, I refers to I_{THz} and E refers to E_{THz}. As suggested by its name, this involves increasing the THz electric field strength, which usually results in a nonlinear increase in the rectified THz current.

An important type of spectroscopy is Optical Pump / THz-STM Probe (OPP-THz-STM). This type of spectroscopy introduces an optical-frequency laser that pumps the surface, which is then probed by coupling the THz to the tip. This type of spectroscopy is described in more detail in the next chapter.

3.4 Electronics

Lock-in amplifiers (LIA) are able to measure signals at incredibly high frequencies, making them critical for use in THz-STM. THz beams are created at a rate of 250 kHz, the repetition rate of the laser, but there is an additional modulation applied on the terahertz creation. This is done by applying a square wave bias modulation on the terahertz antenna, turning it on and off at a rate of 5077 Hz. This is done to prevent the antenna from being damaged from excess current. Additionally, by setting up the lock-in amplifier to measure that frequency, the current with THz and without THz can be measured, which is substracted in-situ to obtain the average terahertz current. This is also done to control the tip height modulation. The feedback loop has a low-pass bandwidth, and by modulating the terahertz at a higher frequency this makes it so that the tip does not oscillate quickly. Therefore, the tip height does not change between periods of THz / no THz, which means that any changes in current are due only to the THz and not due to a tip height change.

The feedback controller bandwidth and currents are dependent on electronic pre-amplifiers. The STM uses a two-stage amplifier setup. The first amplifier, the IVP-

(100/200/300) has a high gain of (10^7,10^8,10^9) V/A and a bandwidth of (250/50/5) kHz, respectively. Their frequency responses can be found in reference [25]. The second amplifier, the IVP-PGA, has a unity gain and a customizable low-pass filter which is set to 5 kHz, meaning that the 5.077 kHz THz antenna modulation is sufficiently beyond the feedback loop response. Experimentally, the preamplifier gain controls which setpoints will result in stable images. The IVP-300, which is the only one used for this thesis, allows setpoints of up to 1 nA. However, the tip will be unstable in this configuration. Currents of 250 pA to 2 pA are possible with the IVP-300, and higher currents would be better with a lower gain. Additionally, since the IVP-300 allows for the smallest currents, it is preferable for THz-STM due to less background DC current.

The values measured by the lock-in amplifier must be calibrated, as the raw data cannot be exactly related to the current. One way to calibrate the THz field is to apply a small DC bias and a very low setpoint. The THz field is increased until the DC current is zero. Therefore, one can equate the setpoint and the terahertz current. Another calibration method is to thoroughly multiply the gains and lock-in amplifier sensitivities to obtain a calibration constant. However, these methods give slightly different results, meaning that this is still a matter of debate. New calibration methods are currently being investigated.

Lock-in amplifiers are also important when taking dI/dV data. LIAs can provide the bias modulation needed, and can measure the resulting change in current.

3.5 Experimental Setups

There are two STMs in this thesis from which data was acquired. The primary STM, used in previous works, is equipped with UHV and THz-STM capabilities. The secondary STM is an ambient system used for quick study of samples, and has no UHV or (current) THz-STM capabilities.

3.5.1 THz-STM

The primary STM used is a commercial system (RHK Technology, RHK-UHV-SPM 3000), which can be seen in Fig. 3.4. The system is stabilized using an active vibration isolation system (TMC, STACIS 2100/3000), which detects and filters out vibrational noise using piezoelectric actuators. Samples can be cooled down to (100/30) K using liquid (nitrogen/helium) using an open-flow cryostat (CryoIndustries, RC-110). These liquids are stored in refillable dewars.

This STM has a base capability of 5×10^{-11} torr, although in practice it is usually

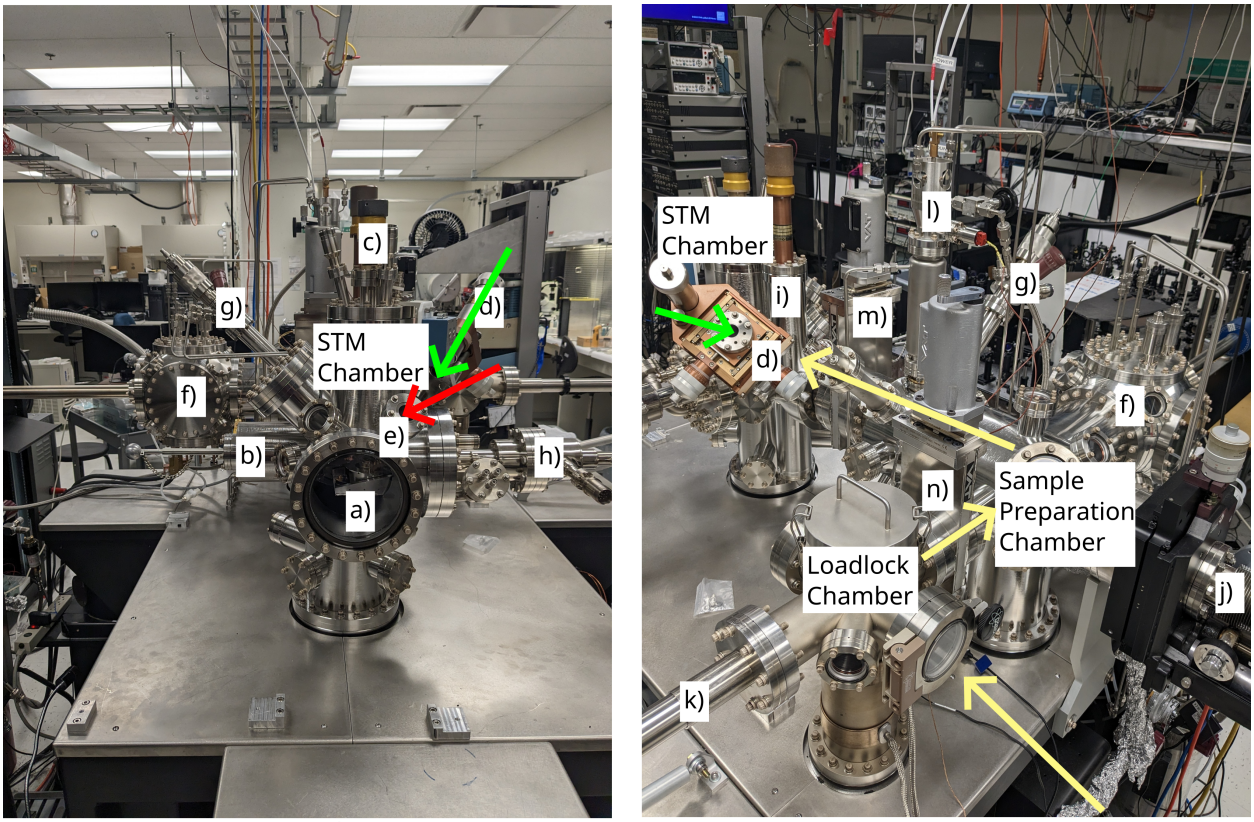

Figure 3.4: Images of the THz-STM system. As this photo was taken prior to bakeout, several optical breadboards and cables are missing, allowing a better view of the STM. The leftmost image shows the STM from the front and the rightmost image shows the STM from the back.

lower by an order of magnitude. The loadlock chamber contains a roughing pump (Agilent, IDP-7) which can reduce pressures from ambient to 10^{-2} torr. The loadlock chamber also has a turbomolecular pump (Leybold, TURBOVAC-TW70H) which can reduce pressures from 7.5 torr (2 torr in practice) to 7.5×10^{-8} torr. The STM and sample preparation chambers both contain ion pumps (Gamma Vacuum, 300T-DI) which can reduce pressures from 7×10^{-4} torr to 10^{-12} torr. Under normal operation, all doors between chambers are closed. When we want to introduce a new sample or tip (see Fig. 3.4), it must first be inserted into the loadlock chamber. Then, the roughing and turbo pumps bring down the pressure while the sample is baked at 130 °C overnight. This is done to remove any organic compounds which cannot be filtered by the ion pumps. Once the sample has cooled down, the door between the loadlock and sample preparation chambers (n) is opened, and the sample is moved using the loadlock transfer arm (k) to the sample preparation transfer arm (j). The door is closed, then the STM to sample preparation chamber door is opened (m) and the sample is brought into the STM chamber. Samples and tips may be stored in the sample elevator (i) or on a copper mount or STM stage (a). This is done using the wobble stick (b). For scanning, the roughing and turbo pumps must be turned off due to their vibrational noise, but the vacuum is maintained in the STM and sample prep. chambers via the ion pumps. Samples may be modified in UHV using a deposition chamber (f), an electron gun (g), or an argon bombardment chamber (i). The STM tip can be raised or lowered using the scanhead controls (c).

Although Fig. 3.4 does not show the optical breadboards for clarity, there are usually several breadboards attached around the STM with all the THz and pump optics. The pump enters the STM via a viewport (e), and can be controlled via mirrors on the breadboard. The THz beam enters the STM via another viewport (d). There are mirrors on the breadboard, and the viewport has a TPX lens which may be controlled using external knobs, giving further control to the beam direction.

3.5.2 Tips

The creation and treatment of sharp tips is one of the most important factors for THz-STM. The microscopic profile of the tip controls the stability of tunneling and resolution of images. The tip shape can affect the ability to get atomic-quality scans [48, 49]. The mesoscopic profile controls the antenna properties of the tip, and can lead to a vast difference in THz-STM results. Although STM tips have been studied extensively, there is more work required for tips intended for use in THz-STM.

We use a simple-submersion electrochemical etching method for creation of tungsten

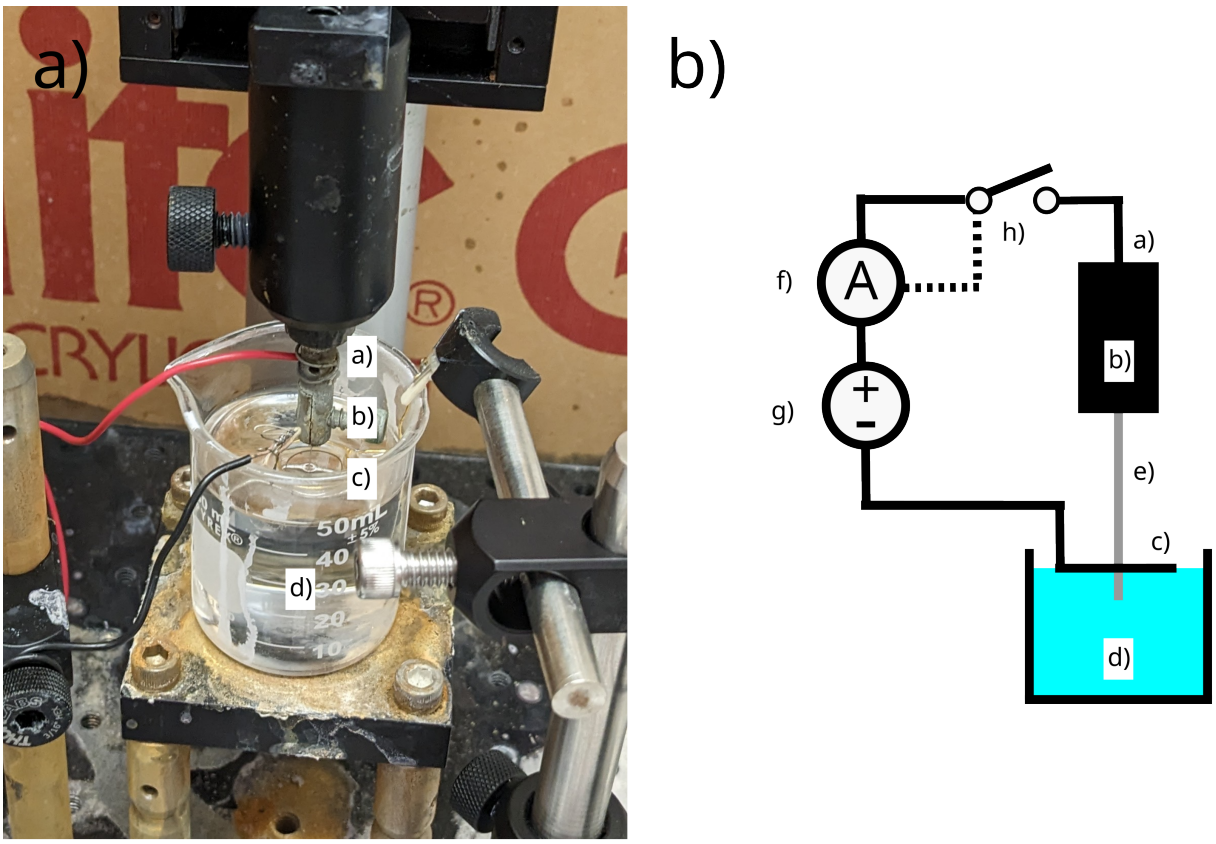

a) Metal Ring (on clamp)
b) Clamp (holding a tip)
c) Metal Ring and Meniscus
d) Etching Solution
e) Metal Tip
f) Anmeter
g) Voltage Source
h) Cutoff switch

Figure 3.5: Images of the tipmaking process. (**a**) A photo of the tip-making station as it is currently set up. The image was acquired during the creation of a tungsten tip, and the current solution of 2 M NaOH. (**b**) A diagram of the tip etching process and corresponding circuit diagram.

(W) and gold (Au) tips, which can be seen in Fig. 3.5. A large spool of tungsten is sanded to remove surface oxides and cut into 1-2 cm pieces. It is then inserted into a solution of 2 M Sodium Hydroxide (50ml deionized water + 4g sodium hydroxide), and a bias of 4 V is applied across the wire and the solution. The bias is applied to the solution via a metal ring which is placed on the meniscus of the solution. This begins the etching, which will slowly sharpen the tip of the wire and reduce the current across it. Eventually, the wire will break, resulting in the creation of a sharp tip, and the current will be reduced dramatically. It is important to cutoff the voltage as quickly as possible to prevent the tip from getting blunter, and this is done by switching the circuit off once the current is under 1 mA. For gold tips, a similar process is done but no sanding is needed, a 1:1 solution of 95% ethanol and hydrochloric acid is used, and a 4.5 V bias with a 0.5 mA cutoff is used. In order to prevent oxidation, W tips must be stored in UHV or methanol, making them ineffective for ambient STM. Another tip making method is to shear PtIr wire at a 45 degree angle, creating a sharp edge on one side of the wire.

Once tips are made, they will not be perfectly sharp. Tips may be modified on a copper stage, which is located near the STM stage (see Fig. 3.4, label (a)). Electron bombardment is done on the tip to induce strong reshaping. As the name implies, electrons are ejected from a filament by applying a bias of 150-200 V, leading to a current of 1 mA. After that, one or multiple rounds of field emission are done. In this method, a voltage of 600-4000 V is applied to the tip resulting in emission of up to 100 nA (if this limit is reached, the voltage is decreased to reduce current). Finally, scanning a surface at high speed, voltage and current can induce tip reshaping.

3.5.3 Optical Setup

In order to perform THz-STM, we require a variety of optics and lasers, which can be found in Fig. 3.6. The optical pulses used have a central wavelength of 800 nm, a full width half max of 77 fs, and are shot at a repetition rate of 250 kHz. They come from a commercial laser, the Coherent RegA 9050, which is a regenerative amplifier with a Ti:Sapphire crystal. The RegA crystal is pumped by the Coherent Sprout (CW laser at 532 nm) and the Q-switch is Coherent Micra. All three systems require a stable temperature, achieved using liquid-cooling chillers, to have stable laser emission. The pulse is amplifier using the principles of chirped pulse amplification, as it passes through a compressor after the RegA. The compressor is tunable and allows for tuning of the pulse width, and therefore the terahertz pulse width.

This ultrafast beam is split off for several uses, including a photodiode for timing, EOS probe beam, terahertz generation and as an optical pump. The optical pump is used

for photoexciting samples. Using a single-lens or double-lens configuration, the pump can be focused onto the sample. For semiconductors with a bandgap of under 1.55 eV, the original 800 nm pump beam is sufficient to excite the sample. However, with semiconductors with a larger bandgap, we can use a BBO (Barium Borate) crystal for second harmonic generation to 400 nm, which corresponds to a 3.1 eV bandgap. Both the pump and THz optical setups can be seen in Fig. 3.6.

3.5.4 Ambient STM

Designed for a rapid turnaround of samples, the ambient STM can be seen in Fig. 3.7. The location and mount of the system during data acquisition is different than that in the figure, and it is currently stabilized using piezoelectric actuators (TMC, LaserTable-Base). As it is made by the same manufacturer as the THz-STM, it has interchangable sample holders. Additionally, the stage for STM, as seen in Fig. 3.7(b) is almost identical to the one used in the UHV-STM.

The ambient system also has the ability to create a high vacuum. The system has a roughing pump (Agilent, IDP-7) and a turbomolecular pump (Shimadzu, TMP-B300). Since these must be off during scanning, the system is also equipped with a non-evaporable getter (CapaciTorr, CF 35 NEG) which serves as a passive way to maintain ambient once the pumps have been disengaged. For an overnight pumping, we can achieve pressures of 10^{-6} torr.

Similarly to the UHV-THz-STM, the Ambient STM has two preamplifiers. The ambient system has a current to voltage amplifier (RHK, Femto DLPCA-200 Transimpedance Amplifier) and a gain amplifier (RHK, IVP-R10 Programmable Gain Amplifier). The Femto amplifier has a gain from $10^3 - 10^9$ for the low noise setting and $10^5 - 10^{11}$ for the high speed setting.

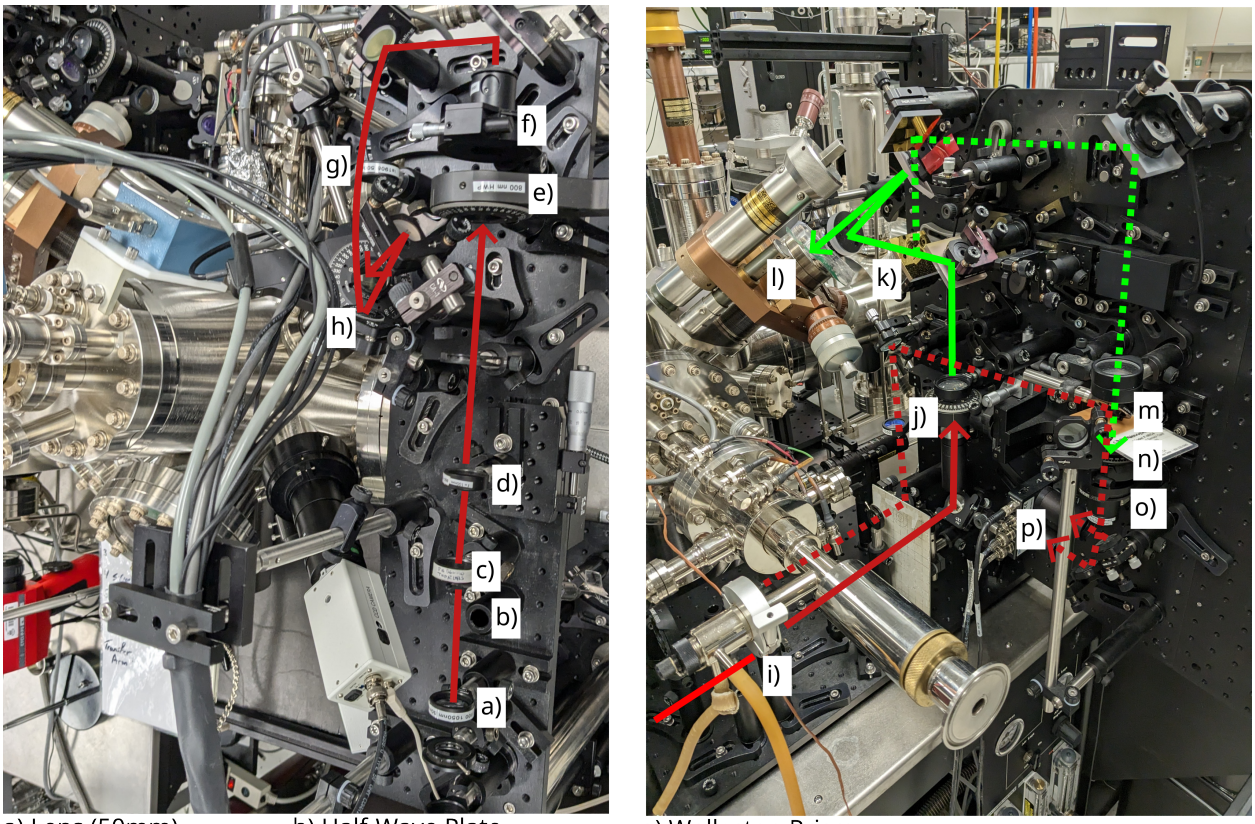

a) Lens (50mm)
b) BBO (Optional)
c) Filter (Optional)
d) Lens (100mm)
e) Half-Wave Plate (Pump Power)
f) Polarizer
g) Lens (500 mm)
h) Half-Wave Plate (Pump Polarization)
i) Flip Mirror (Optional)
j) THz Antenna
k) Gold Flip Mirror (Optional)
l) THz Entry Viewport
m) EOS Probe Mirror
n) ZnTe Crystal
o) Wollaston Prism
p) Balanced Photodiodes

Path: Pump / THz Generation Beam
Path: EOS Probe Beam
Path: THz (to STM)
Path: THz (to EOS)

Figure 3.6: Images of the THz-STM, with an emphasis on the optics. The leftmost image (rotated 90 degrees for clarity) shows the pump optics experimental setup. It is currently set up with a 'single-lens' configuration, where a collimated beam enters an f=500mm lens (**g**) and is focused onto the junction. A double-lens configuration would replace **g** with a 300 mm lens, and insert a 50 mm lens just before the viewport. The second configuration leads to a tighter spot size, which is experimentally harder to align. The rightmost image shows the THz generation, detection, and entry into the viewport. Beamblocks are inserted at **k** and below **l** when in regular STM mode. For THz-STM, there are two optional flip mirrors: (**i**) blocks the generation of THz, and (**k**) can be used to block the THz from entering the junction after generation by sending it into the EOS line. The pump and THz generation beams are both 800 nm beams from the same source, although an optional BBO (**b**) can frequency double the pump to 400 nm.

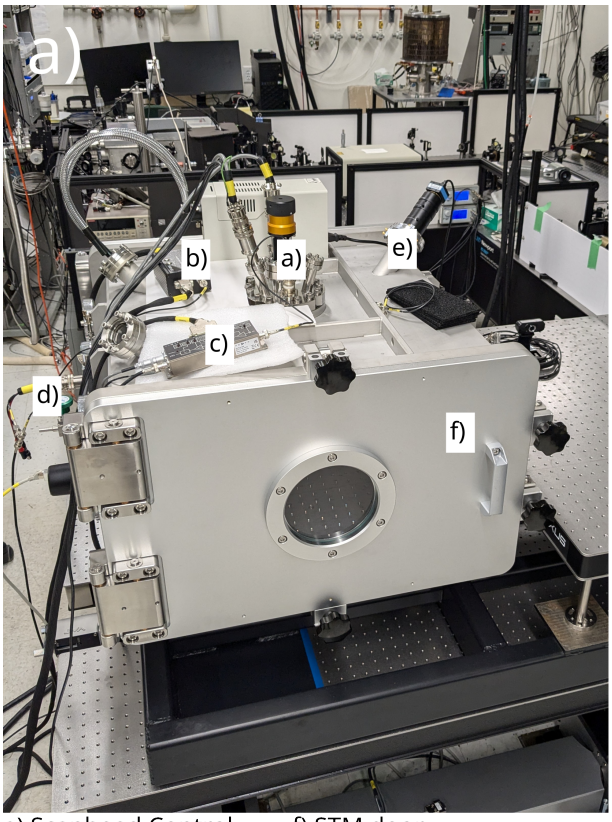

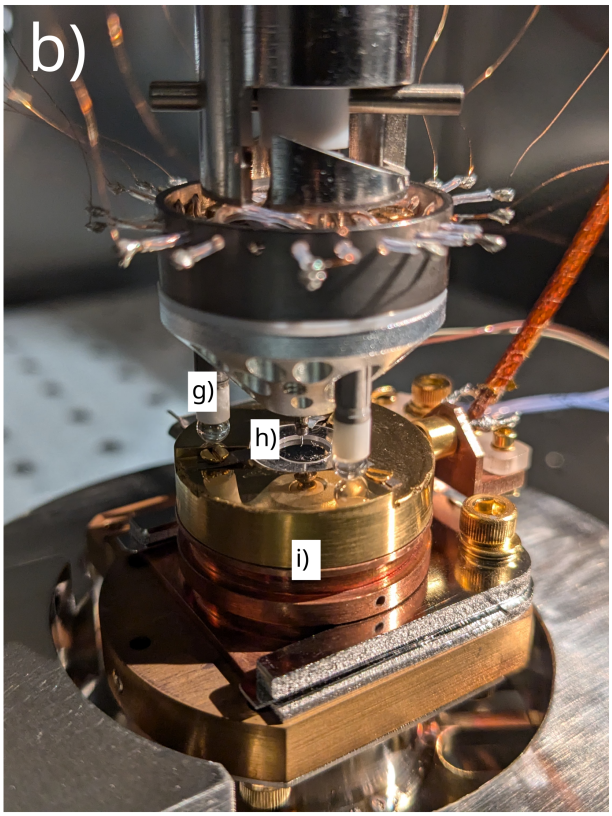

a) Scanhead Control
b) IVP R-10
c) Femto Preamplifier
d) Air Release
e) CCD Camera
f) STM door
g) Beetle legs
h) Tip and Sample
i) Sample Holder

Figure 3.7: Images of the ambient STM. Although the setup was slightly different during data acquisition for this thesis, the difference between setups is negligible for the results. (**a**) The outside of the ambient STM. (**b**) Inside of the ambient STM, showing the STM junction, which is almost identical to the one in the UHV STM. The STM "Beetle" lands on the sample holder using a three legs containing piezoelectric motors, where it can then approach further until tunneling distance is reached.

Chapter 4

Photoemission Sampling of the THz Near-field

In addition to coupling THz, an important THz-STM experiment is an Optical Pump - Terahertz-STM Probe experiment using (also known as OPP-THz-STM, or pump-probe for short). For this experiment, an optical pulse "pumps" a surface, photoexciting it, and then a THz beam couples to the STM tip and probes the surface.

Similar to THz beams, there is also a degree of field enhancement for optical frequency pulses incident on an STM tip. Depending on the angle, field enhancement can reach up to 270 for an Au tip and 6 for a regular W tip[1]. The enhancement is dependent on tip to wavelength ratio, opening angle, polarization, angle of incidence, and other tip geometry factors [50–52]. In order to excite a semiconductor, the photon energy must exceed the bandgap. We can use a 800nm/1.55 eV pump or a 400 nm/3.1 eV pump that has been frequency-doubled to achieve this excitation.

4.1 Pump-Probe Theory

When a pump beam photoexcites a surface, it creates a transient surface photovoltage and creates free charge carrier pairs in the sample. This transient increase in carriers n will therefore increase the amount of carriers rectified by the THz probe. Without any photoexcitation, the number of free carriers in the sample will just be equal to the LDOS value, which is $\rho_s(\epsilon)$. Although a model including rise time and a gaussian distribution may be used, for our purposes we will assume a simple impulsive excitation, leading to a time-dependent

[1] According to ref [50], W nanotips can result in a two-fold increase in field enhancement

carrier concentration of:

$$n(\epsilon, t) = \begin{cases} p_{\mathrm{s}}(\epsilon) & t < 0 \\ p_{\mathrm{s}}(\epsilon) + n_{\mathrm{pumped}} e^{-t/\tau} & t \geq 0 \end{cases}. \tag{4.1}$$

where n_{pumped} is the maximum amount of photoexcited carriers, and τ is a generic carrier decay parameter. We can now modify our current equation to get:

$$I_{\mathrm{THz}}(t, \Delta t) \propto \int_0^{e(V_{\mathrm{DC}}+V_{\mathrm{THz}}(t))} T(\epsilon, V_{\mathrm{DC}} + V_{\mathrm{THz}}(t), z)\rho_{\mathrm{t}}(\epsilon - eV_{\mathrm{DC}})n(\epsilon, t + \Delta t)d\epsilon \tag{4.2}$$
$$\Delta t = t_{\mathrm{pump}} - t_{\mathrm{THz}}.$$

This is a convolution between the terahertz pulse, carrier density, and transient photoconductivity. Experimentally, one can obtain the entire spectrum of I_{THz} by sweeping the time difference Δt. This is shown graphically in Fig. 4.1. For cases when the THz beam arrives before the pump excitation, as shown in 4.1(a), the THz signal will rectify electrons before the surface photovoltage is created, giving identical results to an experiment without a pump beam. For cases when the THz beam arrives after the pump, as shown in 4.1(b), there may or may not be a leftover surface photovoltage (this depends on the decay rate τ), which will lead to an increased THz current. For cases when the THz and pump beams intersect, the result will depend strongly on τ. There are two limiting cases: in the case of a large τ, the profile of $I_{\mathrm{THz}}(t)$ will match that of $V_{\mathrm{THz}}(t)$ and can be used to detect the near-field. In the case of a small τ, $I_{\mathrm{THz}}(t)$ will resemble $n(\epsilon, t)$.

4.2 Photoemission

4.2.1 800 nm Photoemission

Whenever an optical pump is shined on an STM tip, electrons are ejected from the tip and sample. The main process that controls emission is multiphoton emission [18]. The Keldysh parameter $\gamma = \frac{w}{eE_{\mathrm{pump,max}}}\sqrt{2m_{\mathrm{e}}\Phi}$ (where w is frequency, $E_{\mathrm{pump,max}}$ is the maximum electric field strength of the pump, and Φ is the work function) indicates multiphoton emission for values greater than 1.

Once electrons have been emitted, the voltage difference across the tip-sample junction accelerates the electrons. The direction and magnitude of the electric field controls the effect. This can be seen in the IV shown in Fig. 4.2. When the sample is positively biased, electrons from the tip are accelerated towards the sample, and vice versa. Usually, a positive

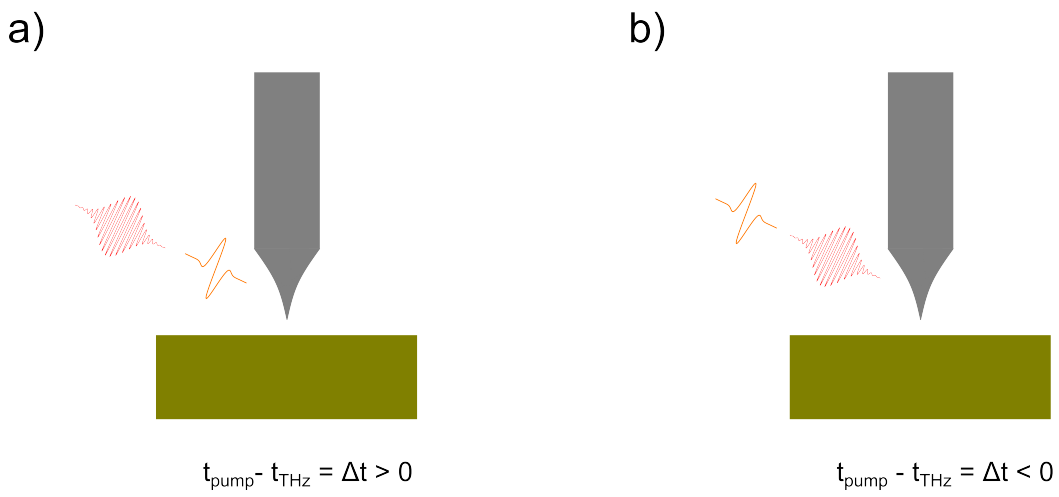

Figure 4.1: Diagram showing the pump and THz pulses incident on an STM tip for a photoemission or pump-probe experiment. The time $t_{\mathrm{pump,THz}}$ represents when the pump and THz pulses hit the junction, respectively. Note that although the beams are colinear in this diagram, this is only for demonstration purposes and the beams enter the junction at different angles in the experiment.

current (electrons from tip to sample) dominates, especially with no bias. Sharp edges on the tip are more favorable for emission, and the larger surface area of the sample acts as a better target. However, this is dependent on the pointing of the pump and the tip/sample materials. There is a saturation effect present for large biases - as the voltage is increased, electrons are accelerated more and more until there are no more electrons to accelerate. In Fig. 4.2, this happens for negative biases but not positive ones.

A photoemission experiment, analogous to OPP-THz-STM with a rapid decay constant, can be made using a THz-STM. The rectified THz current measured by the lock-in amplifier is widely agreed to be a way to measure the THz near-field at the junction [18, 46, 53]. It is believed that this occurs due to THz-induced tip work function modulation, and the local THz-induced bias lowering the amount of photons needed for multiphoton emission.

First, we do a comparison of the pump power and resulting photoemitted current, as seen in Fig. 4.3. Although the current increases monotonically with laser power, which is expected, the behavior is nonlinear. There is a threshold laser power at which the current is too small to read, and for large laser powers there appears to be a saturation of the emitted current.

Once there is sufficient photoemitted current coming from the tip, a very large amount of terahertz can be applied. Once the THz signal is found, the pump-THz delay can

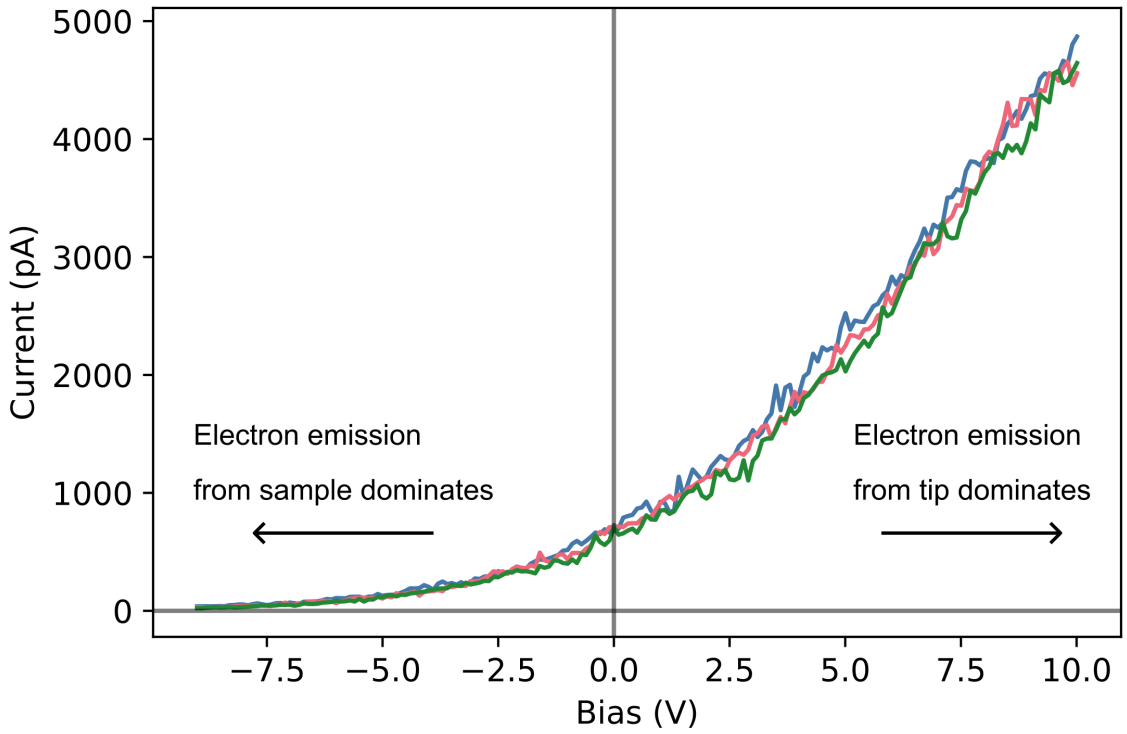

Figure 4.2: Photoemission IV of a W tip on an Au sample, at a distance of z=1500 nm using 800 nm pump light, double lens system.

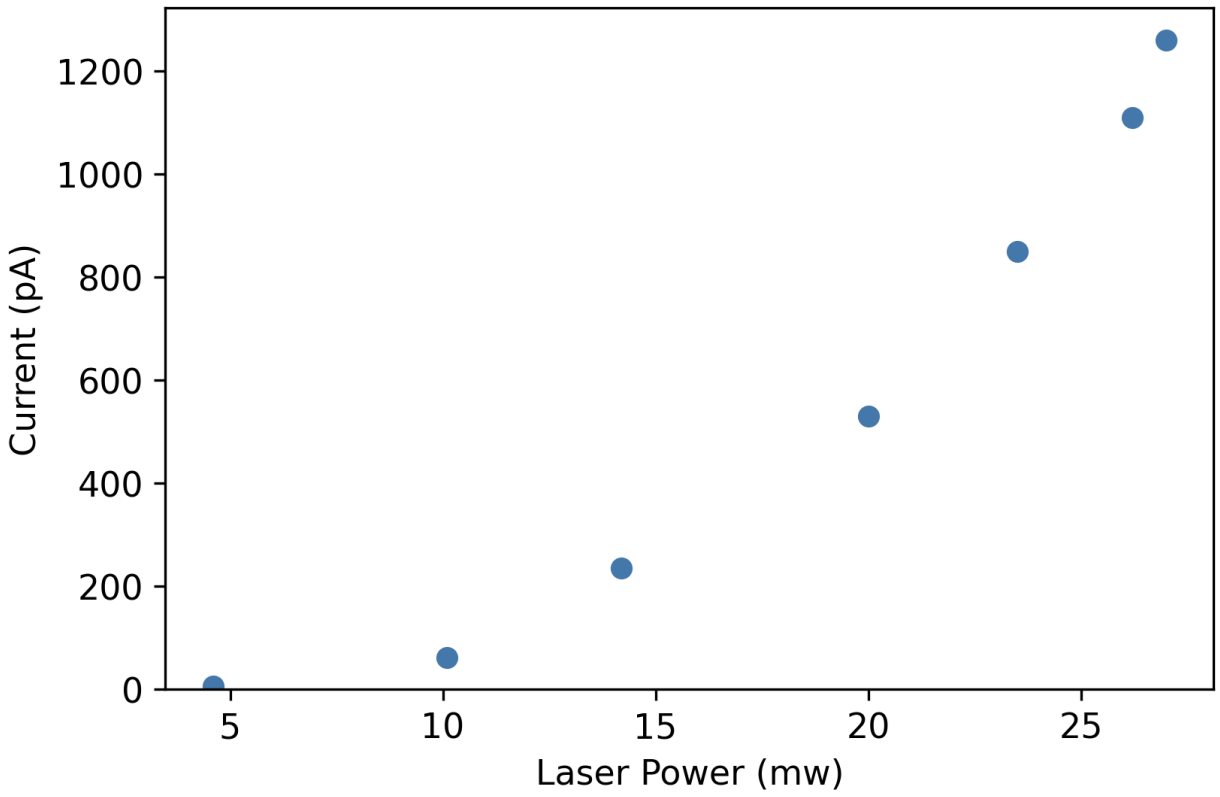

Figure 4.3: As the laser power increases, the photoemitted current increases nonlinearly. This has been taken at a bias of 10 V, using a double-lens 800 nm configuration, with a height of z=500 nm, with an Au tip and an Au sample.

be scanned in order to get the photoemission waveform.

One of the most important aspects of THz-STM is being able to verify that any signals are real and not due to RF-cross talk, background noise due to the lock-in amplifier (LIA), or some other source. There are two ways to test this out. The first is by simply blocking the THz after or before generation. The second is to introduce a THz-blocking material after THz generation to reduce the amount of THz generated while maintaining the same bias on the THz antenna. Introducing different materials can lower the maximum electric field strength and distort the signal, sometimes introducing reflections. The results for both of these tests are found combined in Fig. 4.4. The addition of three microscope slides decreases the strength of the electric field, as seen in Fig. 4.4(a), and suppresses the photoemission signal, as can be found in Fig. 4.4(b). The addition of a petri dish does not decrease the field as much, but results in a delay of 2.7-2.8 ps. An interesting observation is found in the photoemission results. Whenever the terahertz arrives before the pump beam (negative values of time), there is a periodic modulation in the background THz signal. If the THz field strength is reduced or suppressed, the photoemission signal disappears and only the background is left. This behavior is observed in Fig. 4.4(b,c) for the "3 microscope slides" and "THz Blocked" data sets, respectively. However, the background modulation only disappear when the THz generation beam does not hit the THz antenna - as seen in Fig. 4.4(c) "THz Source Blocked" dataset. This implies that the background signal is being created by some interaction between the THz antenna and the THz source beam.

Finally, the near-field is investigated. A zoom-in on the EOS and photoemission signals can be seen in Fig. 4.4(d), where all the signals have been adjusted to have their peaks at $t = 0$ ps. Although the photoemission has some distorted features, the near-field profile matches the electro-optically sampled beam. As mentioned in Chapter 3, an RLC model is typically used to model how the THz far-field gets modified when coupled to the antenna and becomes the near-field. A frequency spectrum of the original and RLC-modified signals can be found in Fig. 4.4(e). RLC model I was made to fit this data, and uses a fit of $R = 347\Omega$, $L = 160$ pH, and a fixed value of $C = 35$ fF. This model matches both the experimental photoemission spectrum and published results from literature. RLC model II uses parameters from a published THz-STM simulation from our group [54], and uses parameters of $R = 220\Omega$, $L = 75$ pH, and $C = 35$ fF.

This background signal phenomenon prompts further investigation. As seen in Fig. 3.6, there are two different flip mirrors where the THz can be blocked: the flip mirror (i) blocks the THz source before it gets converted to THz at the terahertz antenna (j). The gold flip mirror (k) can block the THz after it has been generated. For these block tests, "All Blocked" indicates that the pump, source for THz (i) and THz beams (j) are all blocked.

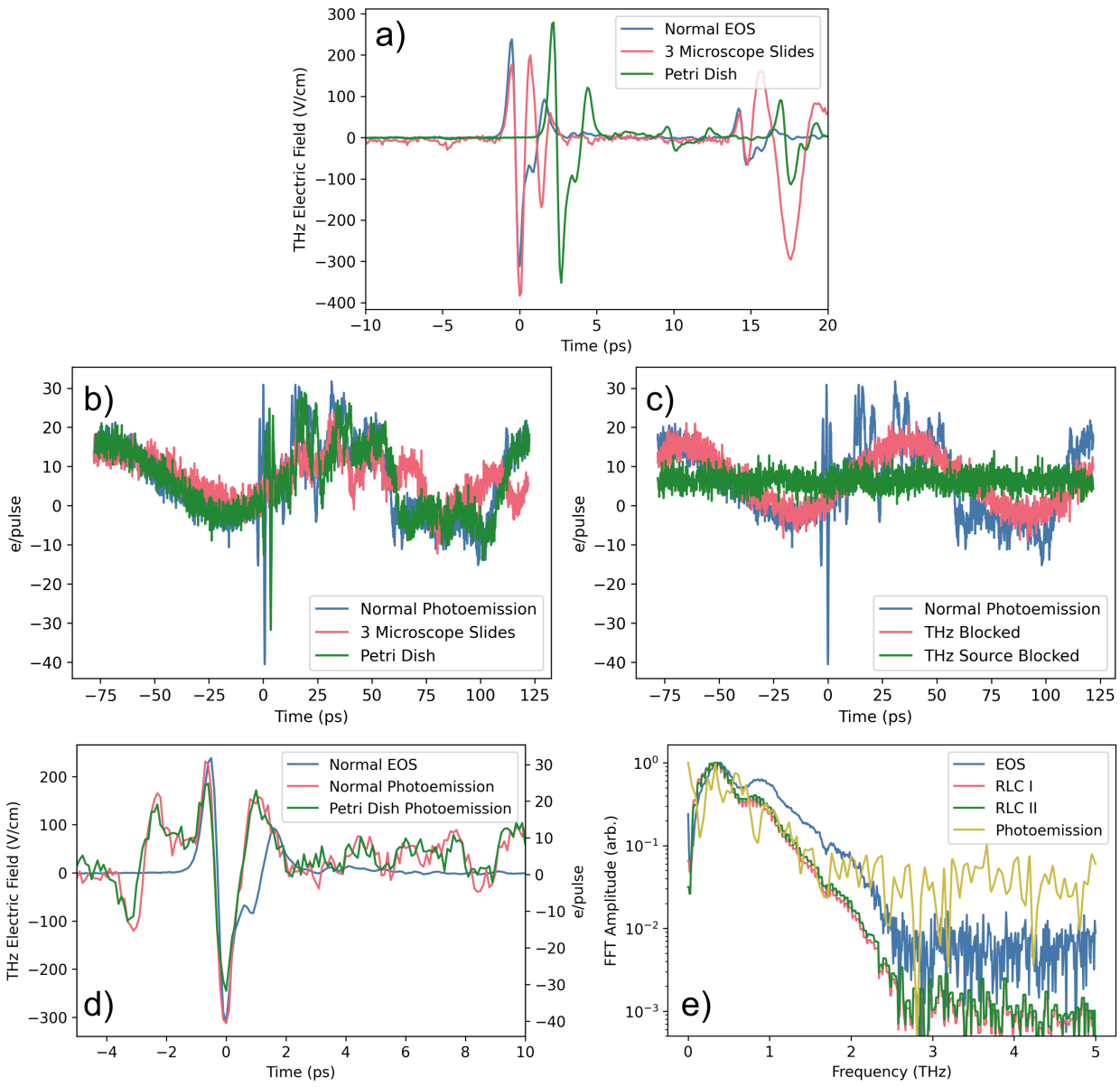

Figure 4.4: The effect of two different THz-blocking materials on THz-STM. These materials have been placed just after the THz antenna. (**a**) Electro-optic sampling of the terahertz pulse, where different materials have been placed in the path of the THz beam. The peak of the "petri dish" data is delayed by 2.7 ps compared with the other two pulses. (**b,c**) Photoemission signals taken at 10 V with 1.69 nA of current, using a 800 nm pump with a single lens, and a THz field of -395.6 V/cm. There peak of the "petri dish" data is delayed by 2.8 ps compared with the normal photoemission. In (c), the "THz Blocked" indicates that the THz has been blocked before generation, and "THz Source blocked" indicates that the THz source beam has been blocked before generation. (**d**) Comparison between the successful photoemission experiments and the EOS. (**e**) RLC circuit model applied on the EOS. Fit I was found to be $R = 347\Omega$, $L = 160$ pH, $C = 35$ fF. Fit II was made with parameters from a THz-STM publication [54], where $R = 220\Omega$, $L = 75$ pH, $C = 35$ fF.

"THz Optics Blocked" indicates that only the THz source and THz beams are blocked. "Gold Mirror Blocked" indicates that the THz beam is blocked (j). "Flip Mirror Blocked" indicates that the source for THZ has been blocked (i). Unblocked means that nothing is blocked. If any of these flip mirrors are blocking a beam, this indicates that any measured signal is due to factors other than a successful photoemission experiment.

This is explored in-depth in Fig. 4.5. While adjusting the lock-in amplifier angle, it was found that the angle that minimized the background signal (the "all blocked" data) was different than the angle that maximized the signal at the peak. As seen in Fig. 4.5(a), when the THz antenna is off, there is no signal read. For both LIA angles Fig. 4.5(b,c), whenever the source for THz is blocked, the modulations are not present. This indicates that this is caused by the interaction between the 800 nm beam for THz generation interacting with the THz antenna is causing this. As shown in Fig. 4.5(d), when the appropriate background signal has been subtracted, both LIA angles yield the same result.

Further investigation on photoemission was done, which can be found in Fig. 4.6. In order to further examine the oscillations, the entire stage was scanned, as found in Fig. 4.6(a). The oscillations at the trailing end have a period of 95 ± 5 ps. Additionally, an IE was done with a block test in order to see the effect of increasing the THz field. This was done at the peak of the curve as shown in Fig. 4.6(a). There is an increasing reading in the THz current when the flip mirror is blocked - demonstrating the importance of subtracting out any background signals. Finally, the THz dependence is shown in Fig. 4.6(c) - showing that the terahertz coupling is optimal at certain angles.

The conclusion of this chapter is that photoemission was done in order to verify that the pump optics were working and to find the location of the pump-THz intersection. This value recorded in terms of stage position, and can be used for future pump-probe experiments. Optical pump - THz-STM probe experiments have a lot of parameters that can change the signal, and by intersecting the pump and THz beams right away it can be easier to obtain a signal, especially if there is a rapid photocarrier decay in the system. Several tests were made to investigate the effects of decreasing THz fields and blocking different pulses. An RLC model of the THz antenna was made, and compared to the investigated THz near-fields found. Dependence on LIA angle, THz electric field strength, and THz polarity was investigated.

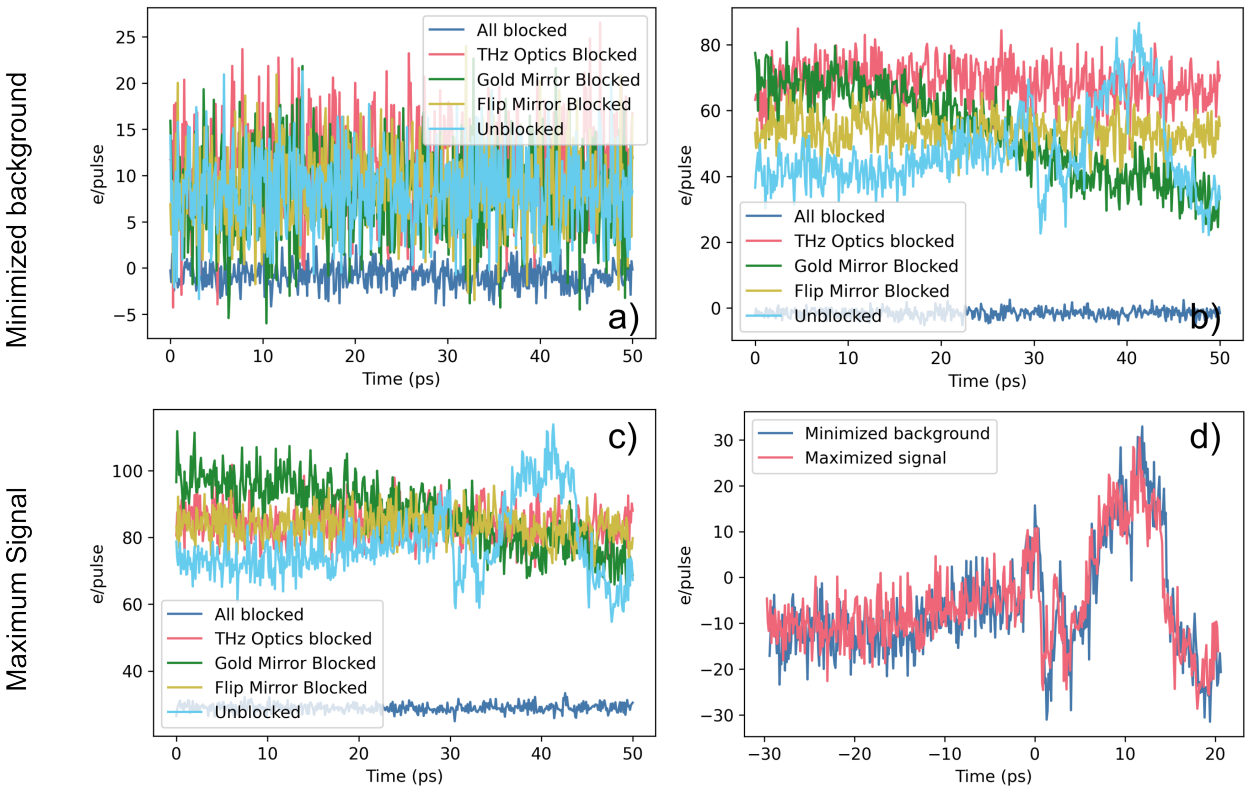

Figure 4.5: Photoemission signals at 10 V, 4 nA, 247 V/cm (if unblocked), using a W tip on an Au sample with a 800 nm pump. (a,b) show photoemission with the lock-in angle tuned to minimize the background signal. Of these, (**a**) has the THz antenna off and (**b**) has the THz antenna on. (c) has the lock-in angle tuned to maximize the signal at the peak value t = 0, and the THz antenna is on. Finally, (d) shows the comparison between both unblocked datasets, where both are normalized by their respective "flip mirror blocked" data. The data has been timeshifted to have a peak at t = 0 ps.

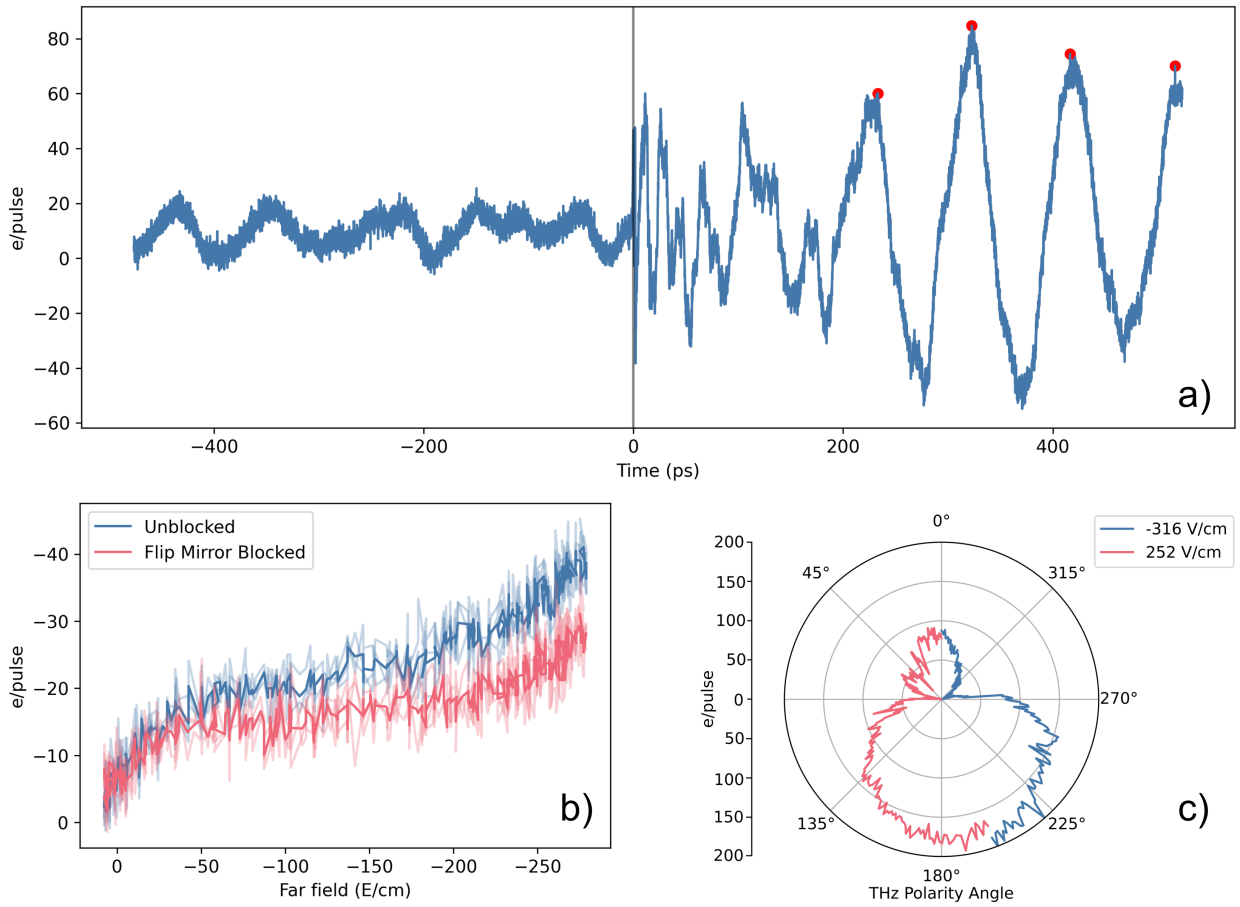

Figure 4.6: Different photoemission data with 800 nm beam. (**a**) Entire photoemission spectrum that is measurable with the range of the motorized stages. A vertical line marks the point at which the THz intersects with the pump beam, which has been timeshifted to t=0 ps. The red dots mark the maximuma of the oscillations on the latter end of the spectrum, which are separated by a distance of 95 $\pm$ 5 ps. This photoemission scan was taken at 0 V, 1.70 nA, 384 V/cm, at z=3000 nm with a single lens system and an Au tip on Au. (**b**) IE curves on the maximum of (a), showing the amount of signal measured vs when it is blocked. This was done with 40 pA, -4 V, W tip on Au, double lens system. (**c**) THz Polarity dependence at 2V, 0.5 nA, with a single-lens system an an Au tip on Au.

Chapter 5

Undoped CdS Nanowires

CdS is a material in the II-VI family of semiconductors. In its undoped state, CdS has a direct band-gap of 2.4-2.5 eV and a wurzite crystal structure [55]. The lattice constants are 4.13 Å and 6.70 Å. CdS has one surface state along the $(10\bar{1}0)$ plane [56], and another along the $(11\bar{2}0)$ plane [57].

Nanowires are of significant interest due to their change in properties in comparison to the bulk version of its material. Since surface area scaled with the square of distance, while volume scales with the cube, small objects exhibit a higher surface-to-volume ratio. Nanowires have a much larger ratio than the bulk form. Since surface area is important for photocatalytic applications, nanowires are an excellent tool for future photocatalytic applications.

This chapter pertains to the study of undoped CdS nanowires using a THz-STM. Nanowires have been studied previously in scanning tunneling microscopes [6, 58–61], including CdS nanowires [62]. Semiconductor anowires have also been studied previously using time-resolved THz spectroscopy (TRTS), including CdS nanowires [19, 22]. However, nanowires have never been studied in a THz-STM before. The TRTS studies of CdS NWs indicated a long-lived charge separation in CdS nanowires, which could be possible to image with OPP-THz-STM and set a new benchmark for THz-STM. Although those results were not achieved due to experimental and time considerations, this is the first time a nanowire is imaged and characterized using THz-STM.

CdS nanowires have been shown to grow along the c-direction (the (200) lattice plane) in hexagonal CdS as a single crystal, [63], and show an increased band gap of 2.56 eV for 26 nm-diameter nanowires. Additionally, they have hexagonal cross-sections [64, 65].

5.0.1 Sample Preparation

As described in ref [19], these nanowires were synthesized by mixing 2.5 mM $CdCl_2 \cdot 2H_2O$ and 7.48 mM NH_2CSNH_2 in 20 mL ethylenediamine, sealed in an autoclave, cooked for 36 hours at 170 C, dried overnight at 80 C, and finally crushed into powder form.

In order to be studied, the CdS nanowires had to be deposited onto a substrate. The two candidates were flame-annealed gold on mica and HOPG. These materials were selected because they were conductors, well-characterized, had relatively flat surfaces, and are easy to work with experimentally. As opposed to semiconductors which do not conduct for voltages in the bandgap, conducting surfaces can conduct at all voltages, most notably the voltages typically used in STM, which is -2.5 V to +2.5 V for the work done in this thesis. These well-characterized materials allowed us ignore substrate effects when doing spectroscopy on nanowires, especially considering that these are already well-characterized. However, it is important to note that a metal to semiconductor interface will result in a Schottky interface, and this has been shown to occur for HOPG as well [66, 67].

Although STM is able to distinguish between material types depending on the voltage selected, the main parameter reported in an STM scan is the topographical height. Therefore, the primary way to determine if a nanowires is present is by analyzing an unusual height change in the topography. A sample whose substrate has a bumpy surface can obfuscate the height change due to the nanowire. Since the sample and nanowires will have different tunneling factors, the tip height may be different between these surfaces even if all the parameters are the same. Although not on the order of a nanowire height (tens of nm), this is still important. Finally, Au on mica is easy to create using an evaporation chamber. This can be flame-annealed or annealed in UHV, as this has been shown to reconstruct the surface [68]. In this experiment, the Au was flame-annealed, after which CdS nanowires were deposited. HOPG can be exfoliated easily to create a new, atomically flat surface, and it tends to last longer in air. After assessing early results, HOPG was chosen for further experimentation as it had a flatter surface.

Nanowires were deposited onto the sample in two different ways. A solution containing CdS nanowires in powder form and methanol was prepared. We dropcasted 1.0-3.0 mg/ml of CdS nanowires onto Au and HOPG, and then quickly moved it into the STM to prevent degradation of the surface due to contaminants in the air. This tended to result in "clumping" of the nanowires into distinct, macroscopically visible yellow patches on the sample, as seen in Fig. 5.1(a). In order to find an isolated nanowire, we tried scanning near the edges of clumps. However, none of the STM images taken showed a nanowire-like increase in topography - the images were completely flat, with the exception of step edges, tip artifacts,

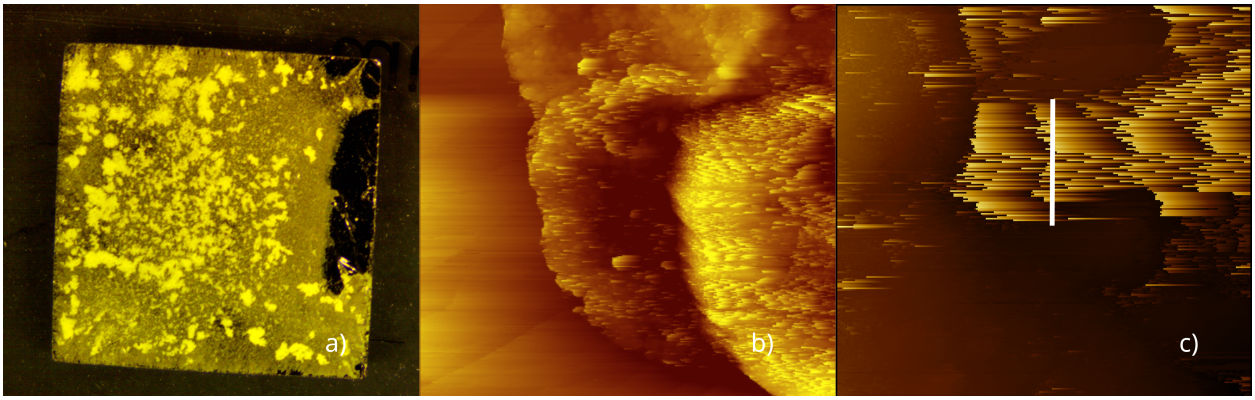

Figure 5.1: Images of dropcasted CdS on HOPG. (**a**) A microscope image of the HOPG with dropcasted CdS. The size of the HOPG is 5 x 5 mm, with a 1 mm height. (**b,c**) STM images on the edge of a clump. Scan (b) has a size of 970 x 970 nm, and scan (c) has a size of 200 x 200 nm. The line section across (c) is 29 nm, showing the length of the feature. Both STM images were acquired with a bias of -2.2 V, a setpoint of 115 pA, and a W tip.

and surface features that were not wire-shaped and too small to be a nanowire. Scanning the clumps directly also did not work, presumably because several nanowires were stacked on top of each other in those regions and the low conductivity of undoped CdS inhibited transmission and resulted in instantaneous tip crashing. One of the few results, shown in Fig. 5.1(b,c), shows the edge of the clump, and an image zoomed into it. Areas within the clump show a large amount of streaking, indicating unstable tunneling. Fig 5.1(c) shows streaking in a rectangular shape, which indicated a potential nanowire of diameter of 29 nm. However, this is likely not a nanowire, as its dimensions are much smaller than observed nanowires found later in this chapter and in Chapter 6. Due to streaking, the height of the feature is impossible to determine. Attempts to follow the feature only resulted in images that contained only streaking, and resulted in a tip crash.

After many months and variation of samples and dropcasting methods, the method was abandoned in favor of spin-casting.. This results in an even distribution of CdS nanowires, and reduced clumping. This was done for both undoped nanowires and doped nanowires (next chapter). The undoped CdS NWs were spincasted at 2000 RPM, 30s, 10uL of 1.5 mg/ml solution, imaged using SEM, then studied in STM. The images can be found in Fig. 5.2, including SEM with varying levels of zoom. The nanowires stuidied have a diameter between 45-65 nm. Since the only way to determine if a feature is a nanowire is via topography, we expect the height of the nanowires to be similar. There are large gaps on the order of several μm, making it difficult to find nanowires using an STM. Fig. 5.2(c,d) shows the nanowires in comparison to the maximum scan area of the STM, and a moderately-sized scan. There are gaps of up to 11 x 11 μm: scanning an area of that size at a fast speed of

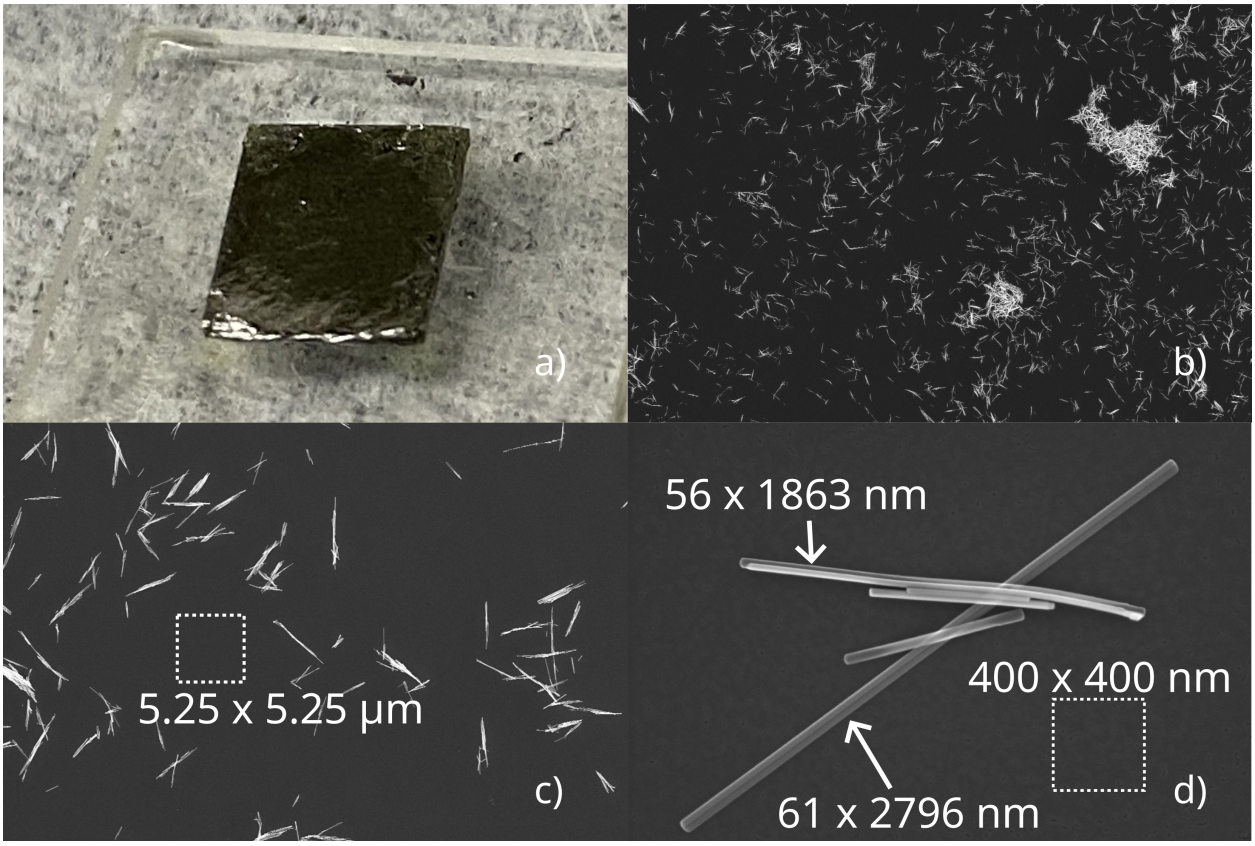

Figure 5.2: Images of undoped CdS nanowires that were deposited via spincasting. (**a**) A camera image of the HOPG with spincasted CdS. The size of the HOPG is 5 x 5 mm, with a height of 1 mm. Image attribution: Cole Thompson. (**b-d**) SEM images of spincasted CdS nanowires. The image sizes are (b) 222 μm x 150 μm, (c) 50 μm x 33 μm, (d) 2.8 μm x 1.8 μm. The dashed-line area shows (c) the maximum scan window of the UHV-STM, (d) a sample scan size, in addition to the estimated diameter and length of two nanowires. Image attribution for SEM images: John Garcia.

200 nm/s and a very low resolution of 10 nm/pixel would take 16.8 hours. In practice, it was more efficient to take successive scans in a single direction; however, this method could sometimes take up to three days to find a nanowire.

5.1 STM of NWs in Ambient

After spincasting and characterization using SEM, the nanowires were studied using the Ambient system. The standard W tips are unavailable in this setup due to them oxidizing in air. Therefore, PtIr was selected as the tip material.

As mentioned earlier, one of the biggest experimental challenges is finding the nanowires in the STM. As seen in the SEM images (Fig. 5.2), there are large gaps on the order of

several micrometers without nanowires on the substrate. Regularly-sized STM scans take a long time, and increases linearly with scan area, scan speed, and number of lines. During the searching of nanowires, having a low line count is preferable, as a larger amount of lines can be used once a nanowire is found. However, this leads to a decreased amount of nm/pixel, which means that nanowires could be obfuscated by tip artifacts or pixel noise. After detecting nanowires for the first time, it was determined that a low line count (like 64x64 or 128x128) was still sufficient for detection of nanowires due to their large height. Conversely, decreasing the line time / increasing the scan speed was not preferable. Increasing the scan speed leads to an increase of streaking, tip instability, and usually results in a tip crash. Although the Ambient system allows for a faster tip replacement, this is still inconvenient.

In order to obtain a better contrast between the nanowire and substrate properties, it is preferable to obtain a single nanowire. As seen earlier in Fig. 5.2, most of the nanowires exhibit small "clumping" and can be found in small bundles with a handful of nanowires touching them. Interestingly, a lot of the data presented seems to defy this trend, and show single nanowires. An explanation for this is due to the tip convolution seemingly bunching together groups of nanowires due to a lack of spatial resolution on tall features. This is explained in Chapter 6.

The underlying HOPG is well-characterized. The material consists of large, flat planes, which provide a very flat surface for STM. Additionally, it has atomic steps that have a height which is some integer multiple of 3 $\mathring{A}$. The atomic structure is easy to obtain in ambient, and can be found in Fig. 2.3. Therefore, it is easy to find a contrast between the underlying substrate and the nanowires based on the topography.

The first results showing cadmium sulfide nanowires are presented in Fig. 5.3 and Fig. 5.4. In both cases, the nanowires can be detected by their long shape and distinct increase in topography, indicating a tall feature. Additionally, the sides of the nanowire are parallel, indicating that they have a constant diameter, as verified by SEM. Fig. 5.3 shows an interesting topography: it is possible for this to be a singular nanowire, or multiple. The first configuration would be a nanowire 12 nm tall with a width of 287 nm. The second configuration would be a nanowire 10 nm tall with a width of 136 nm, which lies on top of a large nanowire / multiple nanowires which are 2 nm tall with a (total) width of 136 nm. Due to the incredibly small height of the possible nanowires in the second configuration, the first is more plausible. A subsequent scan of this same nanowire can be found in Fig. 5.4, where it is labeled as I. This shows two nanowires are observed to be crossing over each other, which was a case often observed via SEM. The topography shows no ambiguity and clearly indicates that this is a single nanowire.

In addition to being fairly obvious to detect via colorbar image, it is useful to take

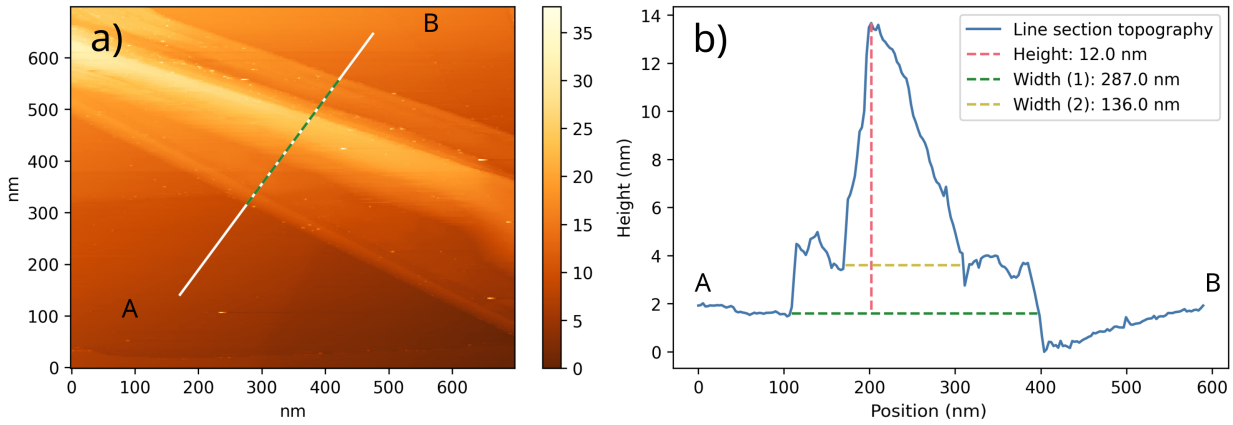

Figure 5.3: STM of an undoped CdS nanowire. (**a**) STM image of a nanowire. The image shows a white line, which represents a line section on the scan which will be analyzed in (b). Two points on the line have been labeled to better visualize the direction of the cross section. The dotted line shows the estimated width of the nanowire. (**b**) A height cross-section, found from the line in (a), as a function of position. The estimated nanowire height is 12 nm, with two calculated widths: 287 nm and 136 nm, which have been calculated at a two points 2 nm apart in height. STM parameters: 2.0 V, 440pA, 1.8 s line time, 256x256, PtIr tip, ambient

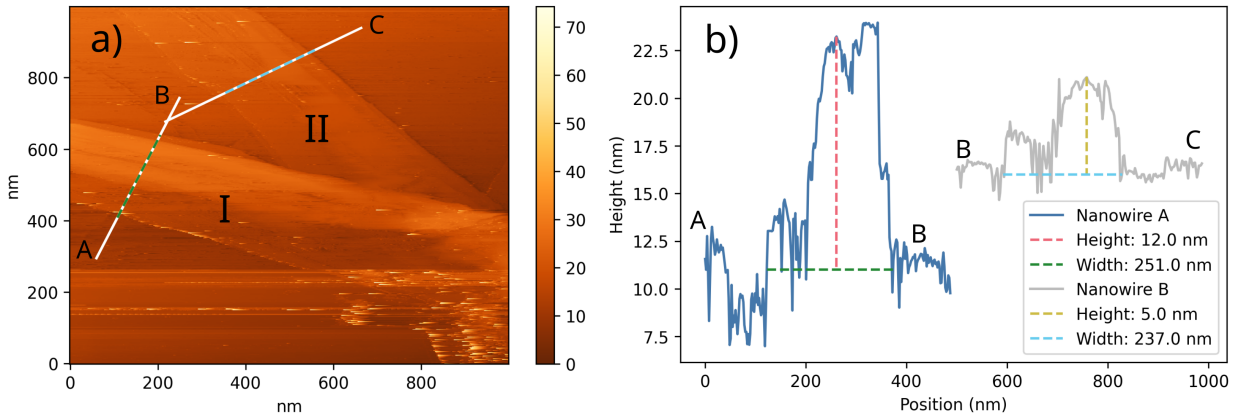

Figure 5.4: STM of two undoped CdS nanowires. (**a**) STM image of two nanowires. Nanowire I corresponds to the one imaged in Fig. 5.3. (**b**) A height cross-section, found from the line in (a), as a function of position. Nanowire A has an estimated height of 12 nm and a width of 251 nm, and nanowire B has an estimated height of 5 nm and a width of 273 nm. STM parameters: 2.0 V, 440pA, 1.8 s line time, 512x512, PtIr tip, ambient

a cross-section of the topography and analyze it, as seen in the Fig. 5.3(b) and Fig. 5.4(b). The peaks of the nanowires are simply the absolute maximum of the nanowire region, and can be easily determined. Then, the height and width of the nanowire is determined. Although the "full-width, half-max" is commonly used to estimate gaussians, the nanowires have a different shape and cannot be estimated this way. In order to account for the noise, the height and width estimations have been done manually, and correlated to the actual scan images to check if they agree with the data shown. The estimations show a very interesting result: there is a large aspect ratio between the height and the width of the nanowires.

Next, we show spectroscopy data on the nanowire presented in Fig. 5.3. This spectroscopy data is presented in Fig. 5.5. It is important to be able to compare the nanowire and substrate data directly, so Fig. 5.5(a) shows the points of spectroscopy. The CdS data has been taken on the highest lobe of the imaged nanowire, since there is some uncertainty as to whether the sides are part of the nanowire or not. From the data, an interesting pattern emerges. The IV data in Fig. 5.5(b) and Fig. 5.5(c) show very clear differences - although they have the same parameters, the IV on HOPG seems to diverge much more at negative biases. However, when both data sets are properly normalized according to Eqn. 2.28, the data sets are hard to distinguish.

In addition, it is also possible to follow the path of a nanowire using an STM. Fig. 5.6 shows a the entire length of a nanowire that was possible to scan within the range of the piezoelectric motors. It is a continuation of the nanowire found in Fig. 5.4. The image was stiched together by gathering the file metadata containing position of scan relative to the window, and then combining that into a single image. There is not a perfect overlap between successive images of the nanowire: this could be attributed to piezoelectric drift, or nanowire drift. A more in-depth study of nanowire drift could be found by measuring nanowire drift in successive SEM images. Alternatively, if there were a clearly visible surface feature near the nanowire, successive scans could reveal the drift. The topographical analysis of the nanowire can be found in Fig. 5.7.

Since Fig. 5.3 and Fig. 5.4 have a nanowire in common, and Fig. 5.6 and 5.7 show the same nanowire, there are only three unique nanowires imaged here. Topographically, they all have a height of 5-12 nm. However, there is a large amount of noise in the topography, which is on the order of 4 nm. Analysis from the SEM images is limited, but it shows typical diameters of 30-60 nm, going as low as 20 nm. As seen via SEM and in references [64, 65], it is assumed that the nanowire heights should be equal to their diameters. Therefore, these imaged nanowires are much smaller than the typical nanowire sizes predicted. Since the tip-sample height is estimated to be in the few-nm to sub-nm range, the change in material between CdS and HOPG cannot have a large effect on this height. However, the

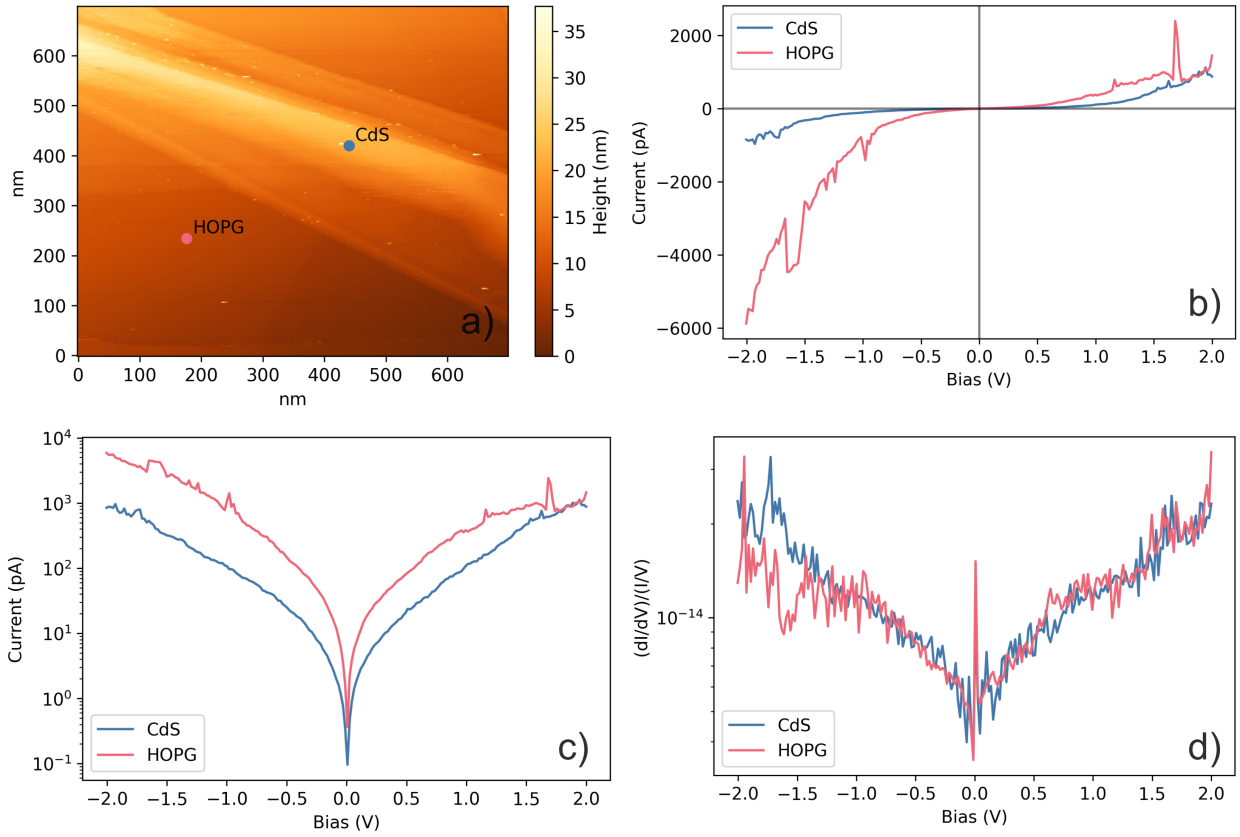

Figure 5.5: STM and Spectroscopy of an undoped CdS nanowire and HOPG substrate. (**a**) STM image of the nanowire, with points of spectroscopy labeled. (**b**) IV characteristics, (**c**) IV (log scale), (**d**) Corrected dI/dV data that has been divided by (I/V) for normalization. All data taken at +2 V, 440 pA.

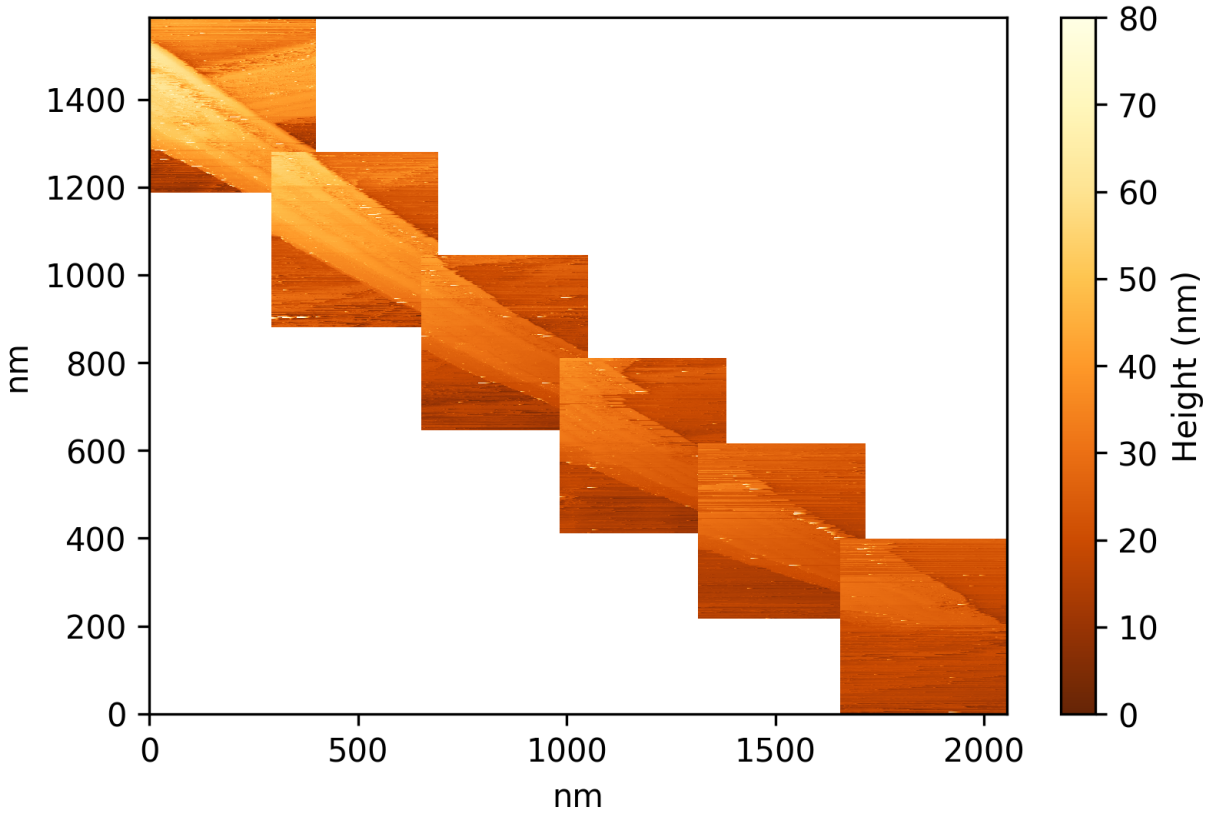

Figure 5.6: A collection of STM images following a nanowire. The images have been stitched together according to the positions they were taken. STM parameters (for all scans): 2.2 V, 440 pA, 0.9s line time, 256x256, PtIr tip, ambient

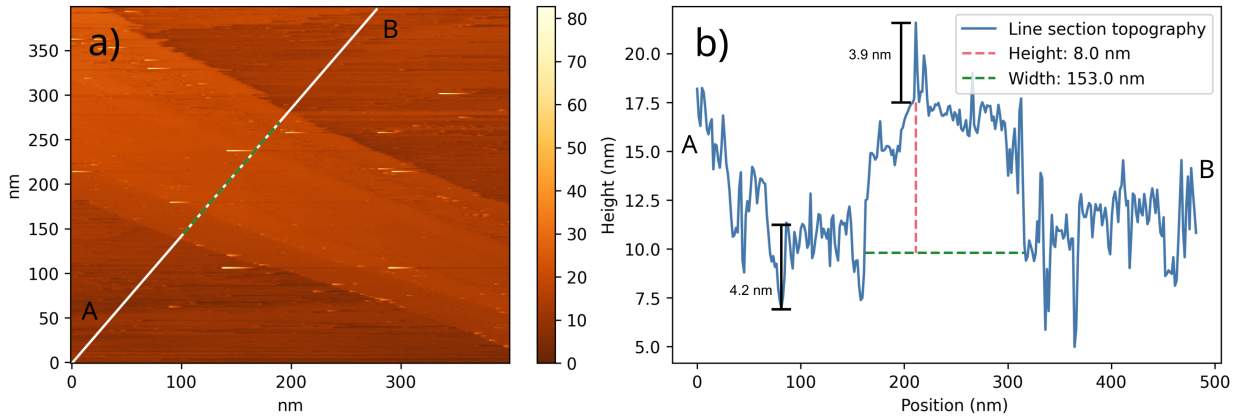

Figure 5.7: STM image of an undoped CdS nanowire, which corresponds to one of the scans from Fig. 5.6. (**a**) STM of the nanowire. (**b**) The height cross-section, found from the line in (a), as a function of position. The estimated nanowire height is 8 nm and the width is 153 nm. Due to the high noise in the image, two lines showing the height of the noise have been labeled, showing a topographic noise of around 4 nm. STM parameters: 2.2 V, 440pA, 0.9 s line time, 256x256, PtIr tip, ambient

height measurements are impacted by the noise in the topography, which limits the spatial resolution of the nanowire and substrate. It is possible that the nanowires imaged are on the lower end of the diameter range, which combined with the uncertainty in the height measurement can readily explain this discrepancy. The nanowires imaged exhibit a wire-like large aspect ratio, further reinforcing the conclusion that nanowires were imaged.

In order to attempt to further explore the nanowires in this system, the chamber was pumped down to high vacuum. However, none of these efforts were able to image a nanowire, and efforts were redirected towards the study of nanowires in UHV-THz-STM.

5.2 STM and THz-STM of NWS in UHV

After study in ambient, the sample was inserted into the UHV-THz-STM for study under ultra-high vacuum conditions. The sample was baked out overnight at 130 C. In the process of loading samples into the UHV, the samples must be temporarily rotated upside-down. Some experiments with dropcasted CdS were made to ensure that the CdS sticks to the surface, as the clumps are still visible after the sample was rotated upside down. An interesting experiment for future THz-STM studies of CdS NWs would be to image the sample after study in UHV, to see if there are any differences before and after bakeout / prolonged UHV exposure. The pressure ranged from 10^{-8} to 10^{-10} torr. W tips were used in UHV as they all have similar tip apexes and have well-documented in-situ tip conditioning parameters.

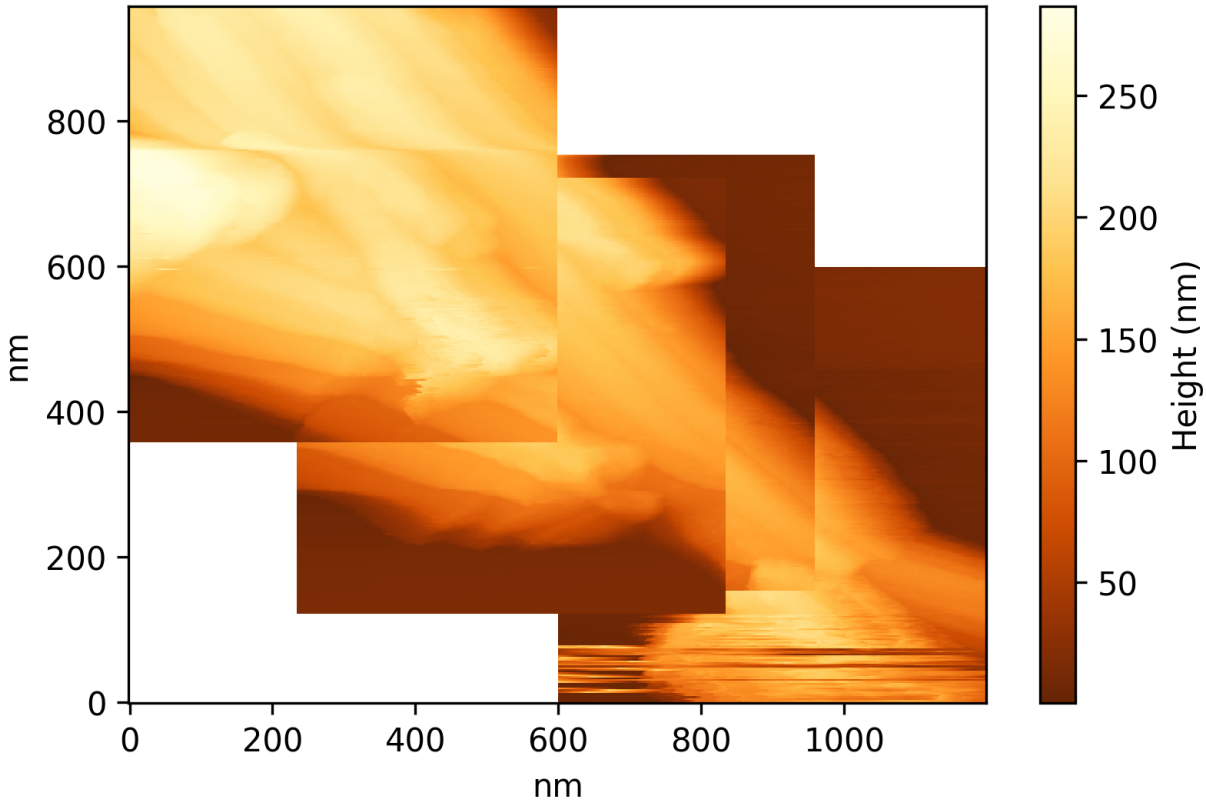

Figure 5.8: A collection of STM images following a bundle of CdS nanowires. The images have been stitched together according to the positions they were taken. STM parameters (for all scans): -2.5 V, 180 pA, 4.8 s line time, 256x256, W tip, UHV

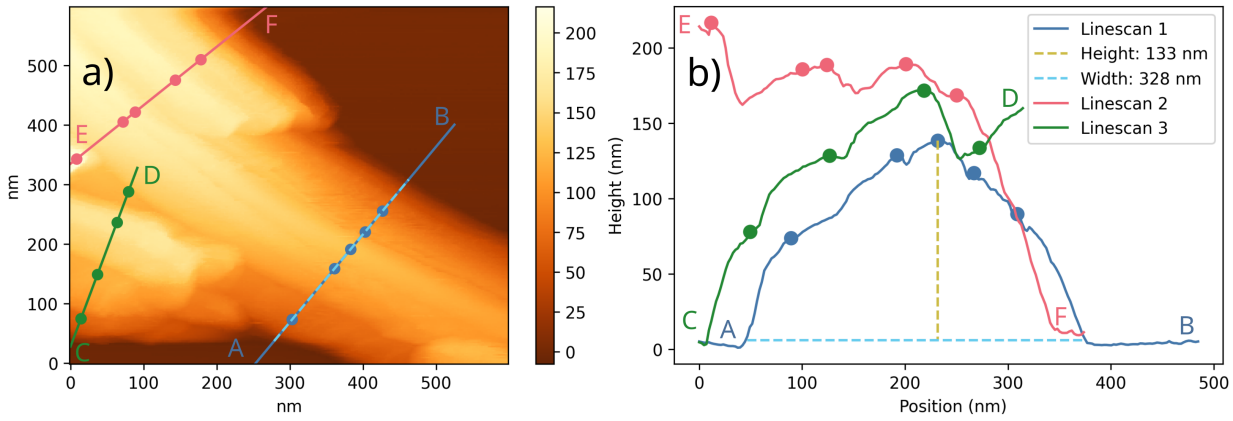

Figure 5.9: STM image of a bundle of undoped CdS nanowires, which corresponds to one of the scans from Fig. 5.8. (**a**) STM image of the nanowire. (**b**) The height cross-sections, found from the lines in (a), as a function of position. Two points on each line have been labeled to better visualize the direction of the cross section. Based on Linescan 1, the estimated nanowire bundle width is 328 nm and the height is 133 nm. Additionally, the individual peaks of within the cross-sections has been extracted, and can be seen in both graphs. STM parameters: -2.5 V V, 180 pA, 4.8 s line time, 256x256, W tip, UHV

Linescan 1 Peaks (nm)			Linescan 2 Peaks (nm)			Linescan 3 Peaks (nm)		
Height	Position	Difference	Height	Position	Difference	Height	Position	Difference
73.9	89.0		216.6	11.7		78.1	49.3	
		103.0			88.7			77.4
128.8	192.0		185.8	100.4		128.6	126.7	
		39.8			23.4			91.5
138.6	231.8		188.8	123.8		171.8	218.2	
		35.1			77.1			54.0
117.0	266.9		189.3	200.8		133.8	272.2	
		42.1			49.0			
89.9	309.1		168.5	249.9				

Table 5.1: A table containing information on the local peaks found in Fig. 5.9. The y-column shows the height of each peak, the x-column shows the horizontal length of each peak along the line, and the dx-column shows the difference between successive data points in the x-column. All values are in nm.

A nanowire is presented in Fig. 5.8, composed of multiple images. As done previously, a more in-depth analysis of the nanowire bundle using an individual scan can be found in Fig. 5.9. It is clear from the image that there are multiple nanowires imaged. In addition, there seems to be multiple-tip artifacts present, visible in the uppermost nanowire, which is parallel to the main nanowire. Disregarding multiple-tip effects, the nanowire can be analyzed by taking multiple linescans across the surface. From the first one, which runs fully across the nanowire, a height and width can be estimated. The estimated total height, 133 nm, is much larger than the SEM nanowire diameters, and the bundle width is 328 nm.

In order to try to further analyze this bundle, several local maxima along the line-sections are shown. Their height and position coordinate data is shown in Table 5.1). Keeping in mind the observed SEM radii of 30-60 nm, some analysis can be done using this data. As seen in Linescans 1 and 3, the height of the lowest peak is around 75 nm. This indicates that the lower layer of a bundle contains a nanowire approximately 75 nm tall, or two nanowires whose height adds up to 70 nm. The second-tallest peak is around 129 nm, which is an increase of 54 nm. The horizontal distance between peaks can also reveal crucial information. By taking the differences in horizontal distance between the nanowires (column 'dx' in Table 5.1) and comparing them to the SEM radii of 30-60 nm, it is clear that the different peaks across the linescans could realistically represent different nanowires on the image (assuming that in some cases a large width corresponds to two nanowires side by side).

In addition to the prior analysis, it would be incredibly useful to be able to take the bundle image and separate it into various different nanowires. To this end, we used a novel approach: an unsupervised machine learning algorithm called k-means clustering. This algorithm is designed to divide datasets into various clusters, where each cluster will represent a nanowire. The algorithm works as follows: assuming there are I data points, a total of $J(< I)$ clusters are initialized, each of which is defined by a centroid. The data points x_{i} get assigned to their nearest cluster, after which the centroid for each cluster C_{j} gets recalculated:

$$\mu_{\mathrm{j}} = \frac{1}{len(C_{\mathrm{j}})} \sum_{x \in C_{\mathrm{j}}} x, \tag{5.1}$$

where μ_{j} is the centroid for cluster C_{j}. Then, the data points are re-assigned to their nearest cluster, and the process is repeated until the algorithm converges on a solution which minimizes the residual sum of squares within each individual cluster. The elbow method can be used to determine the optimal number of clusters. This is done by calculating the residual sum of squares and comparing it to number of clusters - the natural cutoff is at at an 'elbow' in the data. For this analysis, the number of clusters was determined to be 6, which

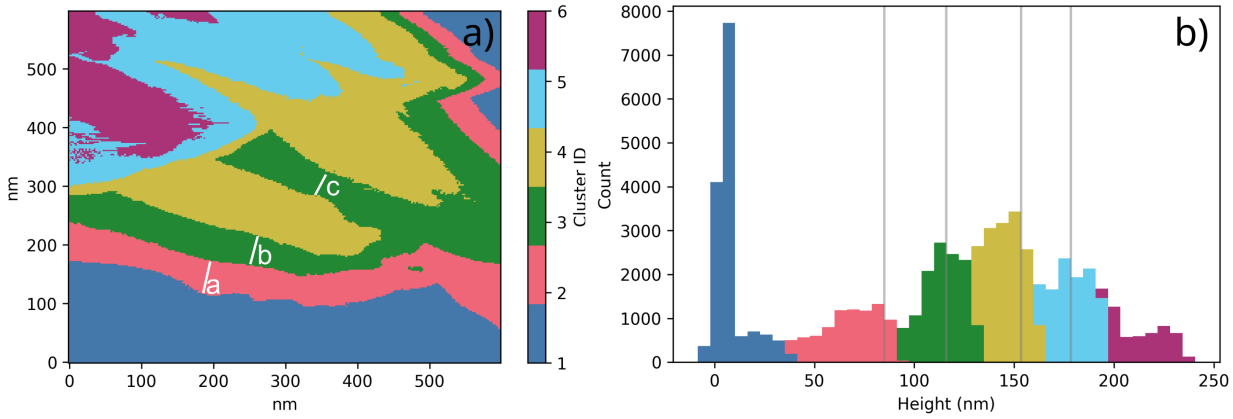

Figure 5.10: A colormap of the clustered form of Fig. 5.9. (**a**) A colormap where the nanowire bundle has been separated into different clusters, each of which has a different color. Three lines have been drawn in order to determine the distance between different clusters. Line a has a length of 56 nm, line b has a length of 52 nm, and line c is 43 nm. (**b**) The height values for each cluster. Vertical lines show the peaks of the clusters, indicating their maximum height. The height difference between clusters 2-3 is 31 ± 6 nm, clusters 3-4 is 37 ± 6 nm, and clusters 4-5 is 25 ± 6 nm.

is confirmed with visual intuition. The results of splitting this nanowire bundle into different clusters can be found in Fig. 5.10. As shown by the lines, the horizontal spacing between clusters is 43-56 nm, which matches observed SEM NW radii and supports the theory that each cluster is a nanowire. Furthermore, by analyzing the height of each cluster, this conclusion is reinforced. The vertical height differences between clusters, found by taking their maxima, is $25 - 37 \pm 6$ nm. Although this does not perfectly match the horizontal spacing between clusters, it is also within the range of observed SEM radii. Finally, this image can be compared visually to Fig. 5.11(a), which shows the unprocessed image.

Fig. 5.11 provides spectroscopy data on various parts of the nanowire bundle shown in Fig. 5.10. In order to show where on the nanowire the data has been taken, Fig. 5.11(a) shows the location of each spectroscopy. First, the IV data is shown in Fig. 5.11(b). Different setpoints where chosen to show the effect of different setpoints on the data. Additionally, Fig. 5.11(c) shows the IV data in a logarithmic form. Finally, Fig. 5.11(d) shows the dI/dV data which has been normalized using Eqn. 2.28. Interestingly, even though there are many differences in the IV spectroscopy, the results are all similar, with an approximately constant DOS (with a singularity at V=0). All of the various spectroscopies on CdS NWs showed this behavior.

While scanning nanowires in UHV, an interesting discovery was found. The nanowires seem to have a bias dependence, as illustrated in Fig. 5.12. Three successive scans are taken

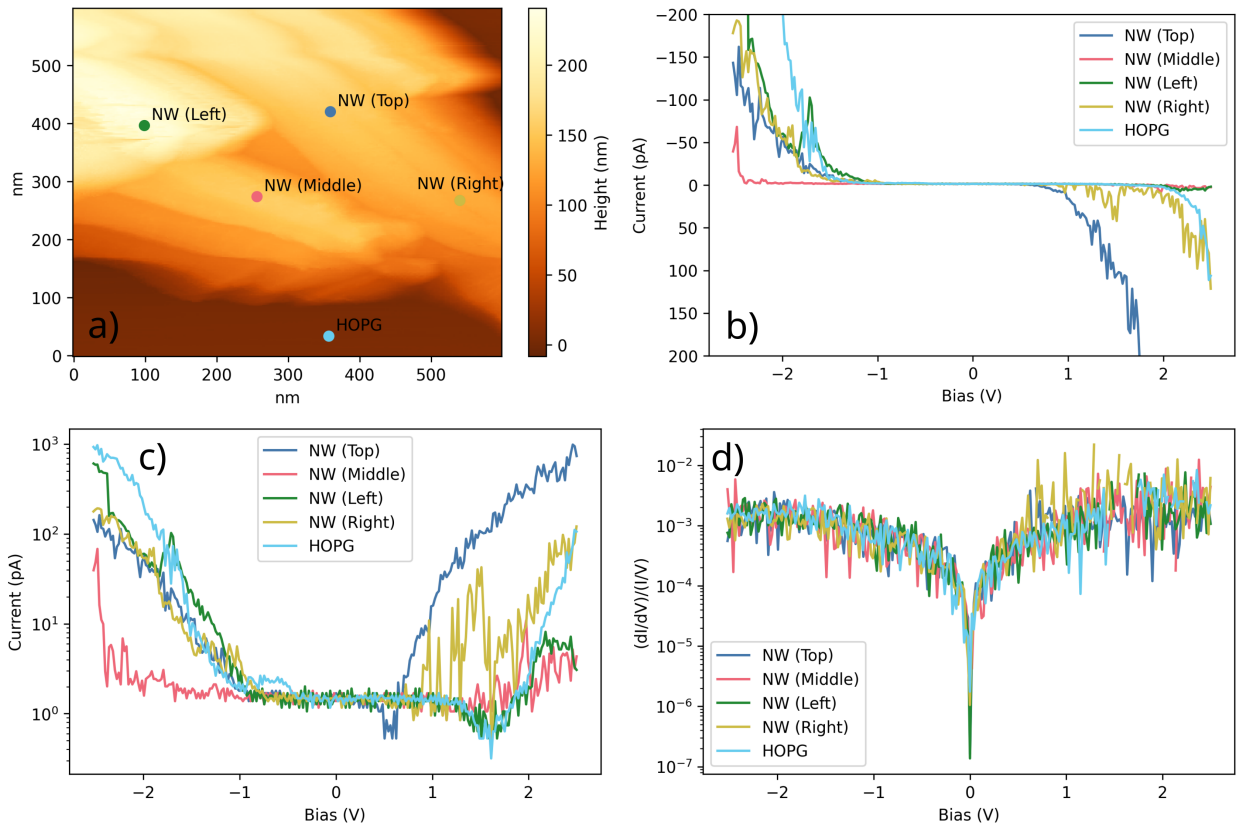

Figure 5.11: STM and Spectroscopy on a nanowire bundle, which is the same one analyzed in Fig. 5.10. (**a**) STM image with the points of spectroscopy labeled on the image. STM parameters: V = -2.5 V, 240 pA, 256x256, 3.1 s line time, UHV. (**b**) IV data, which is trimmed for full visibility. (**c**) IV data (logarithmic scale). (**d**) Corrected dI/dV data, which has been divided by (I/V) for normalization. STM parameters: -2.5 V for all. Setpoints: 200 pA for Top, 100 for Middle, 200 for Left, 300 for Right, 150 for HOPG.

on the exact same spot, with different biases. The first scan, Fig. 5.12(a) shows a nanowire. The second scan Fig. 5.12(b), which uses an inverted polarity for the bias, does not show this feature at all. The region where the nanowire *should* be matches the height of the underlying HOPG - indicating that the tip was somehow blind to the underlying feature. Even more interestingly, the nanowire was found again by scanning the area again with the original parameters in Fig. 5.12(c). This indicates a bias-dependence of the nanowire scanning, or that the second bias used (+2.5 V) lies within the bandgap of CdS and does not have any LDOS states at that level.

This phenomenon may also be explained via tip-induced band bending (TIBB). The contact potential $\Delta\phi = \phi_t - \phi_s - eV$ depends on the tip vacuum barrier ϕ_t, the sample barrier ϕ_s, and bias on the sample eV [69]. CdS has surface states that range from 0.05 eV to 1.5 eV below the conduction band, while the valence band is 2.4 eV below the conduction band [70]. Therefore, when a negative bias is applied, the surface states and conduction are lowered such that electrons can tunnel from the tip to sample. However, when a positive bias is applied, the surface states and conduction band are moved upward, effectively blocking this conduction pathway. Electrons cannot tunnel from the tip into the occupied valence band in the CdS. However, this behavior should also be visible in any IV curves, showing reduced tunneling current at a bias of +2.5 V. Taking a look at Fig. 5.11, this behavior is not present. Another possible explanation is that the nanowire is being dragged around by the STM tip, however, it is highly unlikely to have returned to the same position and orientation as before. As it is impossible to make a determination from this limited data set, further investigation is warranted.

Curiously, biases of 2.0-2.2 V were effective in imaging CdS NWs during scans under ambient conditions (see Fig. 5.3 and Fig. 5.7). Although an important parameter (tip material) varied between these scans, this should not an important factor due to their similarly flat LDOS. Therefore, it can be concluded that this is due to adsorbents on the nanowire surface, an effect which is mitigated in UHV. An increase in extrinsic surface states or fermi level pinning could lead to this effect.

Additionally, THz-STM data was taken on the HOPG in order to better characterize the differences between HOPG and CdS for future data. Fig. 5.13(a) shows that the signal is due to THz and not due to some sort of cross-talk between the voltage on the THz antenna and the signal wires. Fig. 5.13(b) shows the dependence on setpoint for THz scans. Due to the time limitations, no THz-STM results on undoped CdS NWs were obtained. Since different biases and setpoints were used, it is likely that the limiting factor was the tip not having a geometry ideal for coupling to THz beams. The first THz-STM publication showed rectifications in the hundred-e range [1] on HOPG, while we have obtained a value under 50

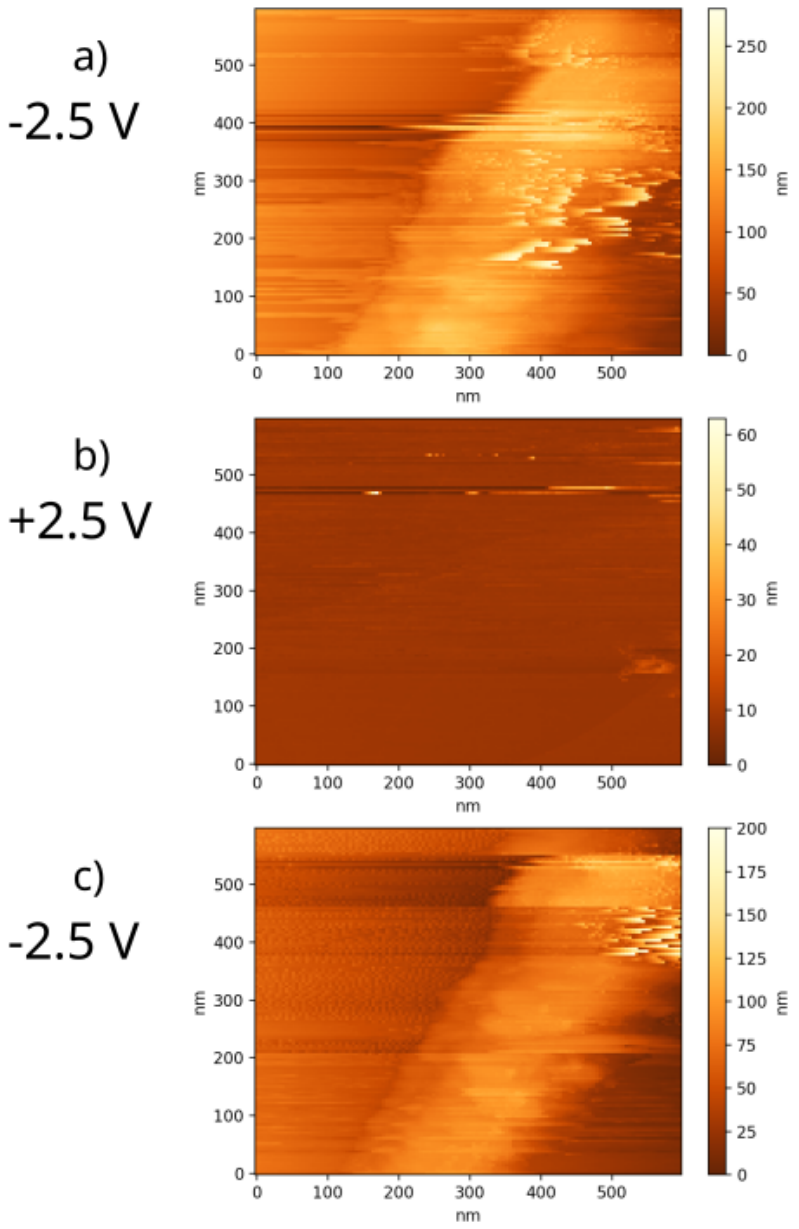

Figure 5.12: Several STM images that were taken on the same area where a nanowire is located. The scans were sequentially taken in the order (a-c), but with different biases. The STM scans were taken at biases of (**a**) -2.5 V, (**b**) +2.5 V, (**c**) -2.5 V. Although all scans are over the same area, the second scan does not show a nanowire. This shows the bias dependence of the nanowire topography. Other STM parameters: 240 pA, 256x256, 4.0 s line time, UHV.

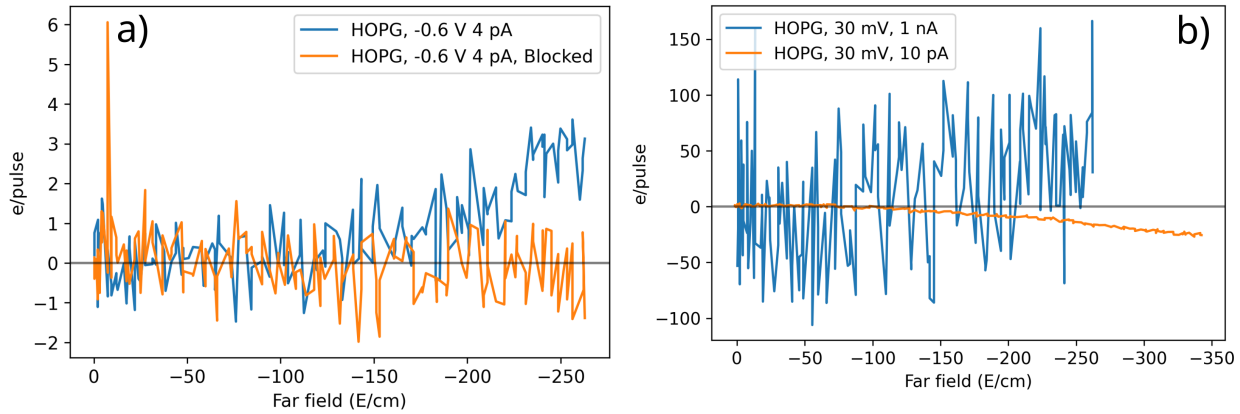

Figure 5.13: IE data on HOPG. (**a**) IE data using parameters experimentally found to be good for coupling THz onto HOPG. By increasing the magnitude of the terahertz strength, the signal increases (after some cutoff point). Additionally, a scan with the THz line blocked is shown, which is found not to have a signal. (**b**) IE data with varying setpoints. The high-setpoint data does not provide any THz signal while the low-setpoint one does.

e/pulse with similar parameters. Nonetheless, the ability of THz-STM to couple to HOPG has been proven.

Chapter 6

Mn-Doped CdS Nanowires

6.1 Sample Preparation

Since CdS nanowires are semiconductors, they can be doped to increase their electrical conductivity. Due to the challenges in obtaining a THz-STM signal on undoped CdS nanowires, a new sample of Mn-doped CdS nanowires was made. The doping was selected to be 5% Manganese, which should lead to an increased electrical conductivity, thereby making it easier to obtain a THz-STM signal on the material. Additionally, Mn-doping of CdS has been shown to act as an acceptor leading to a p-type semiconductor, increase the photovoltage for optical excitations, and add mid-band gap states via the d-orbital of Mn [71–73]. This should remove the bias-dependent scanning property that was shown for undoped CdS nanowires in Fig. 5.12. Additionally, an increase in photovoltage should lead to an increased OPP-THz-STM signal.

These nanowires were also spin-casted onto HOPG. This was done using a 1 mg/ml solution of Mn-CdS NWs and methanol, and spincasted at 2000 RPM for 60 s with 20 μL of solution. This results in an even distribution of CdS nanowires, as found previously with the undoped ones. Two SEM images can be found in Fig. 6.1. Although the nanowire morphology looks slightly different, the nanowire diameters and lengths are the same as those found in the undoped nanowires in Fig. 5.2. As with the undoped SEM images, the nanowires tend to group up in small bundles with large μm-sized gaps between nanowires. This means that the experimental time to find a nanowire is still approximately 1-3 days.

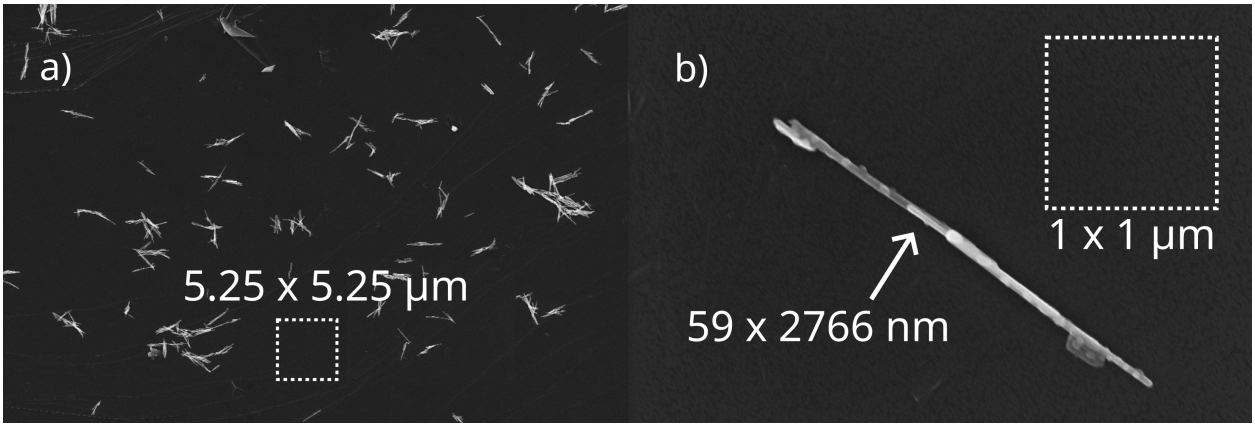

Figure 6.1: Images of dropcasted Mn-CdS on HOPG, acquired via SEM.(**a**) SEM image with a size of 37.4 x 55.6 μm, which shows the maximum scan window of the STM. (**b**) SEM image with a size of 3700nm x 2490 nm, where the pictured nanowire has a diameter of 59 nm and a length of 2766 nm. The image also shows the area of a large scan, which corresponds to the size of some of the scans presented in this chapter. Image attribution: John Garcia

6.2 Tip Radius Determination and Deconvolution

Chronologically, the undoped nanowire experiments were done before the doped nanowire experiments. Work on the undoped CdS NWs showed a discrepancy in nanowire dimensions - the STM images showed much wider nanowires than what was seen in SEM. It was theorized that this is due to the convolution between the tip and sample. Therefore, a more in-depth investigation was performed to determine the magnitude of this effect. All the results were taken with a single tip, which received large amounts of field emission and electron bombardment in order to sharpen it. After all the results were collected, the tip was imaged using SEM. This could only be done at the end of data collection, as the process of inserting the tip into SEM would expose it to air. This would lead to some oxidation of the tip, making it ineligible for further use in STM.

In this section, the dimensions extracted by SEM will be taken as the "true" values and the dimensions extracted from STM will be taken as modified dimensions. This apparent broadening can be described entirely by the convolution between the tip and nanowire(s). As described in Chapter 2, the finite size of an STM tip can interact with the sample at multiple points, leading to a sort of convolution. Tall features, such as a nanowire, are particularly susceptible to this effect [74, 75]. Additionally, the finite size of an STM tip has also been shown to affect the resolution of a THz-STM [47].

There are two primary ways to estimate the size of an STM tip: blind tip reconstruction, and imaging it with SEM. Unfortunately, the former is not possible due to the lack of

good tip-characterizing features on the surface (a good feature could be holes on the order of multiple tens of nanometers). Therefore, the tip radius must be extracted from the SEM images only. The treated tip used for STM can be found in Fig. 6.2. Additionally, since the tip was subjected to field emission and electron bombardment, a fresh STM tip resembling the original STM tip was also imaged, which can be found in Fig. 6.3. Unfortunately, prior to imaging via SEM, both tips were crashed. However, the apex of the tip remains intact as seen via SEM imaging, so the estimations derived are assumed to be accurate.

In the case of the treated STM tip, as seen in Fig. 6.2, it is difficult to obtain the exact profile of the tip. Since the tip was accidentally bent into itself, it is hard to determine which part is the tip apex. This could be approximated as two regions, a major circle with diameter 1170 nm and a minor circle with diameter 340 nm. However, while the major circle is clearly part of the tip apex, it is unknown if the minor circle formed part of the apex. Since only the bottom of the tip can be in contact with the sample, no additional information can be gained by combining these two circles in one figure. Fortunately, obtaining the radius of the fresh tip was easy, and the profile of the tip could easily be extracted by obtaining the contrast between the tip and the background, as seen in Fig. 6.3.

Next, we perform tip-sample convolution simulations using realistic tip parameters, which can be found in Fig. 6.4. A nanowire diameter of 60 nm was used as this matches the SEM images shown earlier. Fig. 6.4(a,b) shows simulation results using the major circle on the treated tip, Fig. 6.4(c) shows simulation results with the minor circle, and Fig. 6.4(d) shows simulation results with the profile extracted from the fresh tip. Overall, the simulations show broadening from 60 nm to 270-500 nm in the case of a single nanowire. This is consistent with previous results in Chapter 5 showing broadened nanowires. In the case of multiple nanowires that are directly adjacent to each other, as seen in Fig. 6.4(b), each excess nanowire broadens the observed width by its diameter. As expected, there are peaks observed in the convoluted data whose peak separation is the same as the nanowire diameter. In the case of nanowires that are not directly adjacent, the peak separation will be the diameter plus the separation between nanowires.

A mathematical model for this broadening can be constructed. To illustrate this, a diagram is presented in Fig. 6.5(a). The tip (left circle) and the nanowire (right circle) are represented as two circles laying flat on the surface, which have been pushed together until they have just started to touch. As the tip moves right, it will start to rise, meaning that the distance x represents the point when the nanowire image first appears. Therefore, x represents the imaged nanowire radius. For this example to be valid for real tips, only the bottom part of the tip circle can be in contact. Therefore, the tip radius R must be double the nanowire radius r or more ($R \geq 2r$). From this example, multiple properties can be

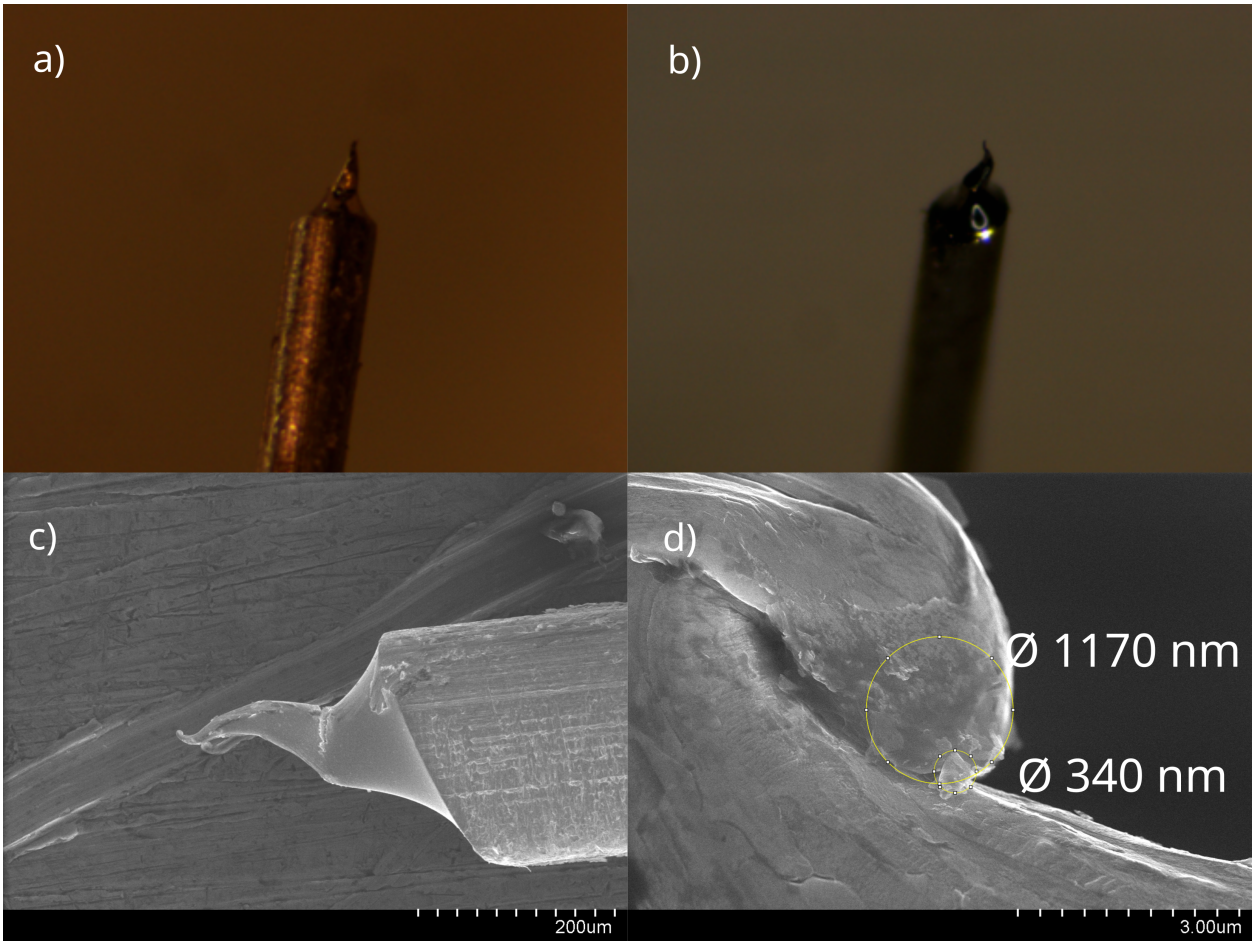

Figure 6.2: Images of a treated STM tip. (**a,b**) Optical microscope images of the tip before and after crashing. (**c,d**) SEM images of the crashed STM tip with different levels of zoom. The tip has been bent into itself, so approximating the profile is slightly difficult. There are two different features that could constitute the apex of the tip, which are indicated by two circles superimposed on the end of the tip. The large circular region has a diameter of 1170 nm and the smaller region has a diameter of 340 nm. It is unknown if the smaller region was attached to the apex of not, so simulations with both diameters will be presented. Image attribution for SEM images: Makoto Schreiber and Kai Cui.

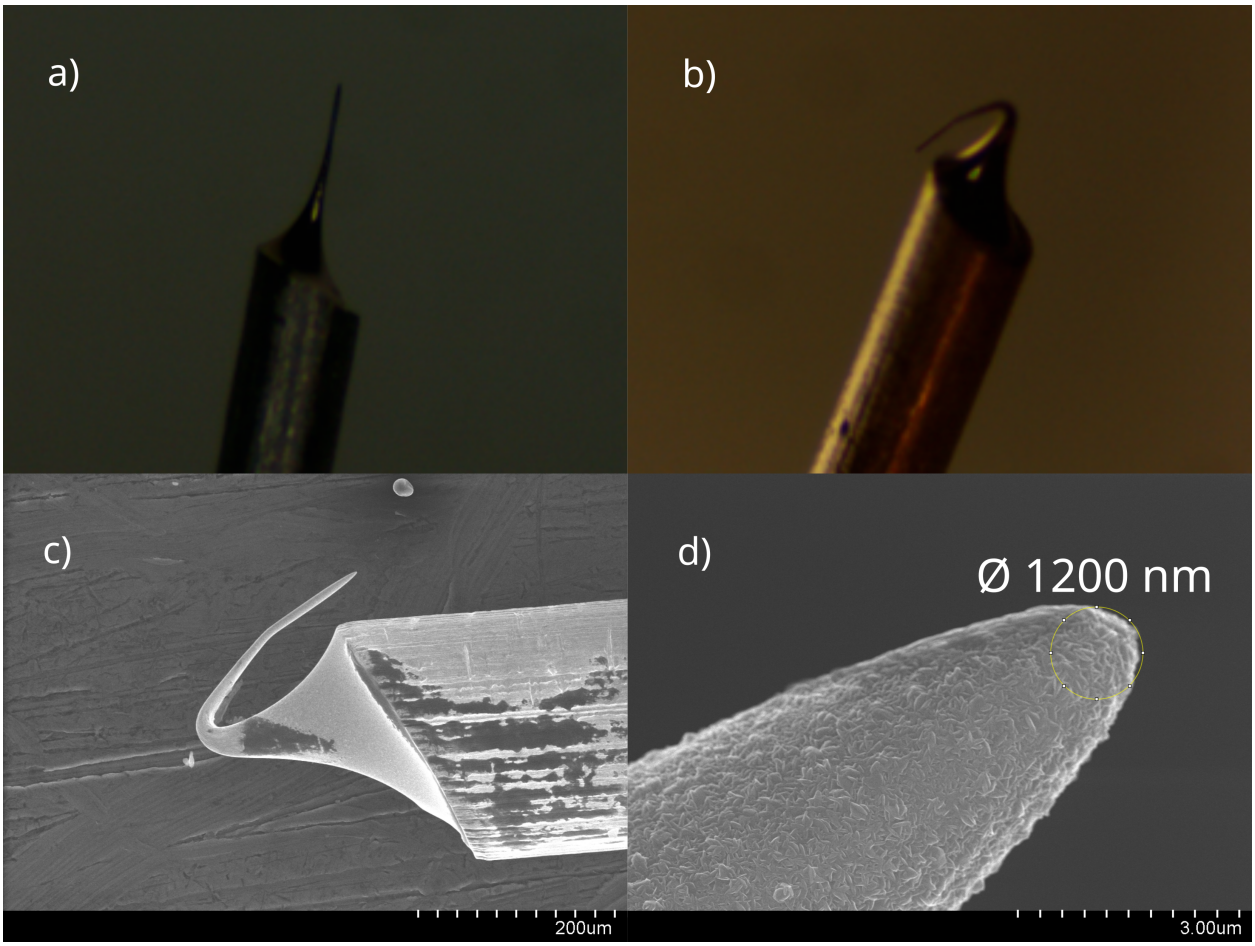

Figure 6.3: Images of a fresh STM tip. (**a,b**) Optical microscope images of the tip before and after crashing, respectively. (**c,d**) SEM images of the crashed STM tip with different levels of zoom. The tip has an approximately circular apex, indicated by a circle superimposed on the end of the tip, with a diameter of 1200 nm. Due to the contrast, it is possible to extract the profile of this image easily. Image attribution for SEM images: Makoto Schreiber and Kai Cui.

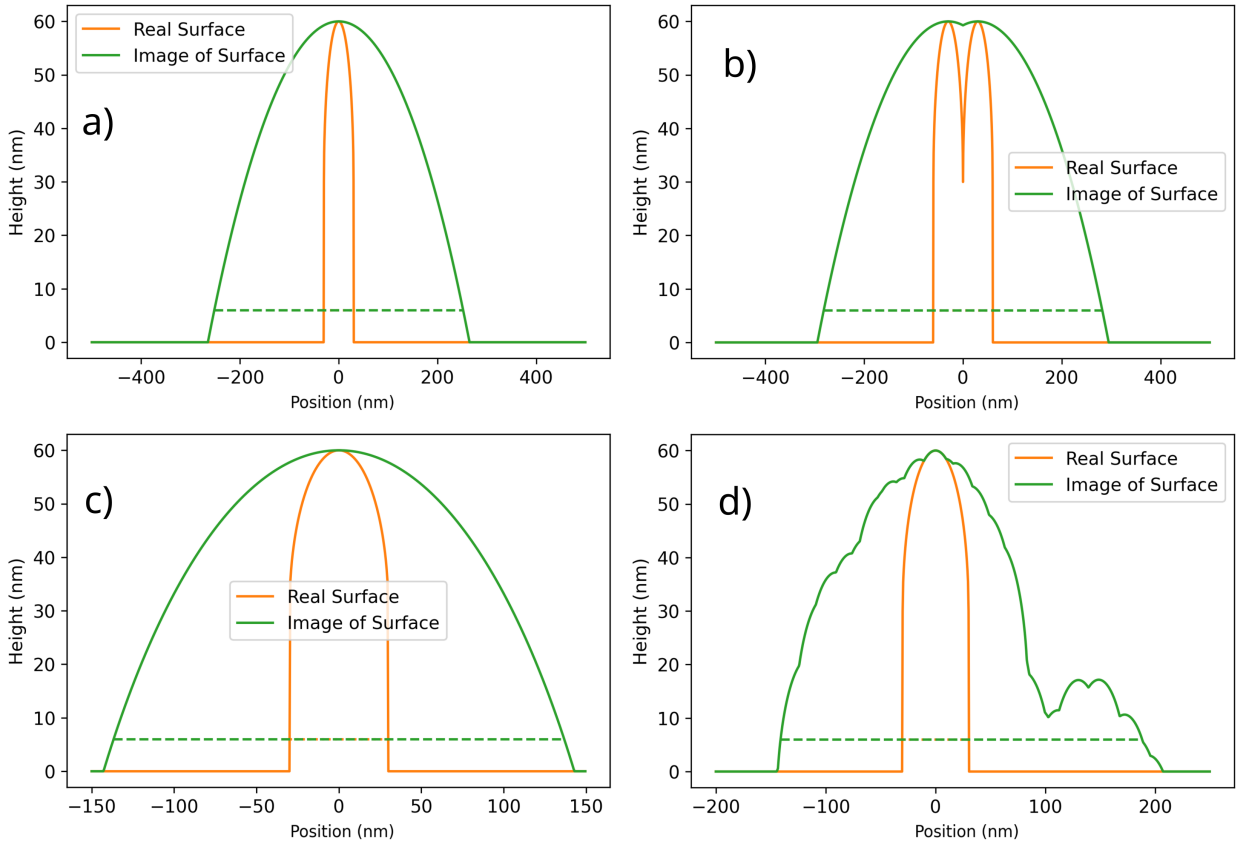

Figure 6.4: Simulation of tip-sample convolution with a nanowire of diameter 60 nm. Note that the images are have seperate height and length scales, so the imaged may appear distorted. (**a**) A simulation with a tip of diameter 1170 nm, which matches the major diameter on the treated tip. The imaged nanowire has a diameter of 504 nm. (**b**) Simulation with a tip of diameter 1170 nm, and features two nanowires that are side-by-side. The imaged nanowire has a diameter of 564 nm. As expected, this is exactly 60 nm more than (a) and the spacing between the two peaks is 60 nm. (**c**) Simulation with a tip diameter of 340 nm, which matches the minor diameter on the treated tip. The imaged nanowire has a diameter of 273 nm. (**d**) Simulation with a tip profile extracted via image analysis from the fresh tip. The imaged nanowire has a diameter of 329 nm.

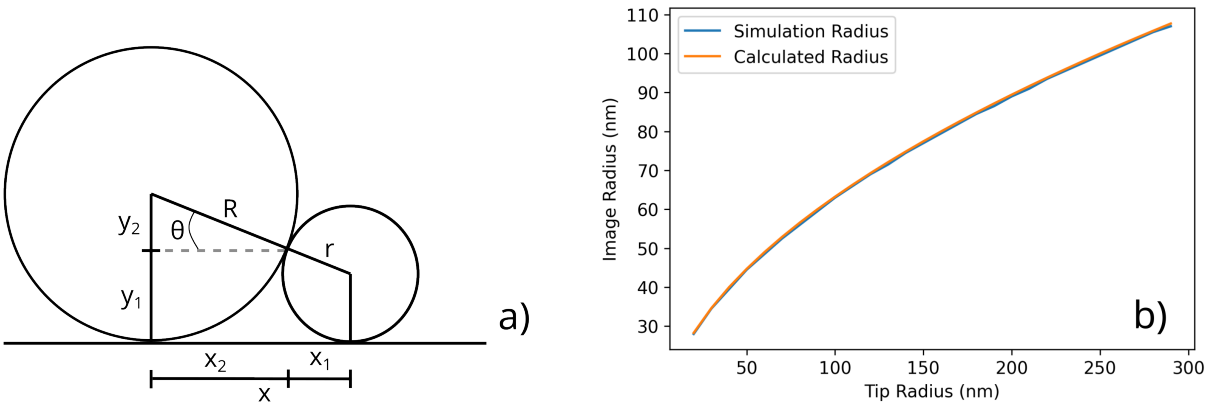

Figure 6.5: Two images that show the convolution effect of the tip and sample for a circular tip - circular nanowire configuration. (**a**) A diagram of the setup, with distances that can be described in Eqn. 6.1 and Eqn. 6.3. (**b**) Simulation data with a nanowire of $r = 10$ nm and varying tip radius. The simulation radius has been extracted by analyzing the points on the image that are not on the substrate. The calculated radius comes from the Eqn. 6.3.

extracted using simple geometry:

$$x = x_1 + x_2, x_1 = r\cos(\theta), x_2 = R\cos(\theta) \tag{6.1}$$

$$y = y_1 + y_2, y_1 = r + r\sin(\theta), y_2 = R\sin(\theta) \tag{6.2}$$

From this, one can arrive at the solution for the imaged nanowire radius:

$$x = (r + R)\cos\left(\sin^{-1}(\frac{R - r}{R + r})\right) \tag{6.3}$$

Multiple simulations with varying tip sizes were performed, and the results were compared to this formula can be found in Fig. 6.5(b), which shows agreement. Therefore, these principles can be applied to nanowire images from STM in order to make conclusions about the data. The actual nanowire radius r can be extracted from the height of the imaged nanowire; the imaged nanowire radius x can be found via the width of the imaged nanowires; and the tip radius R can be found via SEM.

As described in Chapter 2, it is also possible to deconvolute an image if the tip parameters are known. This corresponds to mathematical erosion [36]. This deconvolution has been implemented into the simulation, and its results can be seen in Fig. 6.6. The deconvolution process is the inverse of the convolution process, or mathematical dilation. Simulation-wise, the bottom-most point of the tip travels across the image, and any parts of the image that intersect with the tip are carved out. This can be observed in Fig. 6.6(a), where the simulation has been stopped to show the erosion process. The left of the tip is

eroding the surface away as it travels across the imaged surface. The hole on the left side of the picture shows off another logical conclusion: if the imaged hole is narrower than the tip, then the tip cannot possibly fit inside the hole to image the bottom - therefore, the real surface must have a hole that is large enough to accommodate the tip.

Although this technique is the best technique to reconstruct an original surface, it is not perfect. This can be seen in Fig. 6.6(b), which shows the convolution of two tall rectangles, and then the subsequent result from deconvolution. A great deal of information is lost, particularly in the center of the structures where the tip cannot possibly reach the bottom. Therefore, it is important to emphasize that deconvolution via erosion is the best mathematical way to reconstruct an image but it is impossible to reconstruct an image perfectly.

When deconvoluting a circular nanowire and circular tip, as shown in Fig. 6.6(c), the reconstruction cannot recover the correct apparent width of the nanowire. The onset of the imaged nanowire - specifically, the first point at which the image height is nonzero - is the same for both the convoluted and deconvoluted images. However, the deconvolution still has a noticeable and distinct effect on the image. To account for this, the height of the nanowire can be measured at some higher point, such as a height of 5 nm. Fig. 6.6(d) shows a graph with the estimated nanowire widths of convoluted nanowires, and the nanowire widths of the reconstructed nanowires.

When analyzing nanowire images, both the convoluted and deconvoluted images will be used for the analysis.

6.3 CdS NWs in UHV and RT

For the first section of results, we present results that were taken in UHV, at room temperature, and using the W tip imaged earlier (see Fig. 6.2).

As was done previously, a collection of STM images following the nanowire is presented in Fig. 6.7. Once again, the nanowire features are very distinguishable from the underlying substrate and their aspect ratio is very large, indicating a wire-like structure. An analysis of the topography was done in Fig. 6.8, this time with more analysis done using the results found in Chapter 5. Additionally, since each STM scan actually produces two images, due to the tip scanning back and forth, an analysis of both directions is done. The heights of the nanowire is 29 nm for both line directions, which is assumed to be the diameter of the nanowire. Now that the parameters of the nanowire are known, the convolution and subsequent deconvolution can be simulated, as shown in Fig. 6.8(c) and Fig. 6.8(d). In Fig. 6.8(c), a circular nanowire of diameter 29 nm has been simulated as this matches the

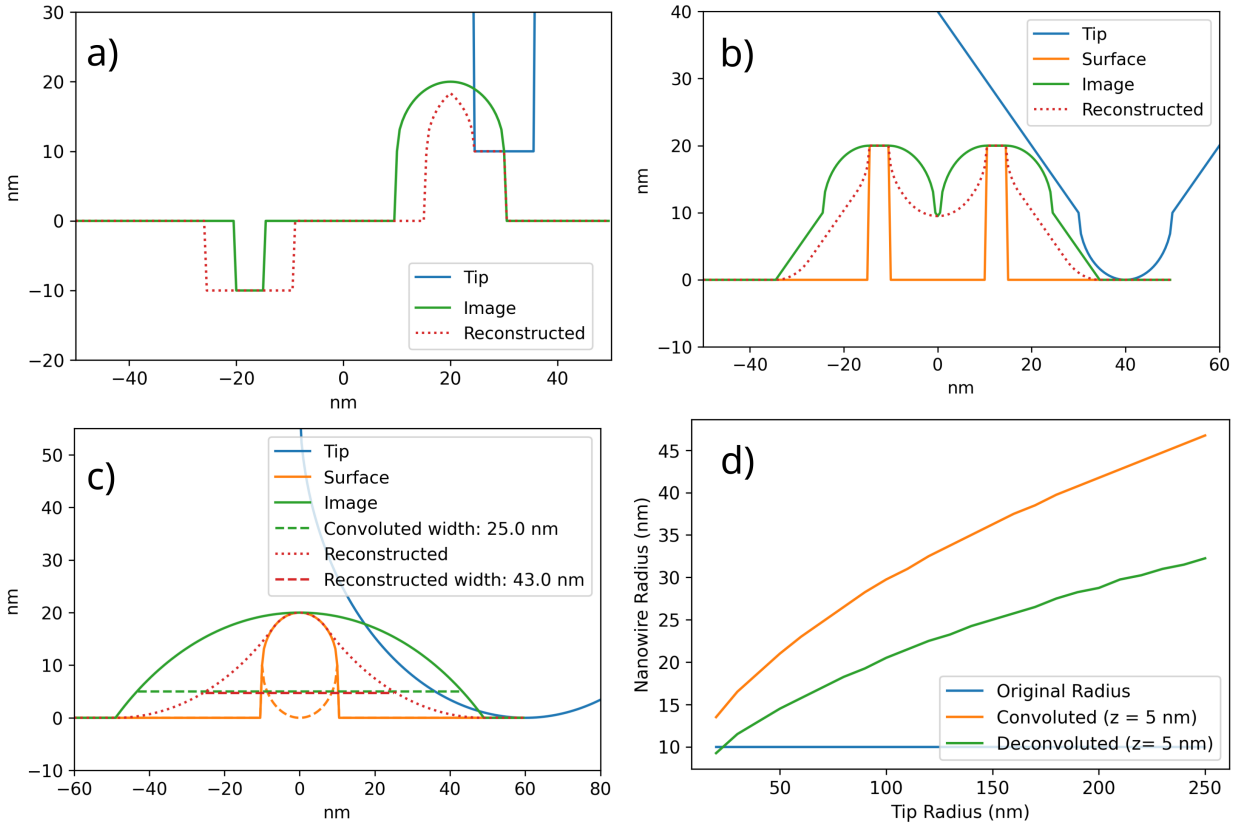

Figure 6.6: Two images that show the deconvolution of a tip with a sample. During the simulation, the apex of the tip follows the path of the surface and carves it out, giving the reconstructed image. (**a**) A mid-simulation image of a square tip eroding a small hole and a circle. Parameters: tip width 12 nm, hole depth 10 nm, hole width 5 nm, circle radius 10 nm. (**b**) Simulation of convolution and subsequent deconvolution of two tall structures with a circular tip. The deconvolution is not perfect, particularly in the area between the two tall structures. Parameters: tip radius 10 nm, structure height 20 nm, structure width 5 nm, structure separation 20 nm. (**c**) Simulation of convolution and subsequent deconvolution of a circular nanowire and circular tip. The width of the nanowires, measured at a height of z = 5 nm, is also shown. Parameters: tip radius 10 nm, nanowire radius 10 nm. (**d**) Graph showing the relationship between the relationship between tip radius and imaged / reconstructed nanowire diameter. The original nanowire has a radius of 10 nm, and the imaged nanowire has a larger radius after convolution and subsequent deconvolution. Since the onset of height increase is equal for both deconvoluted and convoluted nanowires, the radius has been measured at a height of 5 nm.

experimental height found. The tip-sample convolution has been simulated using a tip of diameter 1020 ± 20 nm. This tip has been chosen in order to make the experimental width of the nanowire match the convolued width of the nanowire. In Fig. 6.8(d), even though the simulated nanowire has a diameter of 28 nm, the tip and widths are all the same. Since the estimated tip diameter is 1020 ± 20 nm, this is very reasonable compared with the imaged tip diameters of 1170-1200 nm.

As seen in the large stiched-together scan in Fig. 6.7, the STM images of the nanowires do not always connect, and the nanowires do drift between successive scans. This is studied in Fig. 6.9, where a nanowire is scanned two times in a row and the results are analyzed. Over 20 minutes[1], the nanowire drifts at a rate of 4-9 nm / minute, which is due to a combination of piezoelectric, thermal, or nanowire drift, of which the latter could be due to the tip pushing the nanowire around as it scans. Future work to determine nanowire drift could be done by taking SEM images of the same area over a large timeframe, or finding a nanowire with a distinct surface feature nearby and scanning the area multiple times over a large timeframe.

Finally, another nanowire is presented in Fig. 6.10, which contains two nanowires side-by-side. The two nanowires have a diameter of 44.5 and 42.3 nm, and the spacing between them is 113 nm. According to the simulations, and assuming perfectly circular nanowires, this indicates that there is a separation of $113.0 - (44.5 + 42.3)/2 = 69.6$ nm between the two nanowires. Due to the loss of information due to convolution, it is impossible to determine if the space between contains smaller nanowires or nothing at all.

Topographical analysis of these nanowires requires a little more work than what was done before. In the original image, the slope on the left side of the nanowire has a lesser magnitude than the right side. The slope of an STM cross-section has a big impact on the convolution algorithms. If the image is adjusted such that the slopes are aligned, the image is distorted too much. Therefore, the slope has been adjusted such that the substrate is flat. This adjustment is valid due to two reasons: the exact rotation of the tip compared to the sample is unknown, and the slope compensation on an STM is never set to be perfectly zero, leading to slope offset. In order to attempt to simulate the topography, two nanowires have been simulated, shown in their original form in Fig. 6.10(b) These nanowires had diameters matching the experimental height of the nanowires, and the spacing between them was set by the separation between the two peaks. In order to simulate the convolution and obtain a reasonable estimate for the fit, a little more work must be done. The slope on the right side of the bundle is much steeper than the left side. Fig. 6.10(c) is has the nanowires located as they are in Fig. 6.10(b), and the tip diameter is fitted to make the left ends of the simulated

[1] 9.09s/line * 64 lines * 2 directions = 19.4 minutes

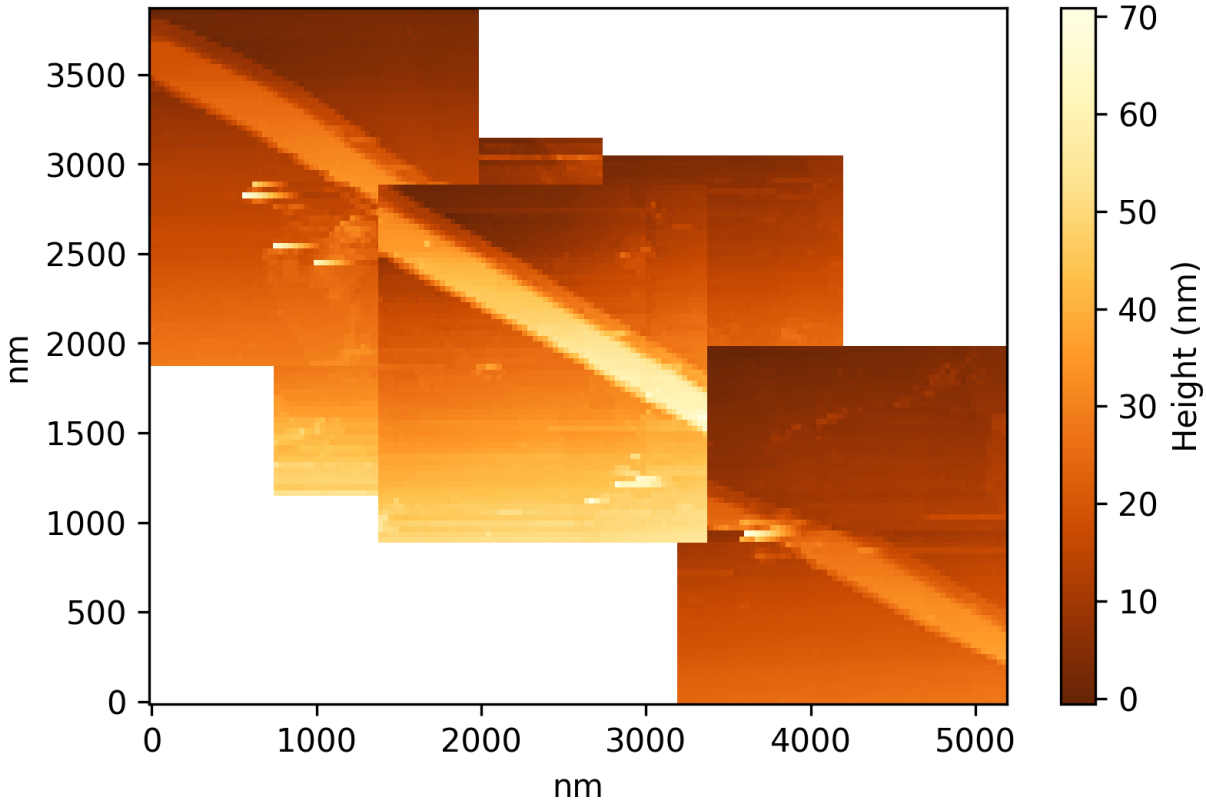

Figure 6.7: A collection of STM images following a doped CdS nanowire. The images have been stitched together according to the positions they were taken in. STM parameters (for all scans): -2.5 V, 40 pA, 9s line time, 64x64, UHV, RT

and experimental data meet. This results in a diameter of 2640 ± 40 nm. On the other hand, in Fig. 6.10(d), fitting the right end leads to a tip of diameter 533 ± 11 nm. Aligning the nanowires to be in the center of the bundle and fitting the total width, as shown in Fig. 6.10(e), leads to a diameters of 1387 ± 22 nm. Of these, only the fit in Fig. 6.10(e) is within reasonable parameters of tip diameters. Clearly, the assumption that the tip is perfectly circular begins to break down for this dataset. Similar to what was shown in blind tip estimation in Fig. 2.4(d), the simulated nanowire cannot fit inside the area between the two simulated nanowires, indicating the tip has a narrower profile, at least near the apex. It is entirely possible that this effect is due to a temporary tip shape reshaping, which occurs naturally when scanning.

Scanning tunneling spectroscopy on the nanowires is also included, presented in Fig. 6.11. As with the undoped data, there is not much difference between the HOPG and the CdS in terms of the normalized IV and dI/dV spectroscopy in Fig. 6.11(a,b). In terms of the Iz data, found in Fig. 6.11(c,d), there is a large difference between the CdS and HOPG. The

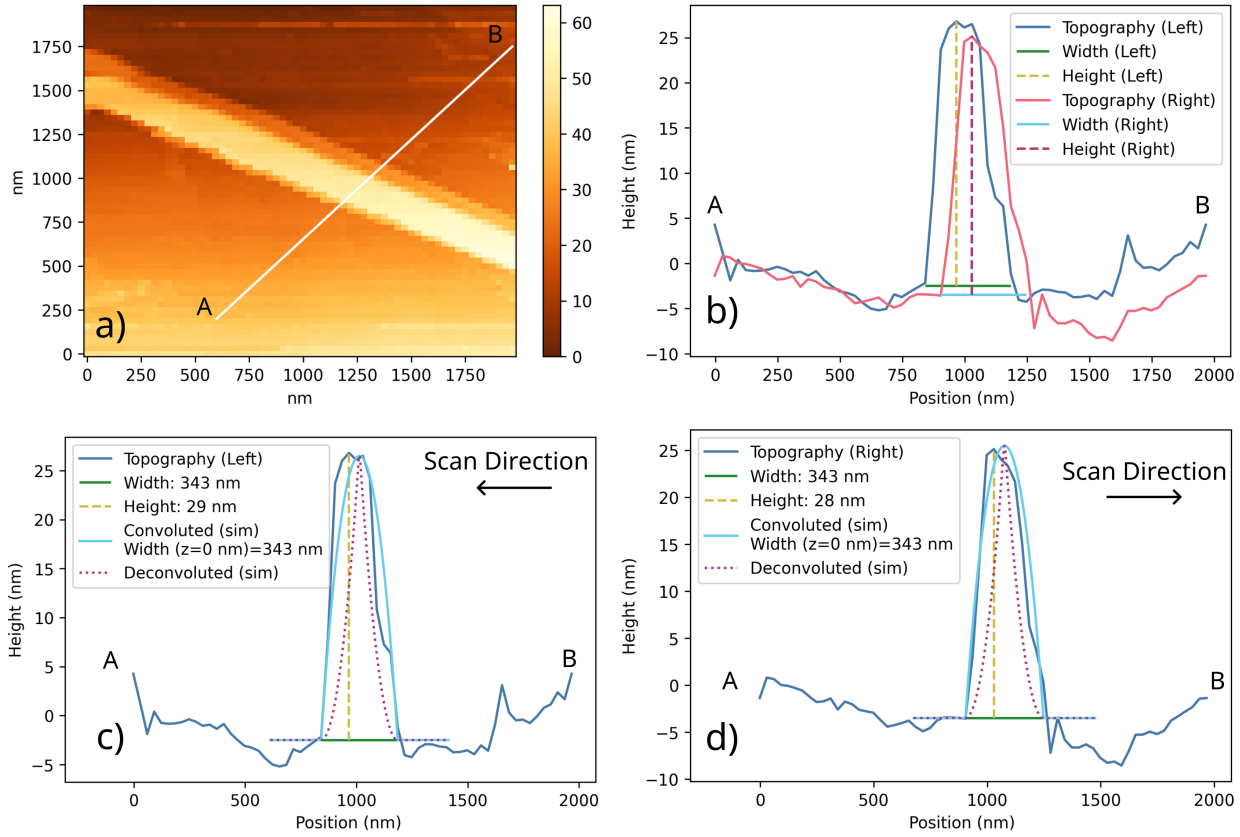

Figure 6.8: STM image of a doped CdS nanowire, which corresponds to one of the scans from Fig. 6.7. (**a**) STM image of the nanowire. (**b**) The height cross-sections, found from the lines in (a), as a function of position. Since the STM scans left-to-right and right-to-left, both of the lines are shown to compare. Two points on the line have been labeled to better see the direction of the line scan. (**c**) Left-to-right height cross section with analysis. A nanowire has been simulated, with an original diameter of 29 nm as this matches the experimental nanowire height. The simulation has been convoluted, and subsequently deconvoluted, using a tip of diameter 1020 ± 20 nm, which has been chosen to produce the same convoluted width as the experimental data. (**d**) Right-to-left height cross section with analysis. This has been simulated with a circular tip also of diameter 1020 ± 20 nm. STM parameters: -2.5 V, 40pA, 9s line time, 64x64, UHV, RT

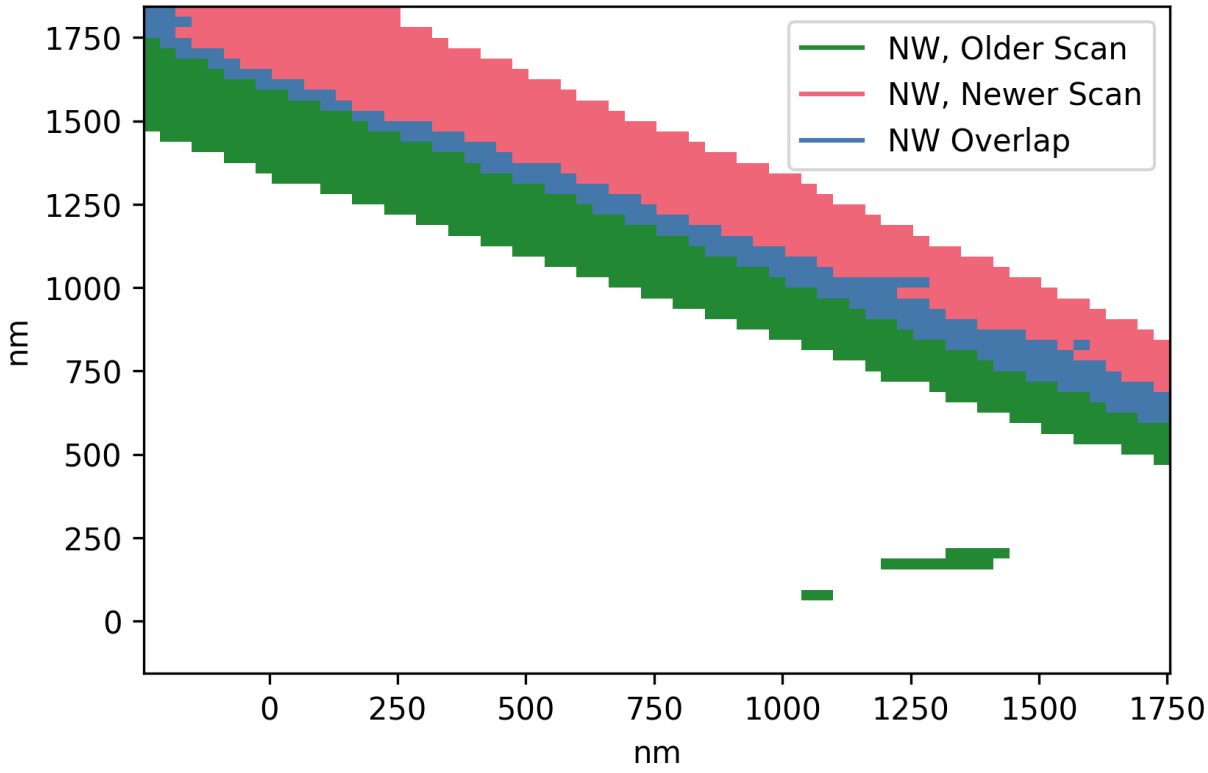

Figure 6.9: Two STM images of a doped CdS nanowire were taken in succession, covering the same region. Using a k-means clustering algorithm, an outline for the nanowire was found. Shown in the figure are the areas of the two nanowires, as well as their overlap. Depending on which points it is measured, the nanowire has moved by 80-180 nm. Each scan took 20 minutes. Therefore, the nanowire has moved at a rate of 4-9 nm / minute. STM parameters: -2.5 V, 40pA, 9s line time, 64x64, UHV, RT

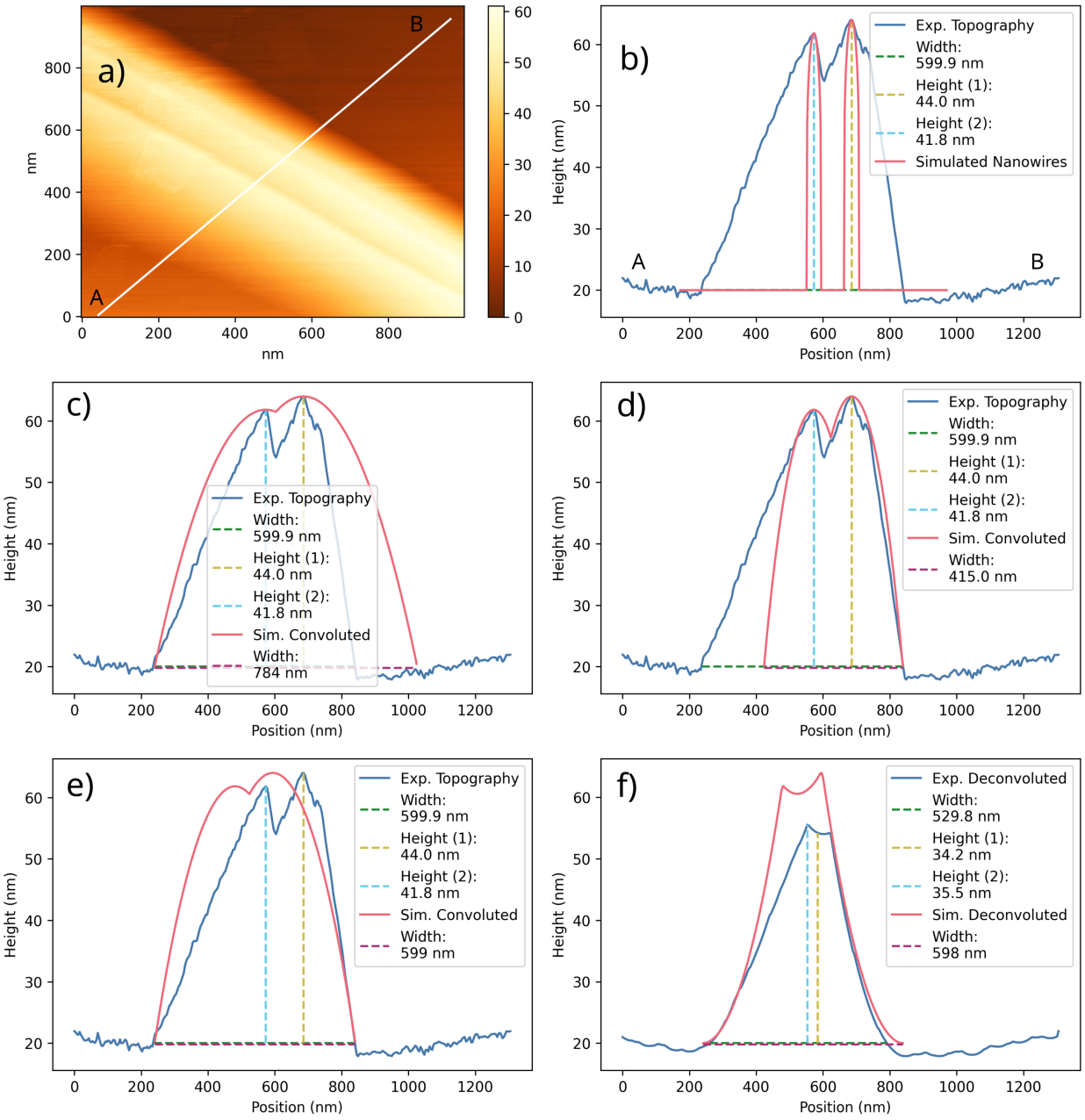

Figure 6.10: STM image of two bundled doped CdS nanowires side-by-side.(**a**) STM image of the nanowire. (**b**) The height cross-sections. Peak 1 has a height 44.0 nm, peak 2 has a height of 41.8 nm, the bundle width is 599.9 nm, and the peaks are separated by a distance of 113.0 nm. Two nanowires have been simulated, with diameters matching the experimental peak heights and separation matching what was found for the peaks. (**c-e**) Experimental data and simulated data from (b), where the simulated nanowires have been convoluted with a tip. (**c**) has a fitted tip of diameter 2640 ± 40 nm. This has been chosen in order to fit the leftmost edge of the nanowire. (**d**) has a fitted tip of diameter 533 ± 11 nm. This has been chosen in order to fit the rightmost edge of the nanowire. (**e**) has a fitted tip of diameter 1387 ± 22 nm. The nanowires have been shifted to be in the middle of the bundle, and the tip diameter has been chosen in order to make the same bundle width. (**f**) The deconvolution of the experimental and simulated data, both of which was done using the tip dimensions found in (e).

calculated apparent barrier height is 0.0248 +/- 0.008 eV for HOPG and 0.010 +/- 0.004 eV for CdS. Another data set was taken that same day, which can be found in Fig. 6.11(e). This data sets shows an apparent barrier height of 1.695 eV for HOPG and 0.747 eV for CdS. The locations of all Iz curves can be found in Fig. 6.11(f). Usual STM barrier heights are much larger, so these values are very unusual. Large biases have been shown to reduce the apparent barrier height [76], but this effect cannot fully explain the magnitude of the barrier height decreases and the difference between different values. Clearly, there is a great instability in any Iz measurements in this material. A possible reason for the instability could be the methanol used to prepare the solution. Although the methanol was fully evaporated by the time the sample was inserted into UHV, there may be trace effects left on the sample surface. Future studies on CdS NWs could explore the solvent used for deposition further. Another explanation could be vertical piezoelectric drift: in some instances, the tip height would increase over time even though the tip was positioned statically on the surface. Therefore, when an Iz curve was taken, the actual tip height change does not correspond exactly to what was reported by the electronics.

As mentioned in the introduction, THz-STM is a relatively new and unexplored way of analyzing samples. Therefore, this technique been applied to very few nanomaterials in the past. Although nanowires have been studied in STM before, the results presented in this section are the first to ever show THz-STM of a nanowire.

The first successful THz-STM signal can be found in Fig. 6.12. A THz field of -220 V/cm was incident on the tip, and the bias was modulated to simultaneously acquire an IV and I_{THz}V curve. Adjusting the parameters until a signal is found can be one of the hardest challenges in THz-STM. In some cases, a low setpoint means that any changes in current due to THz-STM will have a large signal-to-noise ratio and will be easier to read using a lock-in amplifier. In this case, a low setpoint of -32 mV and 7 pA was chosen. As shown in Fig. 6.12(a), this means that the electronics are easily saturated at high biases, since the tip is so close to the sample. Additionally, the THz component of the current is presented in Fig. 6.12(b), indicating that the parameters are suitable for obtaining a THz-STM signal. Both of these curves were acquired on HOPG.

Fig. 6.12(c) shows an IE graph on both HOPG and CdS, as well as curves with the THz blocked and the tip retracted. Since the THz signal is measured through a lock-in amplifier, the angle of the LIA must be set such that the background signal is minimized. However, this assumes that the background and THz signal are out of phase. In this case, this was not possible - the background signal was found in be in-phase with the THz signal. The background signal was found two different ways. When the tip is retracted, there is no current and therefore no THz current - therefore, all this signal is background. Additionally,

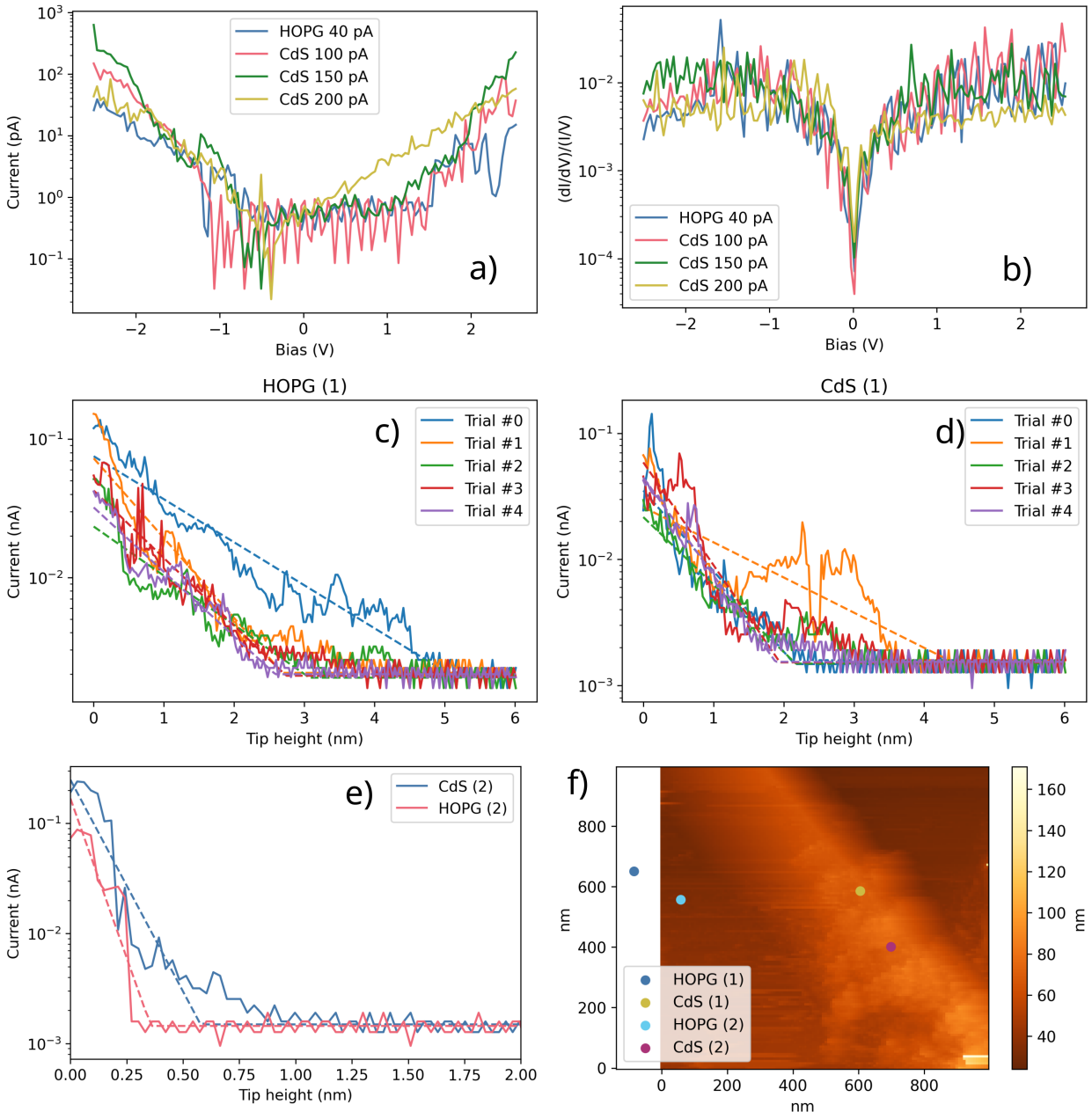

Figure 6.11: IV and dI/dV data on a Mn-doped CdS nanowire and HOPG substrate. (**a**) IV data, on a logarithmic scale for visibility. These scans have been taken at -2.5 V with varying setpoints. (**b**) Corrected dI/dV data, respectively, which has been divided by (I/V) for normalization. (**c,d**) Iz data for HOPG and CdS, respectively. The data is in a log scale with a bi-linear fit. The spectroscopies are taken at -2.5 V, 40 pA, with 30 pm steps. The calculated apparent barrier heights are 0.0248 +/- 0.008 eV for HOPG and 0.010 +/- 0.004 eV for CdS. (**e**) Iz data for HOPG and CdS, taken at a different location but the same parameters. The apparent barrier height is 1.695 eV for HOPG and 0.747 eV for CdS. (**f**) The locations of the Iz spectroscopies, including a data set that has been taken outside of the image bounds.

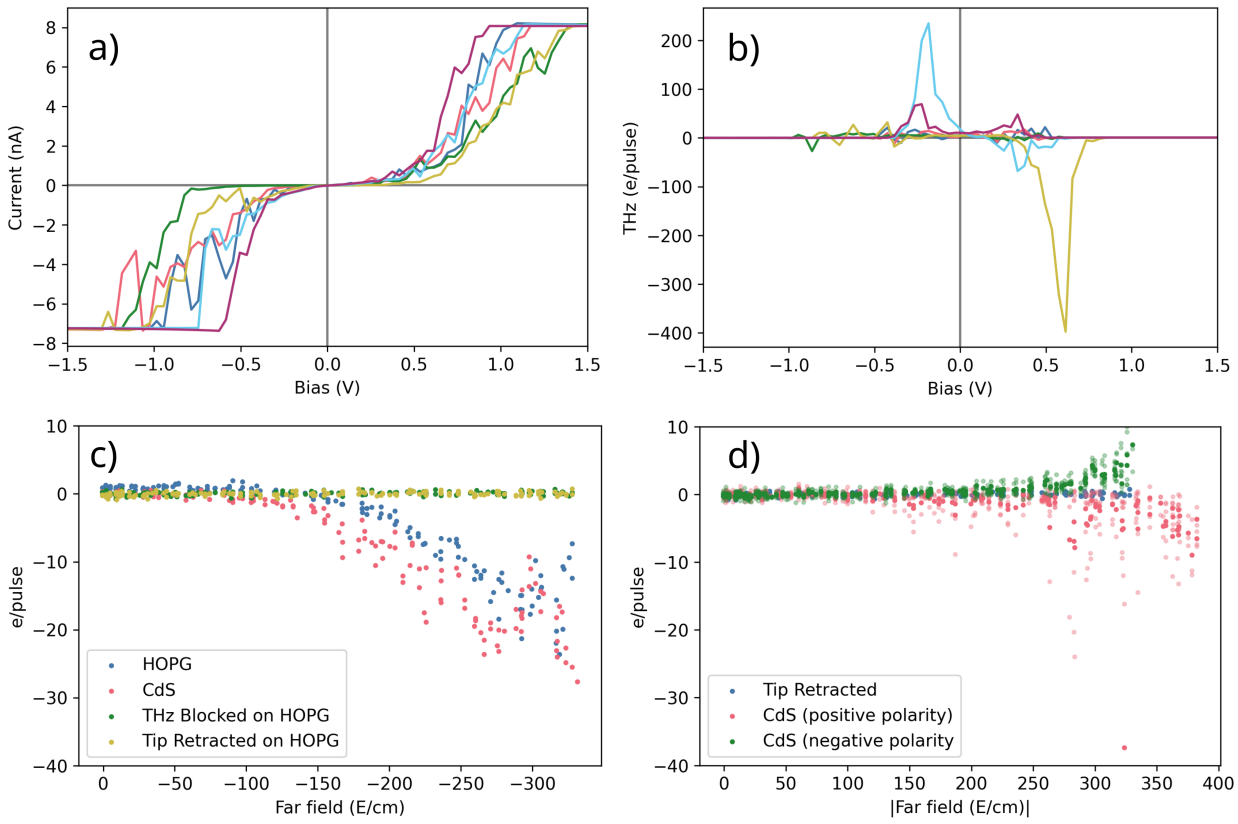

Figure 6.12: THz-STM data on both Mn-doped CdS nanowire and the underlying HOPG substrate. (**a**) IV curve on HOPG (**b**) I_{THz}V curve, showing the simultaneously acquired terahertz current. STM Parameters: -32 mV, 7 pA, -220 V/cm, UHV, RT. (**c**) IE curves on HOPG, CdS, and two different 'blocked' tests. Based on the 'blocked' tests, a flat value of -1.1 e/pulse was substracted to minimize the DC offset in the data. (**d**) IE curves on CdS, with two different electric field polarization directions.

when the THz is blocked after generation and does not arrive into the junction, the signal also represents the background signal. These two backgrounds are both a flat value of -1.1 e/pulse, so this was subtracted from all signals in order to remove the offset.

In Fig. 6.12(c), the CdS and HOPG data are both found using the exact same setpoints. Since the CdS has a higher signal than the HOPG, this is entirely due to the properties of the material. In Fig. 6.12(d), two different electric field polarities are compared, as well as another blocked test to verify that the signal is real.

Finally, a nanowire is shown in Fig. 6.13(a). This nanowire was studied in-depth over the course of two days, as it was easily found again the next day by keeping the tip hovering over it at a safe distance. The topographical analysis can be found in Fig. 6.13(b), which shows the simulated nanowire with diameter 30.7 nm as it matches the experimental height. Next, Fig. 6.13(c) shows the subsequent convolution to 373 nm. This was done with

a fitted tip diameter is 1134 ± 16 nm, which is an excellent fit when compared to the SEM images of tips. Finally, Fig. 6.13(d) shows the deconvolution of both the experimental and simulated data using the tip dimensions found earlier. This deconvolution has decreased the height slightly to 29.8 nm, most likely due to noise which can have a significant effect on image reconstruction [36].

This nanowire was also studied using THz-STM, the results of which can be found in Fig. 6.14. Fig. 6.14(a) shows the curves on HOPG, Fig. 6.14(b) shows the curves on CdS, and Fig. 6.14(c) shows the data on CdS with a blocked test to verify the signal. To further verify the signal, the THz field polarity was changed in Fig. 6.14(d). The spikes at polarities of 140 and 320 deg show that the signal is only present when the THz polarity is aligned with the tip direction, which is the condition for coupling. However, it is important to note that this differs from historical data which shows broader spikes (see ref. [25]). An explanation for this could be the low amount of rectified electrons due to the weak coupling with the tip.

Due to the difficulty in obtaining good THz-STM signals, a low-temperature study of the nanowires was undertaken next.

6.4 CdS NWs in UHV and 50 K

Liquid helium and liquid nitrogen are commonly used to cool down samples to minimize thermal effects. This usually makes it easier to obtain a THz-STM signal [5], and STM data with less noise. For the final leg of this thesis, the study of doped CdS nanowires in ultra-high-vacuum and 50 K temperatures will be discussed.

Although it is easy to cool down a THz-STM sample using liquid helium, there are unique challenges for these CdS nanowire samples. In room temperature studies, the tip can be left hovering over a nanowire overnight and it can be found easily the next day. However, this is not possible for low-temperature studies of nanowires. Due to safety reasons, the dewars containing liquid helium cannot be left open overnight. Therefore, each day of the experiment begins with a cooling down process that takes 1.5-2.5 hours. Cooling down also leads to thermal drift - if a nanowire is found at room temperature, the system cannot be cooled down with the hopes of finding the nanowire at its old position. Due to the difficulty of finding nanowires, only two nanowires were found using this method, of which only one is presented..

The CdS nanowire acquired at 50 K can be found in Fig. 6.15. Surprisingly, the image was very unstable, which required a low line count and slow scan speed to produce decent images. This nanowire is seemingly on the edge of an atomic step, so it is unknown if

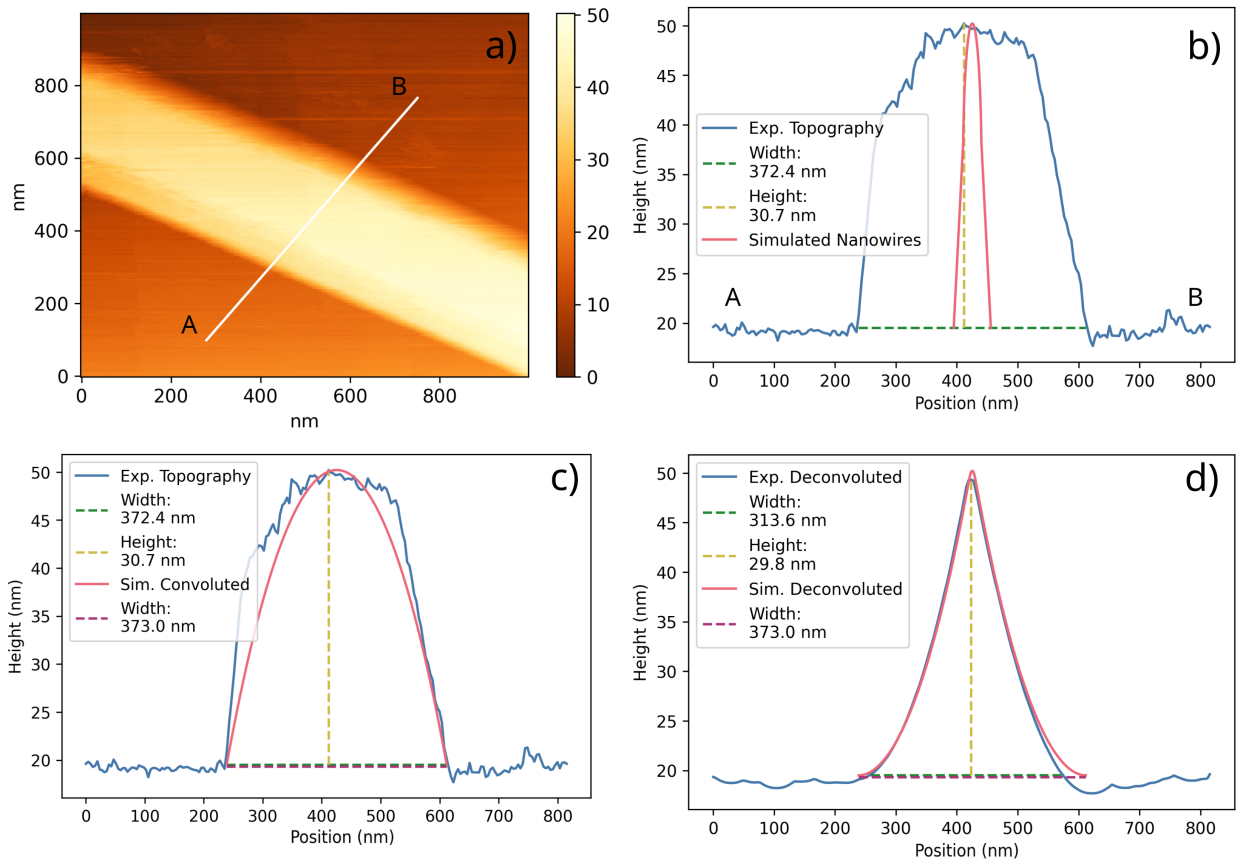

Figure 6.13: STM image of a Mn-doped CdS nanowire.(**a**) STM image of the nanowire.(**b**) The height cross-section, found from the line in (a), as a function of position. The peak height is 30.7 nm, with a total width of 372.4 nm. A single nanowire been simulated, with diameters matching the experimental peak height. (**c**) The experimental data and the convoluted simulation data, which was found using a circular tip with a fitted diameter of 1134 $\pm$ 16 nm. The new simulated width is 373 nm. (**d**) The deconvolution of the experimental and simulated data. The deconvolunted experimental peak height is 29.8 nm, and its new width is 313.6 nm. The deconvoluted simulation topography has changed shape, although its width is still 373 nm. STM parameters: -2.5 V, 44pA, 6.7s line time, 256x256, UHV, RT

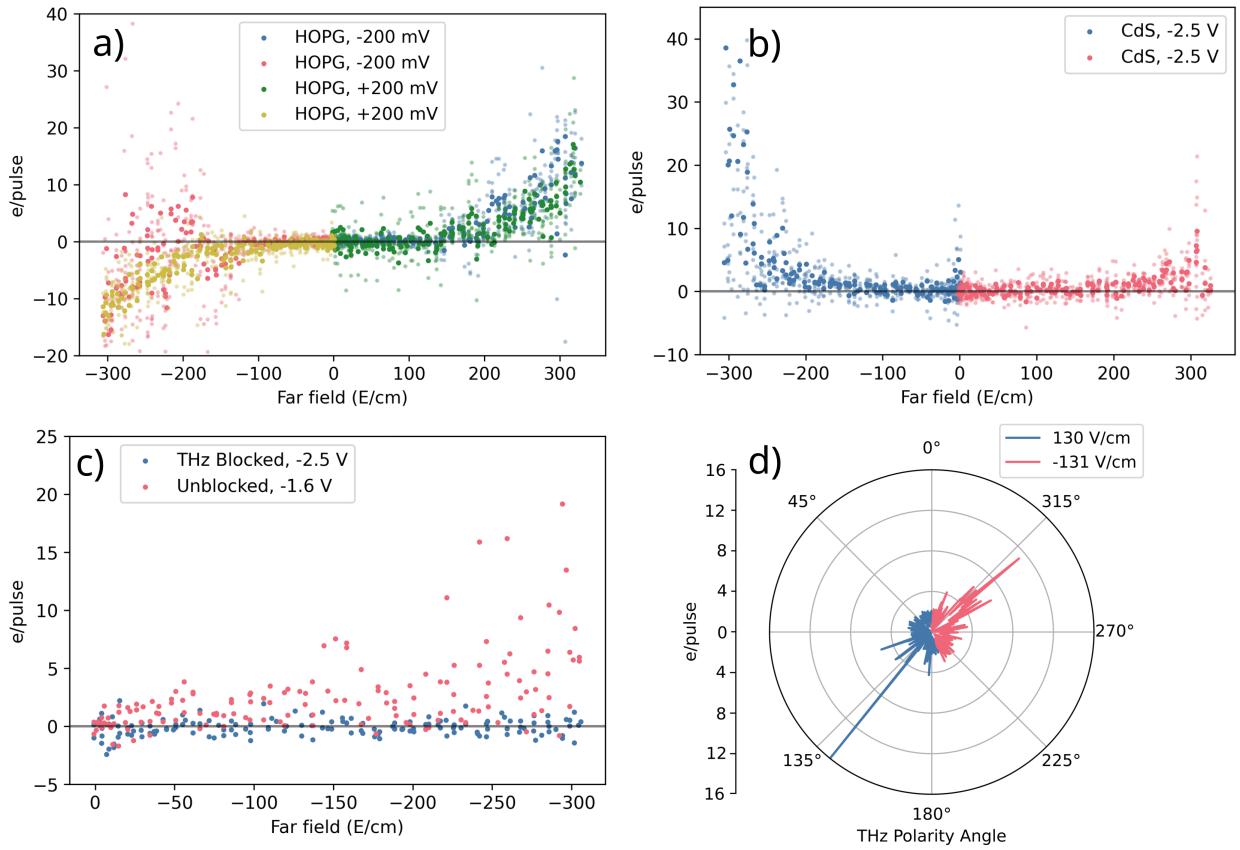

Figure 6.14: THz-STM data on both Mn-doped CdS and the underlying HOPG substrate. (**a**) IE data on HOPG. A case for each bias and electric field polarity is shown. This was done at 10 pA. (**b**) IE data on CdS, with opposing electric field polarities. This was done at -2.5 V, 40 pA. (**c**) Two IEs on CdS, with another block test to verify that the signal from this nanowire is real. This was done at 40 pA. (**d**) A polar plot of the THz polarity vs THz current. The two spikes correspond to the THz field being polarized along the direction of the tip, which equals maximum coupling. This was found at -2.5 V, 40 pA, on CdS.

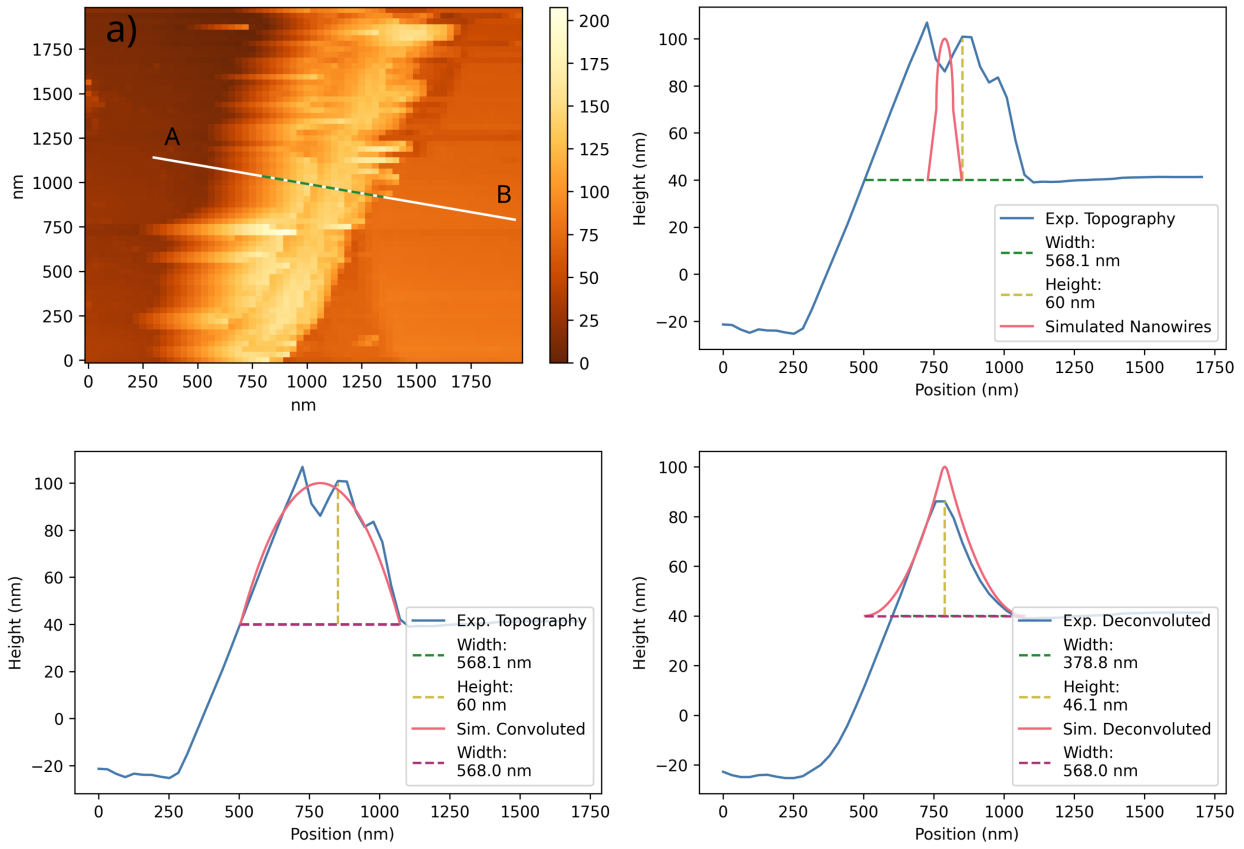

Figure 6.15: STM image of an Mn-doped CdS nanowire at 50 K.(**a**) STM image of the nanowire (b).(**b**) The height cross-section, found from the line in (a), as a function of position. The peak height is 60 nm, with a total width of 568.1 nm. A single nanowire been simulated, with diameters matching the experimental peak height. (**c**) The experimental data and the convoluted simulation data, which was found using a fitted circular tip of diameter 1348 $\pm$ 12 nm. The new simulated width is 488 nm. (**d**) The deconvolution of the experimental and simulated data. The deconvolunted experimental peak height is 47.1 nm, with a width of 441.9 nm. The deconvoluted simulation topography has changed shape, although all the other parameters remained the same. STM parameters: -2.5 V, 41pA, 11.4s line time, 64x64, UHV, 50 K

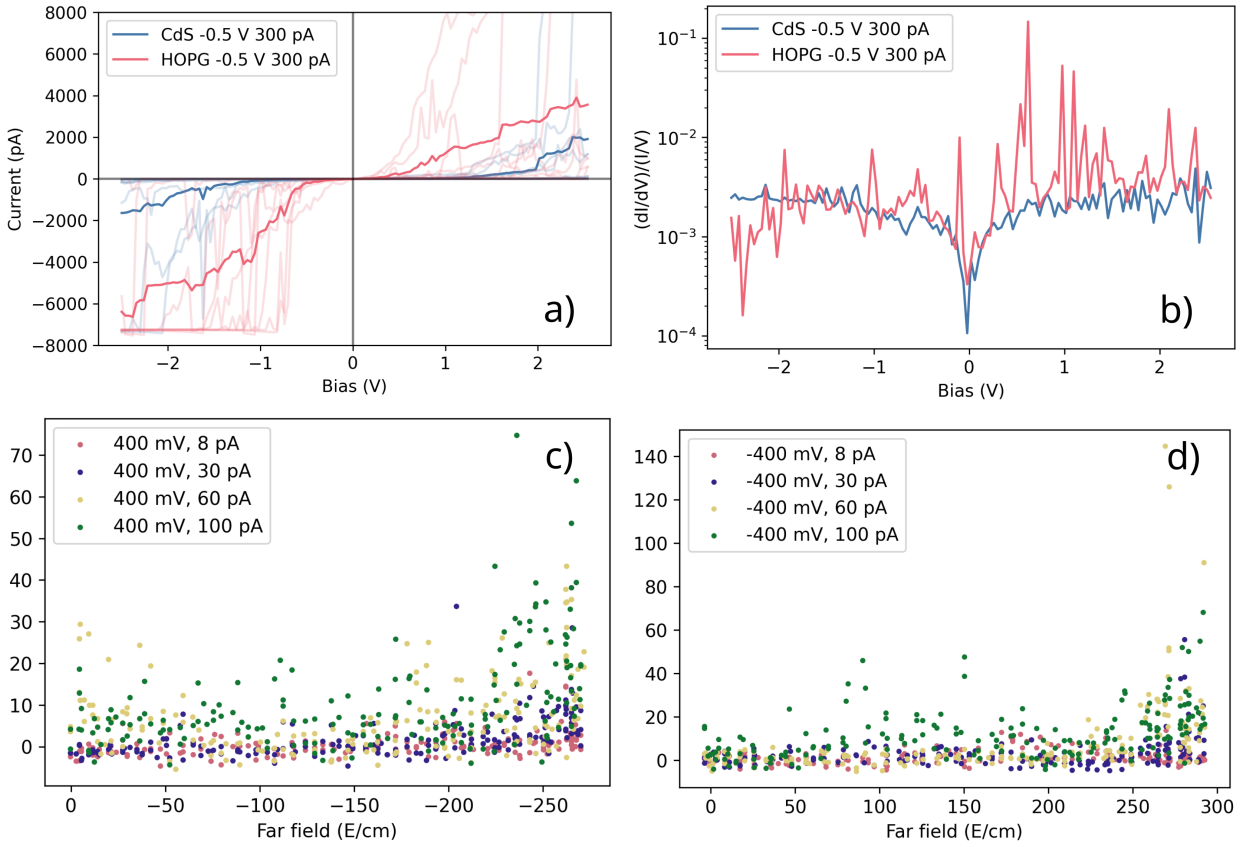

Figure 6.16: STM of an Mn-doped CdS nanowire at 50 K. (**a,b**) The IV and dI/dV characteristics, respectively, of the nanowire and substrate, both of which were taken at -0.5 V and 300 pA. (**c,d**) The IE characteristics of the CdS nanowire with negative and positive polarity THz fields, respectively.

it is lying on the upper or lower plane. For the simulations, it is assumed that the nanowire is on the upper plane and only has a height of 60 nm. Despite the overall topographical noisiness, the results suggest a good fit. The simulated tip has a diameter of 1348 ± 12 nm, which agrees with the SEM images.

There is also STM and THz-STM data on this nanowire, which can be found in Fig. 6.16. There is a strong difference in the IV characteristics between HOPG and CdS, which gives a good indication of them being different materials. However, the normalized dI/dV data does not indicate as much of a difference between the two. Additionally, THz-STM signals are presented, which seems to indicate an equal amount of signal for positive bias/negative THz electric field and negative bias/positive THz electric field.

6.5 Contact Pump-Probe on GaAs (110) and CdS

One of the main objectives of this work was to get an OPP-THz-STM signal on CdS nanowires to obtain a measure of the photocarrier decay and charge separation in the nanowire. Prior to this, it was important to establish a baseline experiment using a known material. The (110) plane of GaAs is a well-established material in THz-STM and is currently being investigated in crashed-THz-STM experiments. Therefore, a pump-probe experiment was performed in order to confirm that the pump optics were working and that the optical fluence of the 400 nm pump was enough to obtain a signal. The results can be found in Fig. 6.17. Fig. 6.17(a) shows the time-dependent OPP-THz-STM signal, with the values of stage position included for later comparison. Fig. 6.17(b) shows a more zoomed-in version, and the corresponding EOS sampling of the THz pulse for comparison. Fig. 6.17(c) and Fig. 6.17(d) show the dependence of the pump polarity and THz polarity - although there is some misalignment, the polarization-dependent results confirm that the alignment of polarization and tip direction yields a stronger signal. For the pump polarization, the sideways direction also yields a lower but significant amount of coupling.

Despite trying to obtain an OPP-THz-STM signal on undoped CdS nanowires at room temperature, doped CdS nanowires at room temperature, and doped CdS nanowires at 50 K, a successful result was not obtained. None of the attempts were able to show a distinguishable feature, only the constant background. One such attempt, taken on the nanowire shown in Fig. 6.15, is shown in Fig. 6.17(e). The stage position is usually not shown as it is intended for internal use only, but in this case it has been included to highlight that the signal was measured using the same time-delay parameters in Fig. 6.17(a).

To summarize this chapter, an in-depth analysis of the tip radius and its effects on the tip-sample convolution was made using known parameters. STM images of nanowires at room temperature and 50 K were presented. The nanowire dimensions were extracted and compared to what was found via SEM. Tip dimensions were fitted to the data and resulted in a good comparison with the SEM images of the tips. Additionally, the deconvolution of the tip and sample was shown, although it was not enough to fully restore the nanowire dimensions. Various spectroscopies on nanowires were shown, yielding a contrast between the sample and the substrate. THz-STM results on cold and room temperature nanowires was shown, as well as OPP-THz-STM data on GaAs to compare with the lack of results on CdS.

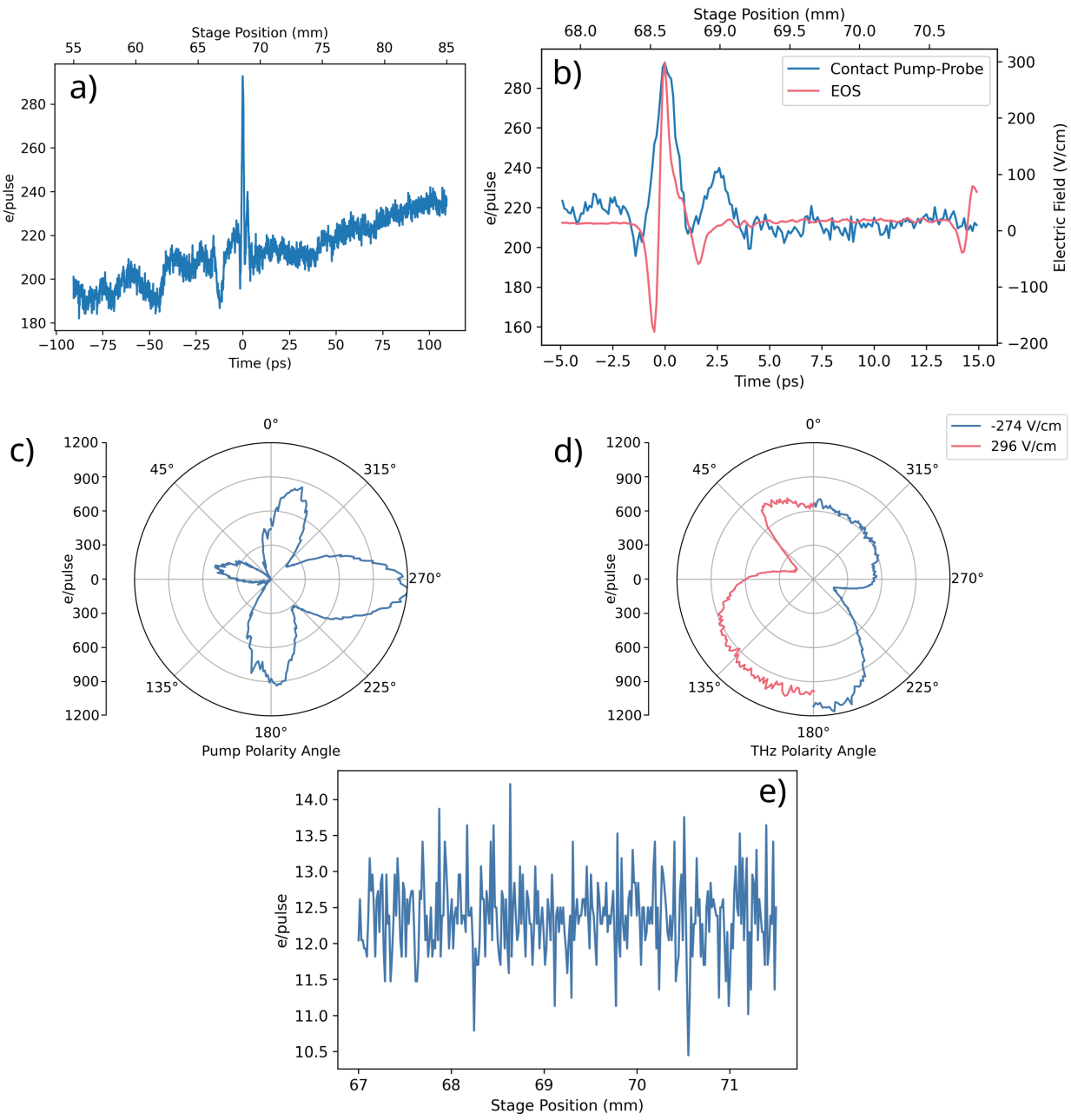

Figure 6.17: Optical pump-THz probe experiments using a 400 nm pump. (**a**) OPP-THz-STM signal on GaAs, where the spike represents the intersection between the pump and THz probe signal. This was done using a W tip that was crashed into GaAs (110) at 0V, 13 μW of power and a THz field of 296 V/cm. (**b**) Zoomed-in version of the OPP-THz-STM signal, and the EOS pulse for comparison. (**c,d**) The THz polarity dependence and pump polarity dependence, respectively. (**e**) An OPP-THz-STM attempt on doped CdS nanowire at 50 K. This was taken at -200 mV, 5 pA, 400 nm single lens configuration.

Chapter 7

Conclusions

The primary focus of this work was to do THz-STM on CdS nanowires. The conventional STM side of this technique has the ability to obtain the atomic structure and electronic structure of a surface with sub-nanometer spatial precision. On the THz side, this technique has the ability to measure the temporal dynamics on a sub-picosecond timescale, allowing it to measure ultrafast electron dynamics. As a burgeoning field of condensed matter physics and ultrafast optics, THz-STM has been proven as a powerful method to measure electron dynamics. Previous TRTS work on CdS nanowires showed a long charge separation, which prompted an interest in a THz-STM study. As described earlier, the THz-STM has the ability to take this spectroscopy on a specific nanowire - a powerful feature unavailable in the past. Since THz-STM studies of nanostructures remain limited, this was a good objective for an MSc thesis.

In order to work towards the ultimate result of OPP-THz-STM, it was first important to establish a baseline for these experiments using a similar method known as photoemission. Results of this technique were shown, showing the interaction between the THz pump and optical pump. Careful steps were taken in order to prove that the signal was a result of actual rectified electrons instead of just being noise. A dependence on THz polarity was shown, proving that the coupling only happens when the THz field is aligned with the tip.

Undoped CdS nanowires were then shown, starting with images obtained using SEM to show the spread and dimensions of the nanowires. Results obtained in an ambient system designed for rapid turnaround of samples were presented next. Images of nanowires were presented where the topography of the nanowire is clearly contrasted against the underlying substrate. Additionally, several images were stitched together to show the extent of the nanowire. Next, the results in an ultra-high vacuum THz-STM were shown. More nanowire images were included, especially a bundle of nanowires which was analyzed in order to

determine how many nanowires comprised the bundle and their locations. Spectroscopy on various different points of the nanowire was included as well. A bias-dependent scanning was proven, indicating the semiconducting nature of the nanowires and the importance of choosing the correct parameters. THz-STM results were also shown, proving the ability of THz-STM to get a signal on the substrate. The physical dimensions of the nanowires were examined as well, although they could not properly be explained until the next chapter.

Doped CdS nanowires were also presented, starting with an SEM profile of the nanowires. To address the issue of physical dimensions of the previous chapter, the tip used for data collection was imaged using SEM. Simulations using realistic parameters, obtained using SEM, showed how the nanowire dimensions could be increased drastically by the tip-sample convolution. A deconvolution algorithm was also shown, which represented the best mathematical way to obtain the original sample topography. Several images of nanowires were shown, which were analyzed using the techniques developed in this chapter to show that the realistic parameters obtained do result in the images shown. Spectroscopy on these nanowires was also shown. The topography of the nanowires when cooled to 50 K using liquid helium was also shown, and compared as was done before. THz-STM of the nanowires was shown, being the first of its kind for a nanowire. Finally, an unsuccessful OPP-THz-STM waveform on a cold doped CdS nanowire was shown, contrasted with a quick aside on a successful OPP-THz-STM crashed-GaAs experiment. For this, a THz and pump polarity dependence was shown.

There are many avenues for future studies on CdS nanowires with THz-STM. A THz-STM with a built-in SEM would greatly reduce the difficulty of finding nanowires, and could validate the assumptions made about the nanowire widths and tip convolution. Alternative tip-making methods could be explored to try and obtain a smaller tip apex, decreasing the apparent width of the nanowires. Finally, varying the CdS doping material and amounts can provide new samples for study.

References

[1] Tyler Cocker et al. "An ultrafast terahertz scanning tunnelling microscope". In: *Nature Photonics* 7 (July 7, 2013), pp. 620–625. DOI: 10.1038/nphoton.2013.151.

[2] Adam J. M. Wollman et al. "From Animaculum to single molecules: 300 years of the light microscope". In: *Open Biology* 5.4 (Apr. 29, 2015), p. 150019. ISSN: 2046-2441. DOI: 10.1098/rsob.150019.

[3] Martin M. Freundlich. "Origin of the Electron Microscope". In: *Science* 142.3589 (Oct. 11, 1963). Publisher: American Association for the Advancement of Science, pp. 185–188. DOI: 10.1126/science.142.3589.185.

[4] G. Binnig and H. Rohrer. "Scanning tunneling microscopy". In: *Surface Science* 126.1 (Mar. 2, 1983), pp. 236–244. ISSN: 0039-6028. DOI: 10.1016/0039-6028(83)90716-1.

[5] Vedran Jelic et al. "Ultrafast terahertz control of extreme tunnel currents through single atoms on a silicon surface". In: *Nature Physics* 13.6 (June 2017). Publisher: Nature Publishing Group, pp. 591–598. ISSN: 1745-2481. DOI: 10.1038/nphys4047.

[6] Emelie Hilner et al. "Direct Atomic Scale Imaging of III V Nanowire Surfaces". In: *Nano Letters* 8.11 (Nov. 12, 2008), pp. 3978–3982. ISSN: 1530-6984, 1530-6992. DOI: 10.1021/nl802500d.

[7] R. M. Feenstra. "Tunneling spectroscopy of the (110) surface of direct-gap III-V semiconductors". In: *Physical Review B* 50.7 (Aug. 15, 1994), pp. 4561–4570. ISSN: 0163-1829, 1095-3795. DOI: 10.1103/PhysRevB.50.4561.

[8] Eadweard Muybridge. *The horse in motion, first successful photographs of an animal in motion, forerunner of the motion picture*. Library of Congress, Washington, D.C. 20540 USA. 1878. URL: https://www.loc.gov/item/2005684184/ (visited on 06/05/2024).

[9] Carlo Sirtori. "Bridge for the terahertz gap". In: *Nature* 417.6885 (May 2002), pp. 132–133. ISSN: 0028-0836, 1476-4687. DOI: 10.1038/417132b.

[10] D. H. Auston and P. R. Smith. "Generation and detection of millimeter waves by picosecond photoconductivity". In: *Applied Physics Letters* 43.7 (Oct. 1, 1983), pp. 631–633. ISSN: 0003-6951. DOI: 10.1063/1.94468.

[11] Alexander Andronov et al. "Stimulated emission in the long-wavelength IR region from hot holes in Ge in crossed electric and magnetic fields". In: *Jetp Letters - JETP LETT-ENGL TR* 40 (Jan. 1, 1984).

[12] Erik Bründermann, Danielle R. Chamberlin, and Eugene E. Haller. "High duty cycle and continuous terahertz emission from germanium". In: *Applied Physics Letters* 76.21 (May 22, 2000), pp. 2991–2993. ISSN: 0003-6951. DOI: 10.1063/1.126555.

[13] Rüdeger Köhler et al. "Terahertz semiconductor-heterostructure laser". In: *Nature* 417.6885 (May 2002). Publisher: Nature Publishing Group, pp. 156–159. ISSN: 1476-4687. DOI: 10.1038/417156a.

[14] Jerome Faist et al. "Quantum Cascade Laser". In: *Science* 264.5158 (Apr. 22, 1994). Publisher: American Association for the Advancement of Science, pp. 553–556. DOI: 10.1126/science.264.5158.553.

[15] Benjamin S. Williams et al. "Operation of terahertz quantum-cascade lasers at 164 K in pulsed mode and at 117 K in continuous-wave mode". In: *Optics Express* 13.9 (May 2, 2005). Publisher: Optica Publishing Group, pp. 3331–3339. ISSN: 1094-4087. DOI: 10.1364/OPEX.13.003331.

[16] János Hebling et al. "Velocity matching by pulse front tilting for large-area THz-pulse generation". In: *Optics Express* 10.21 (Oct. 21, 2002). Publisher: Optica Publishing Group, pp. 1161–1166. ISSN: 1094-4087. DOI: 10.1364/OE.10.001161.

[17] S. S. Dhillon et al. "The 2017 terahertz science and technology roadmap". In: *Journal of Physics D: Applied Physics* 50.4 (Jan. 2017). Publisher: IOP Publishing, p. 043001. ISSN: 0022-3727. DOI: 10.1088/1361-6463/50/4/043001.

[18] Jesus A.M. Calzada. "Terahertz scanning tunneling microscopy on metals, semiconductors, and carbon nanostructures". PhD thesis. University of Alberta, 2024.

[19] Kazi M. Alam et al. "Photocatalytic Mechanism Control and Study of Carrier Dynamics in CdS@C $_3$ N $_5$ Core–Shell Nanowires". In: *ACS Applied Materials & Interfaces* 13.40 (Oct. 13, 2021), pp. 47418–47439. ISSN: 1944-8244, 1944-8252. DOI: 10.1021/acsami.1c08550.

[20] Donna Strickland and Gerard Mourou. "Compression of amplified chirped optical pulses". In: *Optics Communications* 55.6 (Oct. 15, 1985), pp. 447–449. ISSN: 0030-4018. DOI: 10.1016/0030-4018(85)90151-8.

[21] Charles E. Jensen. *Ultrafast imaging of nonlinear terahertz dynamics in semiconductors*. ERA. 2017. DOI: 10.7939/R3SB3XC53. URL: https://era.library.ualberta.ca/items/515ccca2-f945-4fe3-8dca-b5356d4b2af9 (visited on 06/06/2024).

[22] Charles E. Jensen. "Time-Resolved Terahertz Spectroscopy of Semiconductor Nanomaterials". PhD thesis. University of Alberta, 2024.

[23] T. L. Cocker et al. "Nanoscale terahertz scanning probe microscopy". In: *Nature Photonics* 15.8 (Aug. 2021). Publisher: Nature Publishing Group, pp. 558–569. ISSN: 1749-4893. DOI: 10.1038/s41566-021-00835-6.

[24] Tyler L. Cocker et al. "Tracking the ultrafast motion of a single molecule by femtosecond orbital imaging". In: *Nature* 539.7628 (Nov. 2016). Publisher: Nature Publishing Group, pp. 263–267. ISSN: 1476-4687. DOI: 10.1038/nature19816.

[25] Vedran Jelic. *Imaging Ultrafast Dynamics on the Atomic Scale with a Terahertz Scanning Tunneling Microscope*. ERA. 2019. DOI: 10.7939/r3-cwvj-6639. URL: https://era.library.ualberta.ca/items/718be8a4-d91e-4bd0-bac0-b0360ba711ea (visited on 06/06/2024).

[26] Ammerman, Spencer E. "Ultrafast terahertz microscopy of atomically precise graphene nanoribbons". PhD thesis. [object Object], 2021. DOI: 10.25335/9DA2-Q933.

[27] Kan Zhang et al. "Tuning the charge transfer route by p–n junction catalysts embedded with CdS nanorods for simultaneous efficient hydrogen and oxygen evolution". In: *Journal of Materials Chemistry A* 3.9 (2015), pp. 4803–4810. ISSN: 2050-7488, 2050-7496. DOI: 10.1039/C4TA05571C.

[28] Kaifeng Wu et al. "Ultrafast Charge Separation and Long-Lived Charge Separated State in Photocatalytic CdS–Pt Nanorod Heterostructures". In: *Journal of the American Chemical Society* 134.25 (June 27, 2012), pp. 10337–10340. ISSN: 0002-7863, 1520-5126. DOI: 10.1021/ja303306u.

[29] Bert Voigtländer. *Scanning Probe Microscopy: Atomic Force Microscopy and Scanning Tunneling Microscopy*. Google-Books-ID: e4vPBgAAQBAJ. Springer, Feb. 24, 2015. 375 pp. ISBN: 978-3-662-45240-0.

[30] Roland Wiesendanger. *Scanning Probe Microscopy and Spectroscopy: Methods and Applications*. Google-Books-ID: EXae0pjS2vwC. Cambridge University Press, Sept. 29, 1994. 664 pp. ISBN: 978-0-521-42847-7.

[31] Joseph A. Stroscio, R. M. Feenstra, and A. P. Fein. "Electronic Structure of the Si(111) 2 x1 Surface by Scanning-Tunneling Microscopy". In: *Physical Review Letters* 57.20 (Nov. 17, 1986). Publisher: American Physical Society, pp. 2579–2582. DOI: 10.1103/PhysRevLett.57.2579.

[32] R. M. Feenstra et al. "Atom-selective imaging of the GaAs(110) surface". In: *Physical Review Letters* 58.12 (Mar. 23, 1987). Publisher: American Physical Society, pp. 1192–1195. DOI: 10.1103/PhysRevLett.58.1192.

[33] Eloy Anguiano, Ai Oliva, and Marilyn Aguilar. "Optimal conditions for imaging in scanning tunneling microscopy: Theory". In: *Review of Scientific Instruments - REV SCI INSTR* 69 (Nov. 1, 1998), pp. 3867–3874. DOI: 10.1063/1.1149191.

[34] Rakesh P. Borase et al. "A review of PID control, tuning methods and applications". In: *International Journal of Dynamics and Control* 9.2 (June 1, 2021), pp. 818–827. ISSN: 2195-2698. DOI: 10.1007/s40435-020-00665-4.

[35] A. I. Oliva et al. "Analysis of scanning tunneling microscopy feedback system". In: *Review of Scientific Instruments* 66.5 (May 1, 1995), pp. 3196–3203. ISSN: 0034-6748. DOI: 10.1063/1.1145551.

[36] J.S. Villarrubia. "Algorithms for scanned probe microscope image simulation, surface reconstruction, and tip estimation". In: *Journal of Research of the National Institute of Standards and Technology* 102.4 (July 1997), p. 425. ISSN: 1044677X. DOI: 10.6028/jres.102.030.

[37] K. I. Schiffmann et al. "Correction of STM tip convolution effects in particle size and distance determination of metal-C:H films". In: *Fresenius' Journal of Analytical Chemistry* 358.1 (May 1, 1997), pp. 341–344. ISSN: 1432-1130. DOI: 10.1007/s002160050424.

[38] Kirsten I. Schiffmann et al. "Statistical methods for the correction of tip convolution effects in STM imaging of nanometer size particles in metal—C: H films". In: *Ultramicroscopy* 66.3 (Dec. 1, 1996), pp. 183–192. ISSN: 0304-3991. DOI: 10.1016/S0304-3991(96)00086-1.

[39] Yun-Shik Lee. *Principles of Terahertz Science and Technology*. Boston, MA: Springer US, 2009. ISBN: 978-0-387-09539-4 978-0-387-09540-0. DOI: 10.1007/978-0-387-09540-0.

[40] L. Duvillaret et al. "Analytical modeling and optimization of terahertz time-domain spectroscopy experiments, using photoswitches as antennas". In: *IEEE Journal of Selected Topics in Quantum Electronics* 7.4 (July 2001). Conference Name: IEEE Journal of Selected Topics in Quantum Electronics, pp. 615–623. ISSN: 1558-4542. DOI: 10.1109/2944.974233.

[41] Elchin Isgandarov et al. "Intense terahertz generation from photoconductive antennas". In: *Frontiers of Optoelectronics* 14.1 (Mar. 1, 2021), pp. 64–93. ISSN: 2095-2767. DOI: 10.1007/s12200-020-1081-4.

[42] Zhisheng Piao, Masahiko Tani, and Kiyomi Sakai. "Carrier Dynamics and Terahertz Radiation in Photoconductive Antennas". In: *Japanese Journal of Applied Physics* 39.1 (Jan. 1, 2000). Publisher: IOP Publishing, p. 96. ISSN: 1347-4065. DOI: 10.1143/JJAP.39.96.

[43] S.L. Teitel and J.W. Wilkins. "Ballistic transport and velocity overshoot in semiconductors: Part I—Uniform field effects". In: *IEEE Transactions on Electron Devices* 30.2 (Feb. 1983). Conference Name: IEEE Transactions on Electron Devices, pp. 150–153. ISSN: 1557-9646. DOI: 10.1109/T-ED.1983.21088.

[44] F. G. Sun, G. A. Wagoner, and X.-C. Zhang. "Measurement of free-space terahertz pulses via long-lifetime photoconductors". In: *Applied Physics Letters* 67.12 (Sept. 18, 1995), pp. 1656–1658. ISSN: 0003-6951. DOI: 10.1063/1.115047.

[45] Peter H. Nguyen et al. "Modeling the Terahertz Pulse Induced Transient Bias in the STM Junction". In: *2020 45th International Conference on Infrared, Millimeter, and Terahertz Waves (IRMMW-THz)*. 2020 45th International Conference on Infrared, Millimeter, and Terahertz Waves (IRMMW-THz). ISSN: 2162-2035. Nov. 2020, pp. 1–2. DOI: 10.1109/IRMMW-THz46771.2020.9370659.

[46] Melanie Müller et al. "Phase-Resolved Detection of Ultrabroadband THz Pulses inside a Scanning Tunneling Microscope Junction". In: *ACS Photonics* 7.8 (Aug. 19, 2020). Publisher: American Chemical Society, pp. 2046–2055. DOI: 10.1021/acsphotonics.0c00386.

[47] Yang Luo et al. "Nanoscale terahertz STM imaging of a metal surface". In: *Physical Review B* 102.20 (Nov. 16, 2020). Publisher: American Physical Society, p. 205417. DOI: 10.1103/PhysRevB.102.205417.

[48] Bowen Li et al. "Fabricating ultra-sharp tungsten STM tips with high yield: double-electrolyte etching method and machine learning". In: *SN Applied Sciences* 2.7 (June 18, 2020), p. 1246. ISSN: 2523-3971. DOI: 10.1007/s42452-020-3017-4.

[49] James K. Schoelz et al. "High-percentage success method for preparing and pre-evaluating tungsten tips for atomic-resolution scanning tunneling microscopy". In: *Journal of Vacuum Science & Technology B* 30.3 (Apr. 6, 2012), p. 033201. ISSN: 2166-2746. DOI: 10.1116/1.3701977.

[50] Timo Paschen et al. "Highly Localized Optical Field Enhancement at Neon Ion Sputtered Tungsten Nanotips". In: *Nano Letters* 23.15 (Aug. 9, 2023). Publisher: American Chemical Society, pp. 7114–7119. ISSN: 1530-6984. DOI: 10.1021/acs.nanolett.3c01985.

[51] Christoph Huber et al. "Optical near-field excitation at commercial scanning probe microscopy tips: a theoretical and experimental investigation". In: *Phys. Chem. Chem. Phys.* 16.6 (2014), pp. 2289–2296. ISSN: 1463-9076, 1463-9084. DOI: 10.1039/C3CP51730F.

[52] Sebastian Thomas et al. "Large optical field enhancement for nanotips with large opening angles". In: *New Journal of Physics* 17.6 (June 2015). Publisher: IOP Publishing, p. 063010. ISSN: 1367-2630. DOI: 10.1088/1367-2630/17/6/063010.

[53] L. Wimmer et al. "Terahertz control of nanotip photoemission". In: *Nature Physics* 10.6 (June 2014). Publisher: Nature Publishing Group, pp. 432–436. ISSN: 1745-2481. DOI: 10.1038/nphys2974.

[54] Peter Nguyen. "Terahertz Near-Field Coupling in Scanning Tunneling Microscopy". PhD thesis. University of Alberta, 2024.

[55] Ankan Biswas, S. R. Meher, and Deepak K. Kaushik. "Electronic and Band Structure calculation of Wurtzite CdS Using GGA and GGA+U functionals". In: *Journal of Physics: Conference Series* 2267.1 (May 2022). Publisher: IOP Publishing, p. 012155. ISSN: 1742-6596. DOI: 10.1088/1742-6596/2267/1/012155.

[56] N. G. Stoffel. "Experimental band structure of cadmium sulfide". In: *Physical Review B* 28.6 (Sept. 15, 1983). Publisher: American Physical Society, pp. 3306–3319. DOI: 10.1103/PhysRevB.28.3306.

[57] Y. R. Wang and C. B. Duke. "Cleavage faces of wurtzite CdS and CdSe: Surface relaxation and electronic structure". In: *Physical Review B* 37.11 (Apr. 15, 1988), pp. 6417–6424. ISSN: 0163-1829. DOI: 10.1103/PhysRevB.37.6417.

[58] D. D. D. Ma, C. S. Lee, and S. T. Lee. "Scanning tunneling microscopic study of boron-doped silicon nanowires". In: *Applied Physics Letters* 79.15 (Oct. 8, 2001), pp. 2468–2470. ISSN: 0003-6951, 1077-3118. DOI: 10.1063/1.1409276.

[59] S. Yngman et al. "GaN nanowires as probes for high resolution atomic force and scanning tunneling microscopy". In: *Review of Scientific Instruments* 90.10 (Oct. 1, 2019), p. 103703. ISSN: 0034-6748, 1089-7623. DOI: 10.1063/1.5122791.

[60] Lassana Ouattara et al. "GaAs/AlGaAs Nanowire Heterostructures Studied by Scanning Tunneling Microscopy". In: *Nano Letters* 7.9 (Sept. 1, 2007), pp. 2859–2864. ISSN: 1530-6984, 1530-6992. DOI: 10.1021/nl071550z.

[61] Rainer Timm et al. "Current–Voltage Characterization of Individual As-Grown Nanowires Using a Scanning Tunneling Microscope". In: *Nano Letters* 13.11 (Nov. 13, 2013), pp. 5182–5189. ISSN: 1530-6984, 1530-6992. DOI: 10.1021/nl402570u.

[62] Abhijit Bera, Sukumar Dey, and Amlan J. Pal. "Band Mapping Across a pn-Junction in a Nanorod by Scanning Tunneling Microscopy". In: *Nano Letters* 14.4 (Apr. 9, 2014), pp. 2000–2005. ISSN: 1530-6984, 1530-6992. DOI: 10.1021/nl500081m.

[63] Shancheng Yan et al. "Synthesis of uniform CdS nanowires in high yield and its single nanowire electrical property". In: *Journal of Solid State Chemistry* 182.10 (Oct. 1, 2009), pp. 2941–2945. ISSN: 0022-4596. DOI: 10.1016/j.jssc.2009.07.016.

[64] Qingyang Bao et al. "Circular-area-equivalence approach for determining propagation constants of a single-mode polygonal nanowire". In: *JOSA B* 39.3 (Mar. 1, 2022). Publisher: Optica Publishing Group, pp. 795–800. ISSN: 1520-8540. DOI: 10.1364/JOSAB.445738.

[65] Fuxing Gu et al. "Sub-bandgap transverse frequency conversion in semiconductor nanowaveguides". In: *Nanoscale* 6.21 (Oct. 10, 2014). Publisher: The Royal Society of Chemistry, pp. 12371–12375. ISSN: 2040-3372. DOI: 10.1039/C4NR04020A.

[66] S. Tongay, T. Schumann, and A. F. Hebard. "Graphite based Schottky diodes formed on Si, GaAs, and 4H-SiC substrates". In: *Applied Physics Letters* 95.22 (Dec. 1, 2009), p. 222103. ISSN: 0003-6951. DOI: 10.1063/1.3268788.

[67] S. Tongay et al. "Tuning Schottky diodes at the many-layer-graphene/semiconductor interface by doping". In: *Carbon* 49.6 (May 1, 2011), pp. 2033–2038. ISSN: 0008-6223. DOI: 10.1016/j.carbon.2011.01.029.

[68] N. Batina, A. S. Dakkouri, and D. M. Kolb. "The surface structure of flame-annealed Au(100) in aqueous solution: An STM study". In: *Journal of Electroanalytical Chemistry* 370.1 (June 6, 1994), pp. 87–94. ISSN: 1572-6657. DOI: 10.1016/0022-0728(93)03212-8.

[69] R. M. Feenstra et al. "Influence of tip-induced band bending on tunnelling spectra of semiconductor surfaces". In: *Nanotechnology* 18.4 (Dec. 2006), p. 044015. ISSN: 0957-4484. DOI: 10.1088/0957-4484/18/4/044015.

[70] J. Łagowski, C. L. Balestra, and H. C. Gatos. "Electronic characteristics of "real" CdS surfaces". In: *Surface Science* 29.1 (Jan. 1, 1972), pp. 213–229. ISSN: 0039-6028. DOI: 10.1016/0039-6028(72)90080-5.

[71] A. Ganguly and S. S. Nath. "Mn-doped CdS quantum dots as sensitizers in solar cells". In: *Materials Science and Engineering: B* 255 (May 1, 2020), p. 114532. ISSN: 0921-5107. DOI: 10.1016/j.mseb.2020.114532.

[72] Pralay K. Santra and Prashant V. Kamat. "Mn-Doped Quantum Dot Sensitized Solar Cells: A Strategy to Boost Efficiency over 5%". In: *Journal of the American Chemical Society* 134.5 (Feb. 8, 2012). Publisher: American Chemical Society, pp. 2508–2511. ISSN: 0002-7863. DOI: 10.1021/ja211224s.

[73] Gaurab Rimal et al. "Giant photocurrent enhancement by transition metal doping in quantum dot sensitized solar cells". In: *Applied Physics Letters* 109.10 (Sept. 6, 2016), p. 103901. ISSN: 0003-6951. DOI: 10.1063/1.4962331.

[74] David J. Keller and Chou Chih-Chung. "Imaging steep, high structures by scanning force microscopy with electron beam deposited tips". In: *Surface Science* 268.1 (Jan. 1, 1992), pp. 333–339. ISSN: 0039-6028. DOI: 10.1016/0039-6028(92)90973-A.

[75] G. Reiss et al. "Scanning tunneling microscopy on rough surfaces: Tip-shape-limited resolution". In: *Journal of Applied Physics* 67.3 (Feb. 1, 1990), pp. 1156–1159. ISSN: 0021-8979. DOI: 10.1063/1.345712.

[76] Michael Becker and Richard Berndt. "Influence of band structure on the apparent barrier height in scanning tunneling microscopy". In: *Physical Review B* 81.3 (Jan. 27, 2010). Publisher: American Physical Society, p. 035426. DOI: 10.1103/PhysRevB.81.035426.